TECHNISCHE
UNIVERSITÄT
WIEN
Vienna University of Technology

DIPLOMARBEIT

Tailoring trap current distributions in superconducting atomchips

Ausgeführt am

Atominstitut

der Technischen Universität Wien

unter der Anleitung von

Univ.Prof. Dipl.-Ing. Dr.techn. Jörg SCHMIEDMAYER
Projektass. Dr.rer.nat. Fritz Randulf DIORICO, MSc
Projektass. Dipl.-Ing. Stefan MINNIBERGER

durch

Benedikt Gerstenecker

Matrikelnummer 0907969
Kellergasse 6, 2103 Langenzersdorf

Langenzersdorf, March 27, 2017

Abstract

The experiment aims at the generation of hybrid quantum systems, combining ultracold atomic physics and superconductivity. Recent results suggested the possibility of tailoring current distributions in a superconducting atomchip wire and thereby creating arbitrarily shaped trapping structures. A quenching setup has been implemented, which allows for erasing the remnant magnetization of the superconducting wire. Employing a high power laser, it is utilized for resetting the superconductor to its virgin state within milliseconds. By means of an array of magnetic coils, cold ^{87}Rb atoms are transported from a room temperature MOT chamber to a $4\,$K cryogenic environment. These atoms are highly sensitive to magnetic fields, which makes them a useful tool for field sensing. In order to maximize the atom count, the entire MOT setup has been optimized. This resulted in up to 3×10^9 atoms with a temperature of 500-600 μK. Around 3×10^8 atoms reach the cold science chamber, where they are prepared for loading into a chip trap, utilizing evaporative cooling with an rf source. This cooling phase has recently been extended and should result in a very dense atom cloud soon. Although it still has room for improvement, atom cloud temperatures of the order of $10\,\mu$K in a QUIC trap have been observed. In the near future, measurements are expected to give new insights into the hysteresis behavior of type-II superconductors. This will open up new perspectives on both probing and utilizing specific properties of superconducting surfaces, employing ultracold atoms as field sensors.

Zusammenfassung

Zweck des Experiments ist die Erzeugung von Hybrid-Quantensystemen durch die Kombination ultrakalter Atome mit Supraleitern. Kürzlich gewonnene Messergebnisse deuteten darauf hin, dass die Stromverteilung in einem supraleitenden Atomchip-Draht programmierbar ist, was das Generieren beliebig geformter Atomfallenstrukturen ermöglichen würde. Ein Quench-Setup wurde aufgebaut, mit dem die remanente Magnetisierung in einem supraleitenden Draht gelöscht werden kann. Dabei wird ein Hochleistungslaser verwendet, um den Supraleiter innerhalb von Millisekunden in seinen ursprünglichen Zustand zurückzusetzen. Mit Hilfe einer Anordnung aus Magnetspulen werden kalte ^{87}Rb Atome aus einer MOT Kammer bei Raumtemperatur in ein kryogenes Milieu bei $4\,$K transportiert. Da diese Atome hochsensitiv für Magnetfelder sind, können sie als Messinstrument für solche eingesetzt werden. Das MOT-Setup wurde hinsichtlich der Atomzahl optimiert, was letztlich bis zu 3×10^9 Atome mit Temperaturen um 500-600 μK lieferte. Etwa 3×10^8 Atome erreichen die Experimentierkammer, wo sie mittels evaporativen Kühlens mit einem Radiofrequenzsignal auf das Laden in eine Chipfalle vorbereitet werden. Diese Kühlphase wurde kürzlich erweitert und sollte bald in einer äußerst dichten Atomwolke resultieren. Obwohl noch einiges an Verbesserungspotential vorhanden ist, wurden in einer QUIC-Falle bereits Temperaturen in der Größenordnung von $10\,\mu$K beobachtet. In naher Zukunft dürften Messungen neue Einsichten in das Hystereseverhalten von Typ-2-Supraleitern geben. Das wird neue Perspektiven bezüglich der Analyse und der Anwendung besonderer Eigenschaften von supraleitenden Oberflächen eröffnen, wobei ultrakalte Atome für das Messen der Magnetfelder benutzt werden können.

Contents

1 Introduction

1.1 Motivation

For quite some time now, atomchips have been employed in the field of quantum information. Their design allows for creating a wide variety of magnetic potentials and manipulating individual atoms [58]. Furthermore, coherence times of the order of seconds could be observed with atoms trapped in microchip traps [66]. Due to recent discoveries and developments, the next logical material for building such chips are superconductors. These can provide considerably longer lifetimes, further easing the coherence time restrictions in any quantum logic applications. This approach requires an ultracold atom cloud to be transferred into a cryogenic environment, which, ultimately, can be coupled to a superconducting microwave resonator, acting as a quantum bus for qubits [17]. This would mean the creation of a hybrid quantum device, which could be used to interconnect atomic and superconducting solid-state qubits, as outlined in [67]. Calculations and experimental tests (at an associated atomchip experiment) on the feasibility of such a concept were performed and evaluated in [37]. Design, simulation and fabrication of first resonators are in progress and will be reported in [46].

However, a necessary and important step towards this long-term goal would be understanding the impact of current and magnetic field sequences on the magnetization memory of a superconducting atomchip. The hysteresis behavior in type-II superconductors could already be successfully exploited for effectively tailoring trap geometries on a similar experiment [50]. Based on recent evidence presented in ch. 7 in [17], this is a promising prospect for the experiment: Accurately characterizing the current and magnetic field history dependence of a Z-wire type atomchip trap is expected to eventually allow for full programming of arbitrary trapping structures (e.g. a superconducting ring, as featured in [69]).

Furthermore, the emergence of vortices in type-II superconductors can be studied by means of the ultracold atoms and consequently employed for trap design. The net magnetic field of such vortices could already be utilized for creating self-sufficient traps for neutral atoms [72], which do neither require a transport current, nor an external bias field. Trapping atoms with single vortices and thereby creating small-spaced lattices has been proposed as well [56].

1.2 QuIC history

The **Qu**antum **I**nter**C**onnect experiment was started around ten years ago and has endured two generations of PhD, several diploma/MSc, and plenty of short-term project students. A laser setup including the appropriate locking electronics [4] and a vacuum chamber equipped with the coils required for trapping and cooling ^{87}Rb atoms in a MOT (**m**agneto-**o**ptical **t**rap) [42] were designed and built in the early stages of the experiment. Different ways of realizing a transfer system for ultracold atoms were considered, upon which – after elaborate calculations and simulations [42] – a magnetic transport line was chosen and constructed. Furthermore, a concept for supplying coils plus an atomchip inside a cryogenic environment and providing sufficient thermal radiation shielding was created and put into practice [28]. The calculation of the current sequences was integrated

into the experimental control program, and the transfer into a QUIC (**qu**adrupole-**I**offe-**c**onfiguration) trap, allowing for evaporatively cooling the cold atom cloud inside a science chamber at $\sim 4\,\mathrm{K}$, was implemented and characterized [52].

A crucial factor for any of the intended applications is the chip design, for which the sophisticated properties of the superconducting material have to be taken into account. For this reason, calculations and experimental tests on the performance of such wires and the resulting traps were conducted [32]. A paper was published in 2014 [47], summarizing the progress on trapping atoms on a superconducting atomchip and in this context presenting the magnetic transport system. The most recent progress covers the evidence of a magnetization memory in type-II superconductors [17].

1.3   Goals and progress

The objective was getting the experiment ready for characterizing the hysteresis behavior of the chip wire (ch. 2.5.3). Although due to certain drawbacks it was not possible to conduct the intended measurements, a lot of improvements on the optics and some extensions to the experimental control interface paved the way for achieving a sufficiently big and dense atom cloud in the science chamber. Moreover, the implementation of a quenching setup for resetting the superconducting atomchip to its virgin state is expected to allow for an accurate analysis of the wire's magnetization memory.

The described improvements particularly comprise the laser locking scheme, which was analyzed in great detail (ch. 3.3.1), and the MOT alignment. The latter required a lot of effort, until a proper technique could be found (ch. 5.2). Ultimately, the goal of obtaining a massive atom cloud was definitely achieved (ch. 4.2.3). Plenty of optimization scans and the modification of the atom cooling phase in the science chamber resulted in a reasonable cloud, ready for loading into a chip trap (ch. 4.4.3). Finding a method to instantly quench the chip wire could successfully be accomplished by means of a separate laser setup with its own imaging system (ch. 3.5). Besides these major changes, the first 3D printed part in QuIC's history was designed and built in, serving as an additional thermal radiation shield in the $4\,\mathrm{K}$ stage (ch. 3.4.1). Further progress will be reported in [46], [68] and [61].

2 Theoretical background

2.1 Magnetic traps and transport of atoms with coils

Magnetic trapping   Each atomic state associated with an angular momentum $F \neq 0$ carries a magnetic dipole moment

$$\vec{\mu} = -g\mu_B \vec{F} , \qquad \text{where} \qquad \mu_B = \frac{e\hbar}{2m_e} \tag{2.1}$$

is the Bohr magneton and g the species-dependent g-factor. This dipole moment interacts with any magnetic field $\vec{B}$, adding a component to the overall energy according to

$$E = -\vec{\mu}\vec{B} = g\mu_B \vec{F}\vec{B} . \tag{2.2}$$

For sufficiently weak magnetic fields, where the resulting energy gaps are distinctly smaller than the hyperfine splitting, this leads to the normal Zeeman effect, shifting the previously degenerate levels linearly apart:

$$E = g\mu_B m_F B_a \qquad \text{with} \qquad m_F = -F, -F+1, ..., F-1, F . \tag{2.3}$$

The different m_F values represent the eigenstates of the spin component F_a parallel to the field along an axis a. If this magnetic field features a positive gradient $\partial B_a/\partial a$, depending on the sign of the product gm_F an atom experiences a force pushing it either towards the field minimum or in the direction of a maximum. Since energy minima are favored, for $gm_F > 0$ a so-called low-field-seeking state is established, which is the first choice for magnetic traps (it is not possible to create a magnetic field maximum by means of a static field, known as Earnshaw's theorem).

Optical pumping   In order to trap as many atoms as possible, in consequence of (2.3) they need to be prepared in the ground state with the highest m_F absolute value, the sign depending on g. For $g > 0$ this can be realized by shining in a circularly polarized laser beam driving σ_+ transitions (i.e., transitions with $\Delta m_F = +1$) while applying a homogeneous quantization field along the beam direction. This is called optical pumping, and its basic idea is adapting the laser frequency to a resonance with $F = F'$ (ground respectively excited state), where each of the two states is split into $2F + 1$ sublevels in a weak magnetic field. Being exposed to the resonant light, the atoms keep switching between the two states, with every interaction increasing m_F by one, until ideally they end up in the $|F, m_F = F\rangle$ ground state. The latter is then called dark because the σ_+ light cannot induce any further transitions, since there is no $m_{F'} > F$. The $g < 0$ case works analogously with σ_- light [17].

Trap properties   In principle, there are different ways of constructing a magnetic trap. The simplest configuration for creating a field minimum is a quadrupole field with a strong gradient, as generated by a coil pair in anti-Helmholtz configuration, where two coaxial coils are supplied with opposite currents. The trapped cloud is subject to different loss mechanisms, starting with the evident occurrence of collisions between two or more particles. This also involves the background gas, which is why a properly evacuated

chamber is inevitable. Consequently, the (energy-dependent) temperature assigned to the atoms increases, upon which some of them exceed the trap depth and fly away. This and other influences reducing the trap stability are specified in greater detail in [28]. In order to compensate for those, it is necessary to cool the atoms, which can be performed by means of a laser setup and will be explained in ch. 2.2.

Majorana losses When working with magnetic traps, a substantial constraint is given by spin-flips: Once the condition $gm_F > 0$ is not fulfilled any more, according to (2.3) atoms leave the trap, for $gm_F < 0$ becoming high-field-seeking. Even when thermal fluctuations are sufficiently suppressed, an atom is prone to spontaneously changing its spin orientation if the magnetic moment cannot adiabatically follow the field direction defining the quantization axis. The basic condition for the adiabatic approximation [45] can be written as

$$\omega_L \gg \frac{1}{B_a} \left| \frac{dB_a}{dt} \right| \qquad \text{with} \qquad \omega_L = \frac{g\mu_B}{\hbar} B_a \; . \tag{2.4}$$

The Larmor frequency ω_L characterizes the precession of the spins around the quantization axis a and is directly connected to the energy gap between the different Zeeman levels (2.3),

$$\Delta E = g\mu_B B_a = \hbar \omega_L \; . \tag{2.5}$$

Hence, in a static trap such spin-flips occur especially in the area with almost vanishing field strength, where the Zeeman splitting is very weak. For this reason, an atom passing by a zero trap bottom is likely to be scattered into an untrapped state [40].

The aim of ultracold atomic physics usually is achieving a cold, dense cloud confined to a small area around the trap bottom. In order to avoid such Majorana losses, therefore a non-zero field minimum is required. This can be attained by a Ioffe-Pritchard configuration, where a superimposed magnetic field lifts the trap bottom and preserves a useful quantization axis everywhere. Consequently, condition (2.4) is met and transitions between the Zeeman sublevels are suppressed, which is why the atoms tend to stay close to the field minimum [26, 55].

Magnetic transport In a static magnetic trap, an atom cloud is confined to a certain area around the field minimum depending on its temperature. If this minimum is shifted to another position, the low-field-seeking atoms try to follow the field change and move to the new trap bottom. An array of coils, allowing for creating a movable magnetic field minimum, can thus be employed for transferring a cold atom cloud along a certain axis defined by the setup geometry. Here it is important to consider the adiabatic approximation (2.4) as well, so the variation of the magnetic field must not happen too fast.

In order to prepare the atoms for magnetic transport, they need to be trapped and cooled in a sufficiently big vacuum chamber with all necessary accesses and a rather large coil pair (see ch. 2.2). This constructional constraints favor horizontally extracting the cold cloud from such a chamber, which requires a so-called push-coil. The latter is mounted perpendicular to the mentioned coil pair and must withstand high currents, in order to provide a strong magnetic field. It can be employed to literally push the trap

minimum towards the first coil pair of a horizontal transport line. A vital parameter for moving atoms horizontally by means of coils is the cloud aspect ratio. When only two pairs of coils are used to shift the field minimum, the cloud shape depends on the minimum location (fig. 2.1a). This can be overcome by introducing an additional degree of freedom, namely a third coil pair (fig. 2.1b). It allows for individually controlling the trap bottom position, the field gradient and the aspect ratio, and, ultimately, for horizontal transport of an atom cloud. Adding a vertical transport section uses a different approach. Again starting with a cloud trapped between a pair of coils, moving the atoms upwards requires an array of stacked coaxial coils. The atom cloud can then be shifted along the common median axis, until ending up trapped between the uppermost coil pair. As suggested by calculations, it is advantageous to supply four coils at the same time, in order to maintain steady current curves (fig. 2.1c). It should be noted, that this setup premises the possibility to rapidly switch the current direction, once the cloud has passed the center of a coil. Combining the two concepts, it makes sense to stack up the vertical transport section above the very last coil pair of the horizontal part [28, 42].

(a) [1]

(b) [2]

(c) [3]
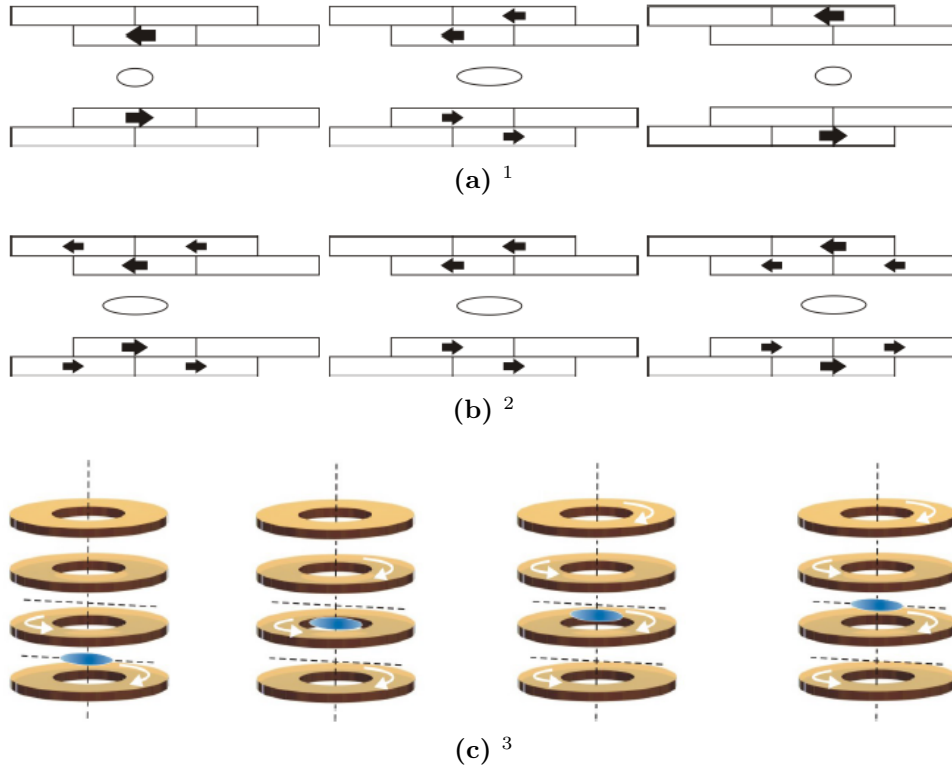
Fig. 2.1: Schematic figure of the magnetic transport. Simultaneously supplying only two coil pairs for horizontal transport results in an oscillating aspect ratio **(a)**. Shifting the minimum by means of three pairs allows for preserving the cloud shape **(b)**. The opposite arrow directions in each coil pair emphasize the anti-Helmholtz configuration, creating a quadrupole trap with a central field minimum $|\vec{B}| = 0$. In the vertical part, four coils are simultaneously supplied, whenever possible **(c)**.

---

[1]Lippok 2008 [42], ch. 3.3, fig. 3.1
[2]Lippok 2008 [42], ch. 3.3, fig. 3.2
[3]Haslinger 2011 [28], ch. 10.3, fig. 10.3

2.2 Laser cooling

2.2.1 Radiation pressure and Doppler effect

Confining a large number of atoms in a magnetic trap requires acquiring a sufficiently cold atom cloud from a background vapor. This can be achieved by standard methods of laser cooling. Its concept originates from the fact, that the absorption of a photon gives an atom a kick into the photon's direction of motion due to momentum conservation. The occurrence of such an event depends on the frequency, since only photons with energy $\hbar\omega$ matching an atomic transition of frequency ω_0 within the natural linewidth Γ are absorbed, lifting the atom into an excited state. However, since an atom is moving around in space with a velocity $\vec{v}$, the frequency of incident light with wave vector $\vec{k}$ is Doppler-shifted by a difference frequency $\omega_D = -\vec{k}\vec{v}$. For this reason, instead of the laser frequency ω_L it effectively sees

$$\omega_e = \omega_L - \left|\vec{k}\right| \left|\vec{v}\right| \cos\theta = \omega_L \left(1 - \frac{v}{c}\cos\theta\right) \ . \tag{2.6}$$

The parenthesized expression exceeds 1 if the atom moves towards the source, where for the angle between the two vectors $\pi/2 < \theta \leq \pi$ applies. Hence, in this case it experiences a higher frequency, and vice versa for the opposite orientation. If a laser beam red-detuned by a negative detuning δ from a resonance ω_0 is shined onto an atom cloud, atoms moving opposed to the beam can become resonant with the light ($\omega_e = \omega_L - \delta \equiv \omega_0$). Consequently, upon absorbing a photon they are pushed back and their velocity is effectively reduced. In contrast, for motion away from the light source, the effective frequency is shifted even further out of resonance. Therefore a second, counter-propagating beam can be added, addressing only atoms moving the other way. For sufficiently small velocity, this 1D configuration results in a damping force linearly dependent on v:

$$F = -\alpha v \ , \tag{2.7}$$

where the friction coefficient fulfills $\alpha > 0$ for detuning $\delta < 0$ (fig. 2.2) and is proportional to the optical power. However, when returning to a ground state, an excited atom emits a photon in a random direction. Due to momentum conservation, this results in another
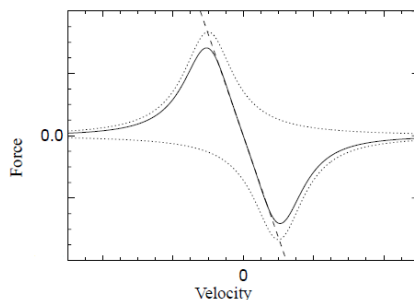

Fig. 2.2: Damping force for Doppler cooling with arbitrary units[4]. The exact shape depends on various parameters, but the concept of an effective force resulting from the overlay of two opposite beams is evident.

---

[4]Slightly modified version of Metcalf et al. 2006 [45], ch. IV, fig. 4

change of this atom's velocity. Moreover, the emitted photon can be absorbed by another atom, which is therefore randomly deflected too. In consequence, similar to momentum diffusion in a liquid (where the viscosity is characterized by an analog damping term), the absorption and spontaneous emission processes lead to a heating rate competing with the cooling mechanism. This sets a lower limit to the cloud temperature, which represents the maximum of the corresponding Maxwell-Boltzmann distribution. It was found to be minimized for

$$\delta \approx -\Gamma/2 \qquad \Rightarrow \qquad k_B T_D = \frac{\hbar\Gamma}{2} \ , \tag{2.8}$$

yielding the Doppler temperature T_D. The concept of Doppler cooling can be extended to three dimensions with three pairs of counter-propagating, red-detuned laser beams. Due to the viscous quality of the force (2.7), this setup is referred to as an optical molasses. Anyway, although in this manner atoms can be successfully cooled, it cannot act as a trap: Since there is no position-dependent force driving the atoms back to the center, they can leave the intersection region, upon which they are lost from the cooling process. For a detailed review on Doppler cooling refer to [3, 45].

2.2.2 Magneto-optical trap

In order to create a position-dependent restoring force, a magnetic quadrupole field is added, just as used for magnetic trapping (cf. ch. 2.1), but distinctly weaker. The Doppler cooling mechanism is independent of the beam polarization, so the latter can in principle be arbitrarily chosen. To understand the concept of such a MOT, the 1D case is considered again, assuming two opposed beams slightly red-detuned to an atomic transition $|F = 0, m_F = 0\rangle \to |F' = 1, m_{F'} = -1, 0, +1\rangle$. The anti-Helmholtz configuration of two coils generates a linearly inhomogeneous field along the beam propagation axis $\hat{z}$,

$$B(z) = bz \ . \tag{2.9}$$

According to (2.3), this leads to a position-dependent Zeeman splitting of the $m_{F'}$ levels: The further away from $z = 0$ an atom is located, the bigger the energy difference between its sublevels. Which state is shifted downwards is determined by the sign, since for $z > 0$ the $m_{F'} = -1$ level has a lower energy, while $z < 0$ favors $m_{F'} = +1$. Consequently, an atom at a certain position $z = z' > 0$ scatters more light from a σ_- beam driving the transition $|0,0\rangle \to |1,-1\rangle$, than from incident σ_+ light. If a beam propagating in $-\hat{z}$-direction is σ_-, and an opposed one σ_+ polarized, on either side of the trap center the atoms are more likely to absorb photons moving towards $z = 0$ (fig. 2.3a). This constitutes a force similar to Doppler cooling, but depending on the position instead of the velocity. Effectively, the particles are therefore pushed towards the center of the magnetic trap. This way, the laser cooling mechanism can be combined with a confinement around a trap minimum.

An extension to three dimensions can be implemented with a magnetic quadrupole field (fig. 2.3b). It results in a force providing compression (characterized by a spring constant κ) and cooling of atoms simultaneously,

$$\vec{F} = -\alpha\vec{v} - \kappa\vec{r} \ . \tag{2.10}$$

Furthermore, the described scheme is not limited to the $F = 0$ case, but works for any $F \to F' = F + 1$ transition. Therefore, a MOT is a very easy solution for cooling and
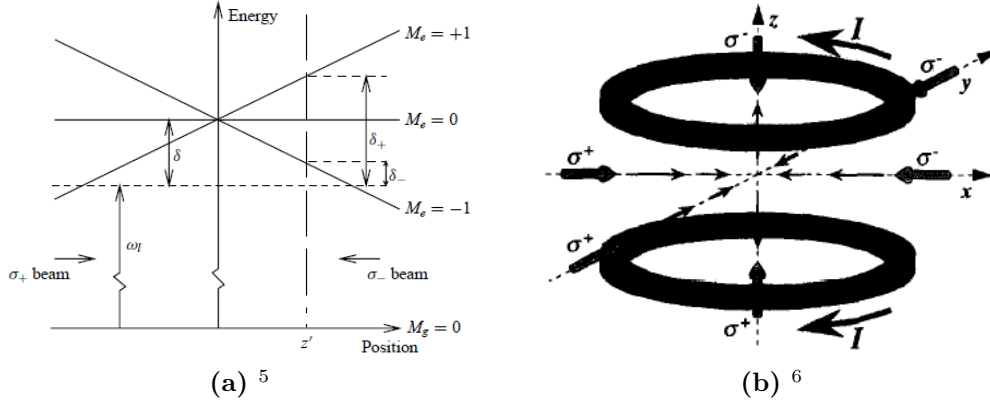
Fig. 2.3: Concept of a magneto-optical trap. In an inhomogeneous magnetic field the Zeeman level shift varies with position, which is why the resonance frequency for incident light depends on the latter's polarization (**a**). In 3D the required conditions are provided by a quadrupole field and three pairs of counter-propagating laser beams with opposite circular polarizations with respect to the quantization axis (**b**).

trapping neutral atoms. However, due to the mentioned constraints of laser cooling, the achievable density is limited: There is a maximum amount of atoms that can be trapped within a certain volume, for which reason sufficiently wide laser beams and rather big coils are necessary [45].

2.2.3   Sub-Doppler cooling

Soon after the first experiments on atom cooling in an optical molasses, cloud temperatures considerably below the theoretically predicted limit T_D were measured for detunings $\delta \ll -\Gamma/2$. Contradicting any preceding calculations, those observations could finally be assigned to a polarization gradient emerging due to the beam superposition. In the 1D case two opposing, appropriately polarized beams can be utilized for cooling an atom cloud below the Doppler limit. While a $\pi\perp\pi$ configuration (perpendicular linear polarizations) can provide a stronger damping effect, the combination with a standard MOT suggests a σ_+-σ_- setup (cf. fig. 2.3b). This way, the atoms can first be trapped and cooled to the Doppler limit according to (2.10), and subsequently further slowed down in a field-free optical molasses with more negative δ.

The effective polarization resulting from the beam overlay is linear at every location, but rotating about the propagation axis (fig. 2.4). A vital requirement for this cooling
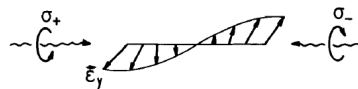

Fig. 2.4: σ_+-σ_- polarization gradient cooling[7]. The counter-propagating beams effectively generate a linear polarization rotating about the propagation axis.

---

[5]Metcalf et al. 2006 [45], ch. VII D, fig. 12
[6]Adams et al. 1997 [3], ch. 2.4.3, fig. 9(b)
[7]Section of Dalibard et al. 1989 [14], ch. 2, fig. 1(a)

mechanism is $F \geq 1$, since it relies on a population imbalance in the ground state. This imbalance is induced by a light shift, which occurs due to the linear polarization the atoms effectively experience (by analogy with the Zeeman effect, but for an electric field). In an atom at rest, the $|F = 1, m_F = 0\rangle$ state is then more populated than the other two with $m_F = \pm 1$, both shifted towards higher energies. Note the contrast to the simple first-order approximation yielding (2.3), which does not apply here. If the atom moves along the beam axis $\hat{z}$ with velocity v, it experiences a periodic rotation of the quantization axis. In a rotating inertial frame, where the linear polarization points into the same direction $\hat{y}$ everywhere, a new term proportional to the velocity emerges,

$$V_{rot} = kvF_z \ . \tag{2.11}$$

While in this description the m_F splitting occurs with respect to the $\hat{y}$-axis, this term adds an inertial field parallel to $\hat{z}$, introducing non-adiabatic couplings between the ground state sublevels. In consequence, the population (Π) distribution of F_z's eigenstates shows a velocity-dependent imbalance between the corresponding $\tilde{m}_F = \pm 1$ levels. Atoms moving in the $\mp\hat{z}$ direction (where $v \lessgtr 0$) feature a more populated $\tilde{m}_F = \pm 1$ state:

$$\Pi_{+1} - \Pi_{-1} \sim -kv \qquad \text{for} \qquad \delta < 0 \tag{2.12}$$

The actual cooling mechanism is very similar to Doppler cooling. The probability that an atom in a $\tilde{m}_F = \pm 1$ ground state absorbs a $\sigma_\pm$ photon is six times higher than for a $\sigma_\mp$ absorption event. For this reason, atoms moving along $+\hat{z}$, implying $\Pi_+ < \Pi_-$ (2.12), scatter more σ_- light, and such following $-\hat{z}$ tend to absorb σ_+ photons, respectively. This creates a strong friction force, since the atoms mostly absorb counter-propagating light, upon which their velocity is damped similar to (2.7). The major difference between the two processes, however, is the dependence on laser power. The friction coefficient α of Doppler cooling increases with power, while the capture range, i.e., the range of velocities, over which the force behaves linearly, is independent of the light intensity. In contrast, polarization gradient cooling is characterized by a power-independent friction coefficient, but in return the capture range depends on the laser power.

The 3D version of such a σ_+-σ_- configuration conveniently coincides with a standard MOT without the magnetic field (cf. fig. 2.3b) and is therefore very well suited for experimental application. The lowest achievable cloud temperature is given by the recoil limit

$$k_B T_R = \frac{\hbar^2 k^2}{2M} \tag{2.13}$$

with the atomic mass M [14]. In principle, there are sophisticated methods of going even below this boundary, but they are not too easy to implement. Some approaches can be found in [3].

2.3 Laser spectroscopy with rubidium 87

2.3.1 Doppler-free FM saturated absorption spectroscopy

Locking a laser to an atomic resonance requires properly resolving the hyperfine transitions. This is impeded by line broadening, in particular by the Doppler effect. When a beam propagates through a vapor cell and its frequency is scanned across a range

$\omega_L^- < \omega_0 < \omega_L^+$, the absorption spectrum will not only show interaction at $\omega_L = \omega_0$. According to (2.6), atoms moving opposed to the beam ($v < 0$) can absorb light with $\omega_L - \omega_0 \equiv \delta < 0$, and such moving in parallel ($v > 0$) scatter photons with $\delta > 0$. A common approach for making a spectrum Doppler-free is a double-pass setup, constituting a pump-probe spectroscopy configuration. Here, an incident beam with $\delta \lessgtr 0$ interacts with a certain group of atoms within the thermal velocity distribution, characterized by $v = v' \lessgtr 0$. For sufficient intensity, the whole fraction addressed is driven into the excited state. When the laser beam is retro-reflected after the cell and passes it again, this time it is absorbed by another fraction with $v = -v'$, since the beam direction has been inverted (fig. 2.5a). At a true transition frequency $\delta = 0$, both beams are only scattered by atoms with $v = 0$, where no Doppler shift occurs (fig. 2.5b). Therefore, after the first beam passage (pump) the majority of these atoms at rest is already in the excited state, upon which the reflected beam (probe) passes the cell without any absorption events happening. This results in a dip in the absorption spectrum at $\omega_L = \omega_0$, eventually providing a Doppler-free spectrum and revealing the hyperfine transitions [24].

For closely spaced hyperfine levels, additional notches in the spectrum can be observed. They are called crossover resonances and arise due to the Doppler effect: If the pump beam is red-detuned to a transition ω_2, but at the same time blue-detuned to a lower resonance frequency ω_1 within range, it can interact with two groups of atoms with $v = v_2' < 0$ and $v = v_1' > 0$. Moreover, the probe will be scattered by two different fractions of the velocity distribution too, characterized by $v = -v_2'$ and $v = -v_1'$ (fig. 2.5c). In this manner, a lot of light is absorbed, resulting in an additional notch in the absorption spectrum. A crossover resonance ω_C always forms in the center between two lines because the Doppler shift is symmetric, which reads $\omega_C = (\omega_1 + \omega_2)/2$. They often are even stronger than the true atomic transitions [54].

For increasing the sensitivity and achieving a high resolution with a good signal-to-noise ratio, combining this saturated absorption spectroscopy method with the FM (**f**requency **m**odulation) technique has been proven very well utilized [51]. Here, the laser frequency is phase-modulated, where the modulation signal can be applied directly to the
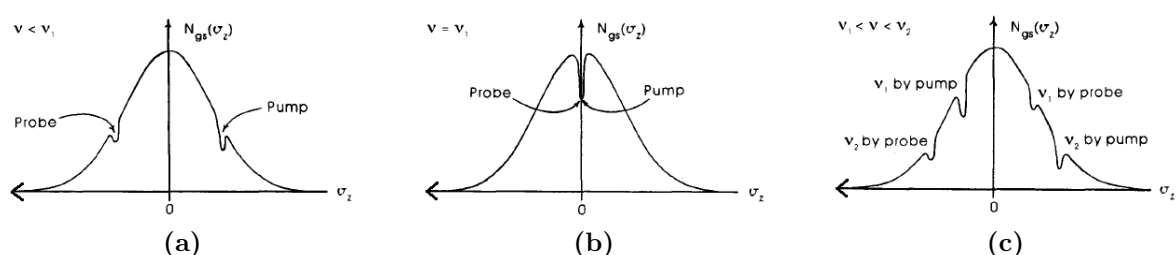
Fig. 2.5: Principle of pump-probe spectroscopy[8]. Here, ν_1 and ν_2 denote two resonance frequencies, and $v_z < 0$ describes atoms moving opposed to the pump beam. For $\delta < 0$, the light is scattered by two different velocity groups **(a)**, for $\delta = 0$ the shift vanishes and the pump beam already excites most of the atoms **(b)**. If the lines are sufficiently close to each other, absorption can take place for four different velocities **(c)**, resulting in an often even larger notch in the spectrum.

---

[8]Slightly modified and rearranged version of Preston et al. 1996 [54], ch. VI A, fig. 4

injection current. In consequence, apart from the so-called carrier frequency, symmetric sidebands appear. Those are equal in magnitude, but opposite in phase, and their offset from the center frequency is usually considerably larger than the natural linewidth Γ of an absorption line. In the limit of fast modulation, each point ω_L of a frequency scan therefore features two additional frequencies, at which atoms can absorb a fraction of the incident light. This effectively results in an amplitude modulation, stemming from the unbalanced sideband amplitudes and only vanishing at $\omega_L = \omega_0$ [33]. A detailed discussion of the theory behind the spectroscopy setup used at QuIC is given in [4].

2.3.2 Rubidium D2 line

An isotope widely used in ultracold atomic physics is ^{87}Rb, since its transitions allow for rather easily applying the methods described in chs. 2.1 and 2.2. In a standard rubidium vapor cell for spectroscopic applications, both ^{87}Rb and ^{85}Rb are present. Scanning the so-called D2 line at ~ 780.241 nm therefore comprises both isotopes, as can be inferred from fig. 2.6a. The relative natural abundance $\eta(^{87}\text{Rb}) = 27.83\%$ explains the fact, that in a typical spectroscopy signal the two smaller, outer Doppler peaks shown in fig. 2.6b represent the $F = 1 \rightarrow F' = 0, 1, 2, 3$ and $F = 2 \rightarrow F' = 0, 1, 2, 3$ transitions of ^{87}Rb, while the inner ones arise from the $F = 2 \rightarrow F' = 1, 2, 3, 4$ and $F = 3 \rightarrow F' = 1, 2, 3, 4$ resonances in ^{85}Rb.

Transition selection The concepts of the preceding chapters shall now be applied to the ^{87}Rb D2 line. At first, the atoms are trapped and cooled in the MOT phase. This requires an $F \rightarrow F' = F + 1$ transition, for which usually the $F = 2 \rightarrow F' = 3$ resonance is exploited. Doppler cooling is supposed to be most efficient at $\delta = -\Gamma/2$, where the natural linewidth of the ^{87}Rb $5^2\text{S}_{1/2} \rightarrow 5^2\text{P}_{3/2}$ transition is given with $\Gamma = 2\pi \times 6.0666$ MHz. The atom cloud temperature expected to be reached in this phase is $T_D = 145.54\,\mu\text{K}$. The subsequent molasses phase requires $F \geq 1$ and again $F \rightarrow F' = F + 1$, so the same resonance is well suited. Only the detuning has to become more negative, here $\delta \approx -2\Gamma$ is supposed to be a good starting value [3]. The recoil temperature is estimated with $T_R = 361.96$ nK, but premises ideal conditions, which are very unlikely to be achievable. Before being magnetically trapped and transported, the atoms need to be optically pumped into a dark ground state. This requires an $F = F'$ transition, which is why the $F = 2 \rightarrow F' = 2$ resonance can be employed for a pump beam. Hence, the ground state stays the same and only the excited one changes, so only a rather small frequency shift is needed. Since $g(5^2\text{P}_{3/2}) > 0$, the low-field-seeking states are characterized by $m_F > 0$ and σ_+ polarization is necessary.

Something that has not been considered yet is relaxation to the wrong ground state, $F = 1$. Upon falling to this energy level, an atom is lost from the cooling or pumping cycle. For this reason, an additional repump beam is added, pumping atoms from the $F = 1$ into the $F' = 2$ state. From there, they can relax to $F = 2$ and participate in the desired transitions again. For finally imaging an atom cloud, the $F = 2 \rightarrow F' = 3$ transition with $\delta = 0$ can be used. However, it shall be noted, that all the detuning values suggested here have to be adapted to potential energy level shifts. These deviations are most importantly induced by any magnetic fields present (remember the Zeeman effect (2.3)), such as (necessary) homogeneous bias fields. An overview of all the frequencies
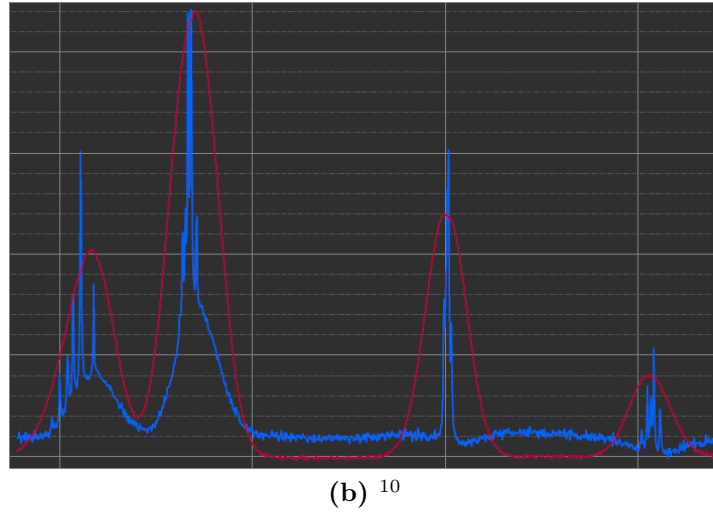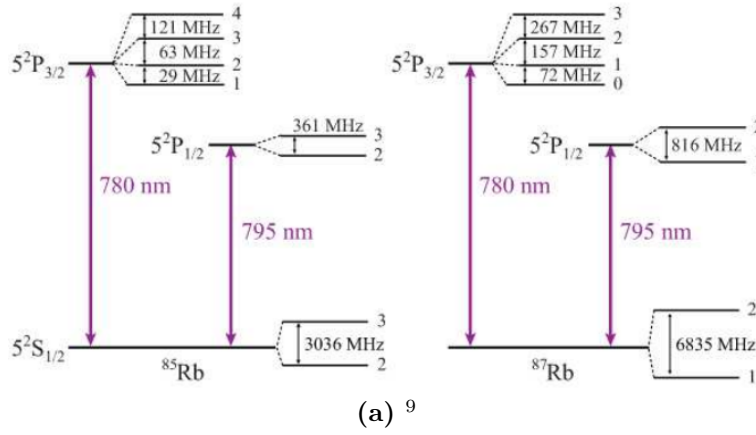
(a) [9]

(b) [10]

Fig. 2.6: Rubidium transitions. Both ^{87}Rb and ^{85}Rb feature a D1 and a D2 line **(a)**. Due to the large frequency gap between the respective ground states, in the D2 line four Doppler-broadened peaks (red) are obtained from a frequency scan. Within these envelopes, the Doppler-free spectrum (blue) can be resolved by means of saturated absorption spectroscopy **(b)**.

needed in the different experimental phases is given in fig. 2.7. All the rubidium properties denoted in this subsection were taken from [63].

2.4 Atomchip technology

With the establishment of atom cooling and trapping techniques, the interest in bringing cold atoms close to surfaces led to the development of so-called atomchips. These devices were invented as a more precise tool to manipulate cold atomic ensembles and allow for designing and controlling custom potentials. In their early history, it was shown that atoms can be trapped by combining the magnetic field generated by a current running through a straight wire with a perpendicular homogeneous bias field. The bias field breaks the rotation symmetry of the wire field, and renders the high-field-seeking atomic orbits unstable. Along a line parallel to the wire, the two magnetic fields cancel each other.

---

[9]Pooser et al. 2009 [53], ch. 4, fig. 5
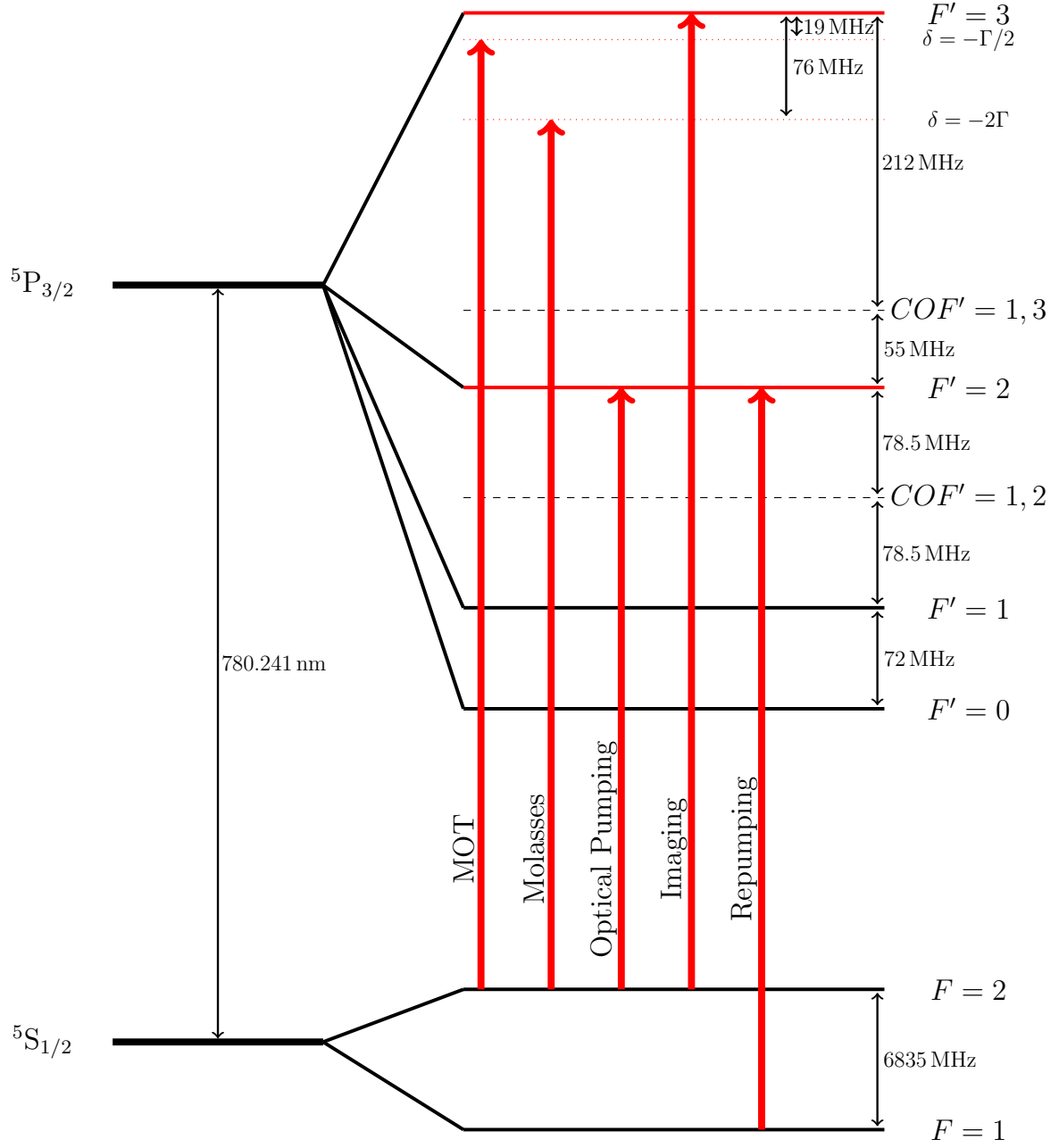[10]Gerstenecker and Schmid 2015 [25], ch. 1.2.2, fig. 1.4

Fig. 2.7: The ^{87}Rb D2 line including the different frequencies that must be provided in the experimental cycle. The denoted splitting frequencies are rounded values inferred from [63]. While the optimal detuning for the MOT phase is derived from theory, the molasses detuning only serves for orientation and needs to be empirically determined.

This effectively results in an elongated trap bottom, i.e., a tube with a field minimum in its center. In consequence, atoms in low-field-seeking states can be guided along the wire, which got the name "sideguide". This concept was soon considered very well suited for various applications in ultracold atomic physics. It can produce very steep traps for easily implementable parameters (such as field strength and current), and provides a huge design leeway. Already back then, J. Schmiedmayer, founder of the "Atomchip" group at the Vienna Institute of Atomic and Subatomic Physics[11], was involved in the developments [15].

Towards surface structures The crucial accomplishment was the creation of potentials with energy-level spacing large compared to particle temperature, thus suppressing excitations and allowing for coherent transport of atoms. This can be realized for neutral atoms moving microns above surfaces, which are equipped with nanofabricated charged and current-carrying structures. Simple modifications of the mentioned sideguide are U- or Z-shaped bent wires. The first form a 3D quadrupole trap, when being superimposed by a homogeneous field, the second result in a Ioffe-Pritchard type trap with the essential advantage of a non-zero field minimum. The latter prevents Majorana spin-flips driving atoms out of the trap, as outlined in ch. 2.1. In addition, such a Z-wire configuration makes generating high field gradients easy, yielding trap parameters used in BEC (**B**ose-**E**instein **c**ondensate) experiments. While first tests were conducted with free-standing arrangements, the planar design furthermore facilitates the fabrication of surface-mounted structures. For this reason, Z-wire traps are widely used in ultracold atomic physics. Mounted on atomchips, they provide even a lot more advantages inherent to surface traps, where the robustness and the rather easy production are only basic examples [6]. One of the major benefits of such surface structures is the possibility of creating arbitrary designs, as the combination of different wire shapes (and various other elements) allows for modeling various potentials. For example, in early successful measurements on loading a cold atom cloud from a MOT onto an atomchip, it could be additionally shown, that atoms can be trapped on a self-contained chip, where the magnetic bias field is created by the surface structure too [23].

Applications A rather huge field demanding specific atomic ensemble properties, that can be achieved by atomchip technology, is quantum information. Quantum logic requires sufficiently long coherence times, i.e., long-lived states, and the capacity of addressing individual fractions of an atom cloud, e.g. for performing controlled collisions. To a certain extent, this can be provided in atomchip micro-traps. The manipulation of qubit states and the implementation of logical operations are made possible by certain surface structures, such as beam splitters for matter waves realized with Y-shaped wires. Furthermore, the ability of compressing atoms to a BEC in a chip trap has the advantage of preparing an entire cloud in the ground state [58]. A lot of progress in atomchip technology over the last fifteen years has been done, which comprises the work with different atom species and materials. Besides quantum information, potential applications involve matter-wave interferometry (e.g. [59]), sensor technology, etc. An extensive overview of the present state of the art can be found in [34].

---

[11]Visit `http://atomchip.org/`

2.5 Superconductivity

2.5.1 Cryogenic environment

As indicated in ch. 1.1, the standard techniques described so far were decided to be combined with superconductors [67]. This requires placing the atomchip in an environment cooled below the corresponding transition temperature T_C of the chosen material (ch. 2.5.2). This upper temperature limit is always very far below room temperature, for most potential options considerably below the cooling range of the commonly used refrigerant Nitrogen (ch. 2.5.4). For this reason, it is necessary to operate a Helium cryostat designed for $4\,\mathrm{K}$ environments.

The use of superconductors and low temperatures brings certain advantages compared to standard atomchip setups. If a trapped ultracold atom cloud absorbs too much energy from its vicinity, many atoms are driven to untrapped states and fly away. Therefore, the atom number might be vastly reduced even before sufficient cooling can be achieved. On the one hand, this energy originates from near-field noise, which significantly affects the lifetime in normal metal chips. In superconductors, where the wire resistance becomes negligible, the noise stemming from thermal current fluctuations (Nyquist noise) is distinctly reduced compared to normal conductors [21, 57]. Another source are interactions with the background gas, which is why a high quality vacuum needs to be established. At room temperature experiments, this leads to long evacuation times. In such a cold environment, almost all potential impurities are simply frozen out. In conclusion, a superconducting atomchip in a cryogenic environment can provide much longer lifetimes.

Closed cycle cooling In ultracold atomic physics applications, an experiment is often supposed to run for many hours without interruption. Since in flow and bath cryostats the coolant has to be refilled very frequently, a system maintaining the heat exchange by an oscillating gas flow is favorable for such experiments. At QuIC, a GM (**G**ifford-**M**cMahon) cooler by ARS[12] perpetuates an oscillating gas flow by means of a moving physical piston. Unfortunately, this induces considerable vibrations in the millimeter range. Since the experimental setup must by all means be protected from such distortions, the $4\,\mathrm{K}$ cold finger had to be mechanically decoupled from the moving upper parts. This was done by interposing a rubber bellow filled with Helium and strongly damping the vibrations. A more detailed description including a heat budget estimation of this specific setup is given in [28]. A theoretical treatise of GM coolers in general can be found in [65].

2.5.2 Phase transition in superconductors

As claimed above, one of the characteristic properties of a superconductor is the vanishing resistance. It was first observed in mercury, where resistance measurements yielded $\rho = 0$ for $T \lesssim 4.15\,\mathrm{K}$. This can only be accepted within certain measurement limitations, but the vast difference between the normal conducting and the superconducting state, definitely covering very many orders of magnitude, justify this attribution. In fact, a sudden jump in the resistance occurs at a characteristic temperature T_C, referred to as

---

[12]Advanced Research Systems, `http://www.arscryo.com/`

the critical temperature of the superconducting phase. Furthermore, magnetic fields applied to a superconductor are expelled from the latter, which is explained by the Meissner effect. This phenomenon emerges regardless of whether the field is turned on before or after the phase transition, rendering an explanation by only the Maxwell equations void. In consequence, soon after this discovery the superconducting state was assumed to constitute an individual thermodynamic phase rather than simply an electronic lattice order effect. Based on the associated electrodynamics and thermodynamics, it was furthermore suspected to be a condensed state in momentum space, implying long-range order of the momentum vectors $\vec{k}_i$ in position space [43].

Cooper pairs and energy gap In fact, the concepts of BCS (**B**ardeen-**C**ooper-**S**chrieffer) theory [5], which has been proven a pretty accurate approximation for most properties of superconductors, rely on the assumptions outlined above. The keynote of this description is the interaction of two electrons via a lattice phonon, where the chances for this are highest for opposite momenta and spins. For an arbitrarily weak attractive potential $V < 0$, the overall energy is reduced, when two e^- couple in momentum space and form a quasi-bosonic particle, a Cooper pair $|\vec{k} \uparrow, -\vec{k} \downarrow\rangle$. This works despite the Coulomb repulsion, since they are still separated in position space. Consequently, electrons within a certain scope around the Fermi surface, limited by the maximum phonon frequency ω_D, pair up and constitute a new, coherent ground state. Thus, an energy gap Δ in the electronic excitation spectrum emerges. For the gap size at $T = 0\,\mathrm{K}$, the described formalism yields the universal relationship

$$2\Delta(0) = 3.54 k_B T_C \ , \tag{2.14}$$

indicating that BCS theory depends on only one parameter. Thermal fluctuations increase the chance for excitations and therefore diminish Δ, which is why its size depends on the temperature. A good approximation for this dependence is given by

$$\Delta(T) \simeq \Delta(0)\sqrt{1 - \left(\frac{T}{T_C}\right)^{3.3}} \ . \tag{2.15}$$

Finding analytic expressions would require distinguishing between different temperature regions below the critical point [70]. When converted to a frequency, the right side of (2.14) is significantly below the near-infrared range for all commonly used superconductors [1].

Critical parameters As can be inferred from (2.15), at $T = T_C$ the superconducting energy gap vanishes. When this critical temperature is exceeded, the material behaves like a normal conductor. Besides heating, there are other ways of breaking the superconducting phase, yielding further critical parameters. When an external magnetic field H_{ext} is increased above a certain limit H_C, maintaining a magnetization compensating for the applied field is not the energetically more favorable state for the superconductor any more. In so-called type-I superconductors this critical field marks the point, where the field expulsion entirely vanishes and the superconducting phase ceases (fig. 2.8a). Type-II superconductors feature two critical magnetic fields: Up to H_{C1} they are in the

Meissner phase, where an external field is expelled, above this limit the field starts to penetrate the material and a mixed state arises. This occurs in the form of quantized flux vortices, which constitute some kind of lattice due to mutual interaction. With increasing H_{ext}, more and more flux lines enter the sample and eventually start to overlap, upon which the superconducting phase completely breaks down at the second critical field H_{C2} (fig. 2.8b) [16, 70]. In sufficiently weak magnetic fields, some superconductors are in a semi-Meissner state with different domains, therefore labeled type-I/II (fig. 2.8c) [12].

Similarly, supplying a superconductor with a current is limited by a critical value I_C. Below this boundary, the movement of Cooper pairs with charge $-2e$ only adds a phase factor, which does not contribute to the probability density. Due to the coherence given by the BCS ground state, a supercurrent can thus be described as a mass of center movement, which only distinguishes itself from the current-free state by a phase factor. In consequence, no resistance arises and terminating the superconducting state requires dissolving the coherence of one Cooper pair with all the others. The latter is equivalent to breaking the pair by adding an energy $E \geq 2\Delta$, and leads to a critical current density proportional to the energy gap [11, 16]:

$$j_C \propto \Delta \ . \tag{2.16}$$

As the gap size is temperature dependent (2.15), the critical current is reduced if the sample is heated. This can lead to unwanted phase transitions, which might for example burn current-carrying coils (and possibly their vicinity) exposed to temperature fluctuations. On the one hand, the resistance jump above T_C can cause a lot of heat production. On the other, the entire field energy stored in the superconducting material might abruptly be dissipated as heat. Such a sudden breakdown of the superconducting phase is commonly referred to as a quench [19].

2.5.3 Current and magnetic field history

As proposed in ch. 1.1, in type-II superconductors the existence of a magnetization memory can be observed with ultracold atoms. The characteristics of this hysteresis behavior
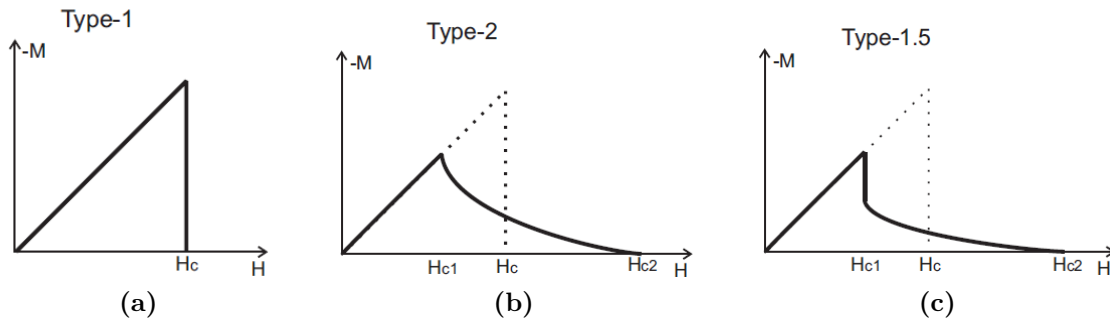
Fig. 2.8: Critical magnetic fields in different types of superconductors[13]. For type-I, a magnetization expelling an external field emerges, until the applied field dissipates too much energy and the superconducting phase breaks down **(a)**. In type-II superconductors, above a first critical field the sample is partially penetrated **(b)**, particularly in multi-component materials a mixture of the two types can constitute a semi-Meissner state **(c)**.

---

[13]Rearranged version of Carlstrom et al. 2011 [12], ch. I, fig. I

depend on the geometry of the superconducting sample. The case of an elongated specimen (slab or cylinder) exposed to a parallel external field $H_{C1} < H_{ext} < H_{C2}$ is examined by the Bean model. In the Meissner phase (below H_{C1}), shielding currents are running only over the sample surface; this model now supposes further penetration of the superconductor by these currents, when the first critical field is exceeded. It assumes a filamentary structure with separate regions, carrying either $j = 0$ or $j = j_C$. Consequently, the field is effectively attenuated inside the sample, as depicted in fig. 2.9. The resulting division into entirely normal conducting respectively superconducting domains serves as an explanation for the observed quantized flux lines.

The Bean model already comprises some certain hysteresis in a type-II superconductor, in particular the trapping of such flux lines: If an external field parallel to a superconducting slab is first increased to $H_{ext} = H_0 > H_{C1}$ and then ramped down again, the sample surface effectively experiences an opposite field and the surface currents reverse. Although H_{ext} is set to zero again, two regions with oppositely directed current sheets carrying $j = \pm j_C$ emerge. They are separated by a current-free layer, which corresponds to a trapped flux density (fig. 2.10). However, although this model in fact provides

(a) (b)
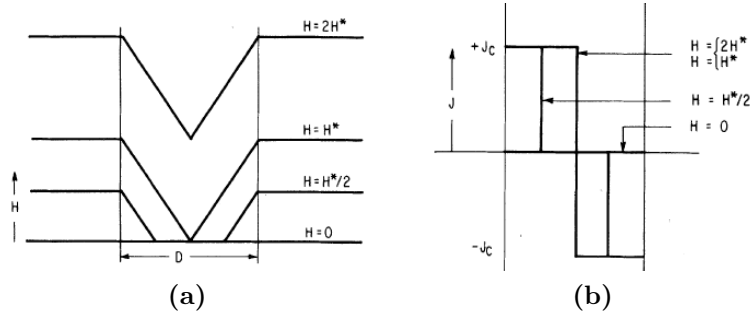
Fig. 2.9: Field penetration in the Bean model[14]. Up to a certain strength H^*, a field applied parallel to a slab with thickness D only partially enters the sample **(a)**. This limit defines the point, where a critical current starts running over the entire object **(b)**.

(a) (b)
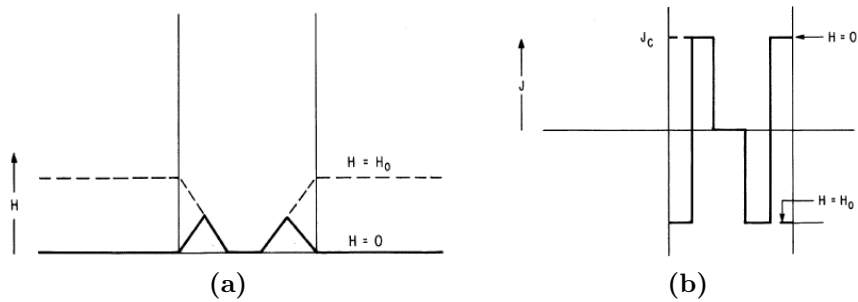
Fig. 2.10: Hysteresis in the Bean model[15]. When an external field penetrating the slab is applied (dashed line in **(a)**) and then ramped down again, a remnant flux can be trapped in near-surface layers. The net current is still zero, but despite the absence of an external field current sheets with opposed sense emerge **(b)**.

---

[14]Bean 1964 [8], fig. 1
[15]Rearranged version of Bean 1964 [8], fig. 2

a proper approximation for several phenomena in hard (type-II) superconductors, it is strongly limited to the introduced geometrical configurations [7, 8].

Perpendicular fields and thin films In typical experimental applications, flat superconductors in perpendicular fields are used. In contrast to the cases considered by the Bean model, here demagnetization effects are no longer negligible, but lead to significant modifications of the current and field distributions. The concept of flux lines moving inwards once the critical current density j_C is reached (cf. fig. 2.9) still applies, but the central flux-free region is shielded by screening currents flowing over the entire width. Moreover, the current density is continuous with a vertical slope at the flux front and drops below j_C everywhere, when the external field H_{ext} or a transport current I_t are reversed. For this reason, the vital condition $|j| \leq j_C$ then already holds throughout the whole specimen, and relaxation leading to a redistribution (as featured in fig. 2.10) is effectively stopped.

In consequence, the response of a superconducting thin film with thickness d to an external magnetic field reveals two different domains within the current distribution: Up to a certain penetration depth, a constant current density $J = J_C = j_C d$ is established, while in the central region $J \leq J_C$. The field distribution is somehow similar to the results of the Bean model (fig. 2.9), but shows a different functional behavior (fig. 2.11a). A bigger difference is caused by the absent relaxation effect. When H_{ext} is first increased to a certain value H_0 and then gradually shifted to $H_{ext} = -H_0$, it will end up in the same state with the signs reversed. All intermediate states, however, are given by current respectively field superpositions depending on the maximum applied magnetic field H_0 (fig. 2.11b). Introducing a new peak field $\tilde{H}_0 > H_0$ furthermore erases the old memory and leads to a distribution dependence on only $\tilde{H}_0$. The same considerations can be transferred to the case of a transport current I_t being applied to the sample, which exhibits the hysteresis behavior as well (fig. 2.12) [10].

(a) [16] (b) [17]
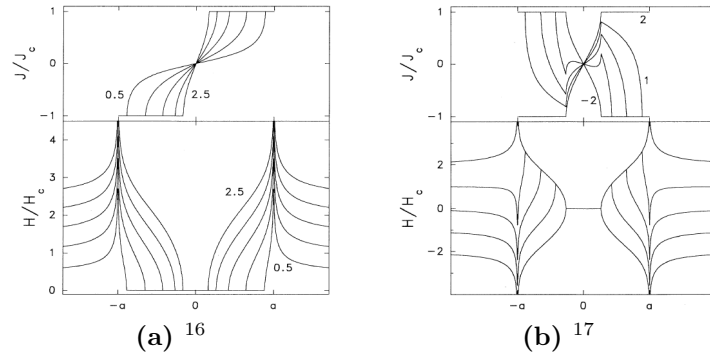
Fig. 2.11: Current and field distribution arising from different perpendicular external fields H_{ext}/H_C penetrating a thin film. If the field is only increased into one direction, a so-called virgin state is established **(a)**. If it is then reversed, the subsequent distributions always depend on the previously reached peak field H_0, implying the existence of a magnetization memory **(b)**. Note that $H_C \neq H_{C2}$, but some quantity proportional to J_C.

---

[16]Brandt et al. [10], ch. III, fig. 3
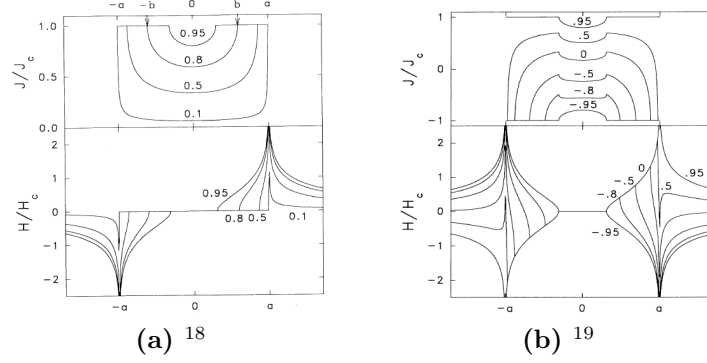[17]Brandt et al. [10], ch. III, fig. 4

Fig. 2.12: Current and field distribution arising from different transport currents I_t/I_{max} in a thin film. The shape of the distributions differs from the case of an external magnetic field (fig. 2.11) **(a)**, but show an analog memory effect **(b)**. The quantity I_{max} marks the point, at which the flux reaches the center of the sample.

As the considered situation applies to a superconducting atomchip, the concepts used for tuning standard atomchip traps cannot be easily adopted. Besides the influence of any previous chip trap parameters, external fields in the vicinity of the chip might already imprint a certain memory. On the other hand, a sufficient analysis of the hysteresis behavior opens up the perspective of tailoring rather complicated current distributions by applying certain current and field sequences, thus allowing for modeling individual magnetic traps. An extensive analytical discussion of the response of thin films compared to slab geometry can be found in [71]. A detailed outlook concerning such material programming in an atomchip wire is given in [17, 50].

2.5.4 Material options

In principle, three different superconducting materials were considered, namely MgB_2, YBCO and Nb. The first one, magnesium dibromide, has a transition temperature $T_C \approx 35\,\text{K}$ and a critical current density $J_C(4.2\,\text{K}) \approx 10^7\,\text{A/cm}^2$. These values make it well suited for application on superconducting atomchips, as could be shown in [48]. The second one, more precisely $YBa_2Cu_3O_{7-x}$ (**y**ttrium **b**arium **c**opper **o**xide), features the advantage of a very high critical temperature $T_C \approx 93\,\text{K}$ and has already been used for chip fabrication too [49]. However, unfortunately its first critical field H_{C1} is rather small (at $4\,\text{K}$ down to $200\,\text{G}$, depending on the orientation). Therefore, the mixed state is reached and flux lines enter the material very fast [41], which is intended to be avoided. Simulations and results for a YBCO atomchip tested at QuIC can be found in [17].

The third material, which was finally chosen for the upcoming measurements, is niobium with a transition temperature $T_C \approx 9.25\,\text{K}$ [1], sufficiently above standard cryostat temperatures as well. In niobium films with widths of a few hundred μm, a critical current density $J_C(4.2\,\text{K}) \approx 3\text{-}7 \times 10^6\,\text{A/cm}^2$ is to be expected [31]. The wires used at QuIC allow for a critical current $I_C \approx 2.5\text{-}3\,\text{A}$ (depending on the temperature). The critical field strengths most importantly exhibit $H_{C1}(\text{Nb}) \gg H_{C1}(\text{YBCO})$ (e.g. $H_{C1}(4\,\text{K}) \approx 1400\,\text{G}$,

---

[18]Brandt et al. [10], ch. II, fig. 1
[19]Brandt et al. [10], ch. II, fig. 2

where due to the different unit system $1\,\mathrm{G} = 1\,\mathrm{Oe}$). Comparison of the magnetization curves found in [22] with fig. 2.8 suggest, that Nb responds to an external field like a type-I/II superconductor. In general its properties can be accurately described as type-II and the concepts introduced so far are supposed to apply. All critical parameters depend on the size of the superconducting energy gap, which vanishes at $T \approx 9.25\,\mathrm{K}$. The gap's temperature dependence below T_C can be obtained from [19]. Inserting the transition temperature into (2.14) yields a $\Delta(0)$ in the same order of magnitude as stated in [36], which lies in the low THz range.

3 Experimental realization

As discussed in ch. 1.2, the QuIC experiment consists of a vast number of different parts. A detailed description and characterization of every single component would definitely go beyond the constraints of this thesis. Furthermore, the various parts have already been discussed in preceding theses [4, 17, 28, 42, 52]. For this reason, this chapter features a rough overview of the experimental setup. It provides a basic description of the preparation of the atom cloud and the superconducting chip for the intended measurements. Special focus is put onto the laser and the quenching setups, which were subject to most modifications of the experiment within the past months (cf. ch. 1.3). A more detailed insight (especially into the highly sophisticated electronics) can be gained by visiting the lab or, preferably, by performing any kind of thesis in the QuIC group[20].

3.1 Overview

By means of several current-supplied dispensers[21], a rubidium background is established in the MOT (**m**agneto-**o**ptical **t**rap, cf. ch. 2.2) chamber. In order to avoid any impurities, this chamber is constantly evacuated by a $50\,\mathrm{L}$ ion pump, providing a pressure of $\sim 10^{-11}\,\mathrm{mbar}$. It is only turned off when the dispensers need to be exchanged, which requires opening the chamber. The construction provides optical access from various directions and is equipped with a pair of MOT coils and several bias coils (fig. 3.1). The laser setup required for cooling the atoms will be described in ch. 3.3.
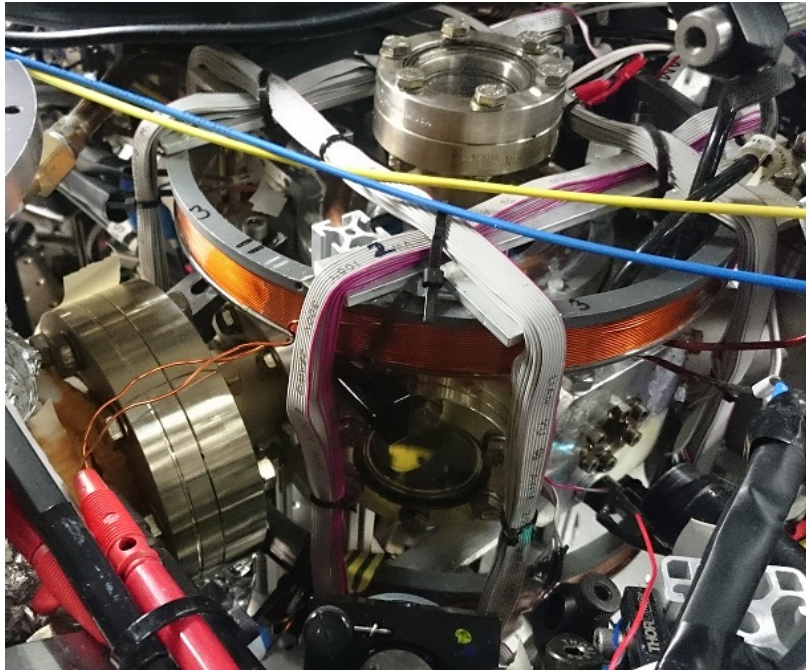

Fig. 3.1: The MOT chamber with plenty of optical accesses and three bias coil pairs mounted outside **(a)**.

The main experimental challenge of the combination of ultracold atoms and superconductors is the transfer of a cold atom cloud from a MOT chamber at room temperature to a science chamber at cryogenic temperatures. On the one hand, operating the dispensers inside a cryogenic environment would not be possible. On the other, the superconducting atomchip must be located in an environment with T well below $T_C(Nb) = 9.25\,\mathrm{K}$ (cf. ch. 2.5.4). Such an atom cloud transport can be accomplished by means of a coil array, which is supplied with a specific current sequence. The basic principle has already been explained in ch. 2.1, the necessary demands and the calculation procedure can be looked up in [28, 42]. The currents are shown in appx. A.1.

The transport coil setup is separated into a normal conducting and a superconducting section. The normal conducting coils are supplied by five "Deltas"[22] (cf. ch. 4.1.1), which run currents up to $150\,\mathrm{A}$ through coils of about 40 windings. The superconducting part consists of coils with around 3000 windings, which is why currents in the range of $1\,\mathrm{A}$ are sufficient for providing the needed magnetic field strengths and gradients [28, 52] (as the magnetic field $B \propto NI$, number of windings times current strength). The reason for this implementation is the limited cooling power in the low temperature part. The use of superconducting niobium wires (cf. ch. 2.5.4) significantly reduces the heat production and allows for a distinctly higher number of windings due to the vanishing resistance (cf. ch. 2.5.2). The current feedthrough from the outside into the cryogenic environment will be shown in ch. 3.4.1. The normal conducting part is water cooled, e.g. fig. 3.2.

Another demand resulting from the special setup is the possibility to isolate the cryogenic part from the MOT chamber. There are already design considerations for splitting up the whole transport line into several parts, but for now there is a single transport valve that needs to be closed before turning the cryostat off or breaking the vacuum inside the low temperature part (fig. 3.3). The latter is necessary from time to time due to maintenance work on the science chamber (see ch. 3.4.1). When the atoms reach this chamber, they need to be prepared for loading onto the atomchip. A standard technique is utilizing a so-called QUIC (**qu**adrupole-**I**offe-**c**onfiguration) trap combined with rf (**r**adio **f**requency) cooling [20], which will be explained in ch. 3.4.2. The trap is formed by a pair of anti-Helmholtz coils and a third coil, whose symmetry axis is perpendicular

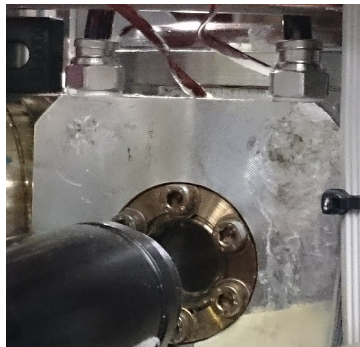**Fig. 3.2:** Water cooling of the push coil. When running the experiment, cooling water needs to be permanently flowing through the black hoses. This way, all the normal conducting coils can be protected from too fast heating. This picture additionally shows the MOT live cam (see ch. 4.1.3) looking into the chamber through a small window.

---

[22]Delta-Elektronika SM3000 series power supplies
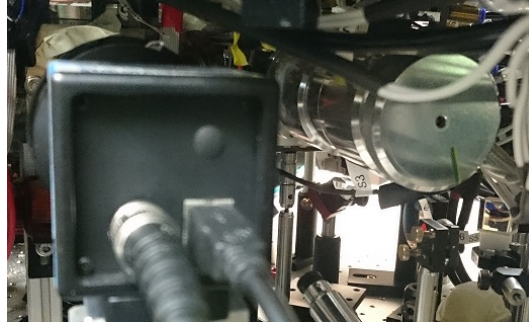
Fig. 3.3: The transport valve. Whenever the cryostat is turned off (and for safety reasons at the end of each lab day), the valve must be closed, otherwise the vacuum in the MOT chamber might get destroyed. Conversely, before transporting atoms further away from the MOT setup than a few cm, it needs to be opened. For orientation the MOT camera (see ch. 3.3.2) left to the valve was kept in this picture too.

to the common one of the coil pair. Moreover, bias fields in all directions are needed during the chip loading sequence respectively for forming a chip trap, see ch. 3.4.3. A cross-section of the basic setup including a mounting for the superconducting atomchip is shown in fig. 3.4.
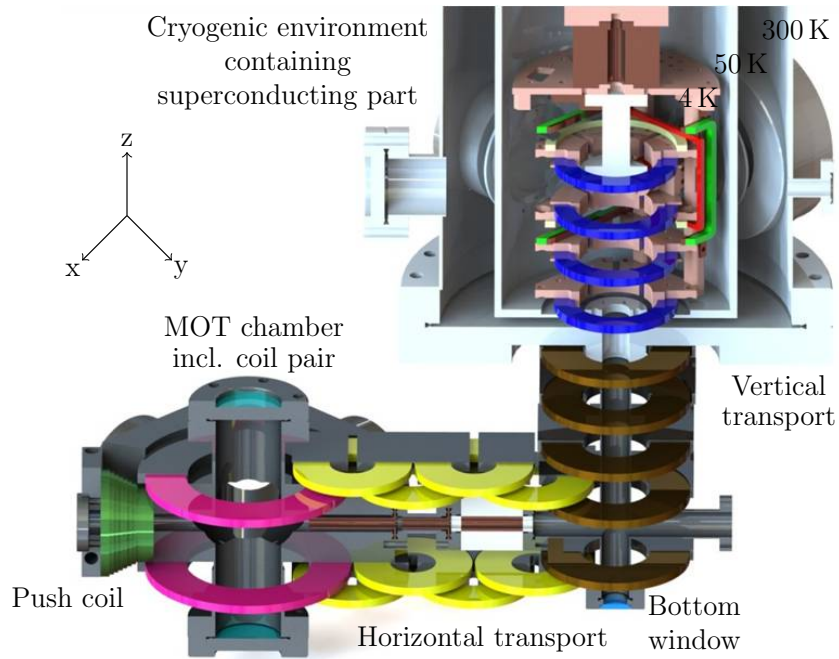
Fig. 3.4: Setup overview showing the MOT chamber with the two big coils, the entire transport line with a push coil moving the atoms towards the first transport pair (cf. ch. 2.1), and the bias coils in the science chamber. Together with a small perpendicular coil, the last two transport coils are used to form the QUIC trap for further cooling. The chip mounting facing the center of the science chamber is depicted in white. The axes drawn here must not be confused with the ones assigned to the MOT setup. They are defined with respect to the science chamber setup.

3.2 ADwin control

For achieving a timing accuracy in the range of microseconds, a control software combined with proper hardware is inevitable: At the QuIC experiment (as for most experiments within the group), the "ADwin"[23] system is used, which (in our case) is able to output voltage sequences via 32 analog and 64 digital channels. These channels can be programmed on a PC in various ways, using one of the standard programming languages, e.g. "Matlab"[24]. The output signals supplied via channel boxes (fig. 3.5) can then be utilized to control the variety of different devices active during an experimental cycle, providing a time resolution down to 300 ns. For the needs of the QuIC experiment, an accuracy of $\sim 25\,\mu$s is sufficient. A detailed discussion of the software programming and the channel properties is given in [52], how the magnetic transport was implemented is explained in [42].

Choosing and varying the parameters necessary for optimizing and characterizing the experiment's performance is done via a graphical user interface designed in Matlab. There are a few different versions of this interface, depending on the kind of measurements one wants to perform: It is possible to only consider the trapping and cooling phase, to transport the atom cloud to a defined position and back into the MOT chamber, and to do measurements in the science chamber. In addition, there are various save files of the same interface type, but with slight changes in preselected values or in single channels. A detailed description of the different **g**raphical **u**ser **i**nterfaces (GUI) will be presented in ch. 4. An explanation of the different control windows and a guideline for modifying the interfaces are given in appx. B.2.

3.3 Laser setup

The extensive laser setup consists of three lasers (not counting the completely independent quenching laser, which will be discussed in ch. 3.5). The first one to be explained is called "Pierluigi" and used as a reference for the main laser. It is an ECDL (**e**xternal **c**avity
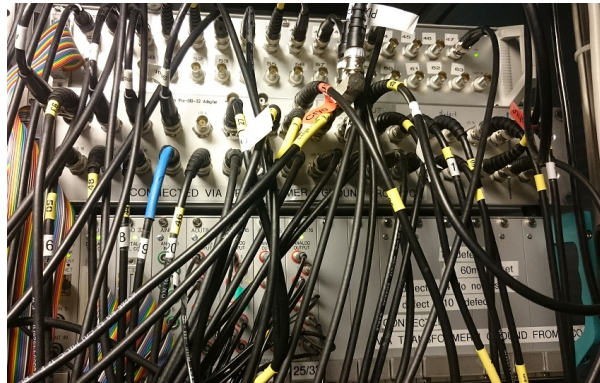

Fig. 3.5: The ADwin output boxes in the lab. All the control signal originate from here, mostly just controlling other devices like current sources or shutters. The upper two boxes provide digital signals, the lower one analog voltages between -10 and $+10\,$V.

---

[23]Jäger GmbH, `http://www.adwin.de/`

[24]MathWorks, `https://www.mathworks.com/products/matlab.html`

diode laser), where a diode is combined with an optical grating, which can be moved by means of a piezo actuator. Adjusting this grating results in a variation of the resonator length and therefore the frequency; for a detailed description refer to [27]. The main laser, the "TA (tapered amplifier) master", is used for the main cooling transition, for optical pumping and imaging. It consists of a seed laser – which is also an ECDL – and an optical amplifier, a combination usually providing a high power beam at a narrow linewidth. The TA master is mixed with the Pierluigi and its frequency then shifted in relation to the frequency of the reference (which therefore needs to be stabilized beforehand, ch. 3.3.1). The repumper, called "Rudi", is a DFB (distributed feedback) laser, where the grating is formed in the gain region, thus being frequency-shifted only by varying the injection current. Some information on the working principle can be found in [39]. The Rudi is completely independent and its output simply mixed into the cooling light, always staying at a fixed frequency.

3.3.1 Laser light preparation

The different frequencies, to which the lasers must be tuned during an experimental cycle, have already been shown in fig. 2.7. Since everything but repumping is implemented with a single light source, a tuning range of at least $267\,\mathrm{MHz}$ downwards from the $5^2\mathrm{S}_{1/2}, F = 2 \rightarrow 5^2\mathrm{P}_{3/2}, F' = 3$ transition is required. However, those are only theoretical considerations and can only serve as a basis for the locking scheme. It is necessary to provide a broader range (extended in both directions).

Frequency tuning   A standard way of performing frequency shifts in the MHz regime is using AOMs (acousto-optic modulators). In such devices, an oscillating signal induces a sound wave in a crystal via a piezoelectric transducer (fig. 3.6). Incoming light is diffracted into several orders, where the (periodic) frequency shifts between the different orders are determined by the frequency of the supplied radio frequency signal. The biggest disadvantage of this approach is the dependence of the diffraction angle of any order $n \neq 0$ on the frequency shift. Consequently, adjusting the latter requires adapting the alignment, which is by no means possible during an experimental cycle. On the plus side, turning the AOM driver off respectively on allows for switching between the zeroth and one of the higher orders, which follow different beam paths. A detailed discussion of the working principle of an AOM including a description of a double-pass setup can be found in [18].
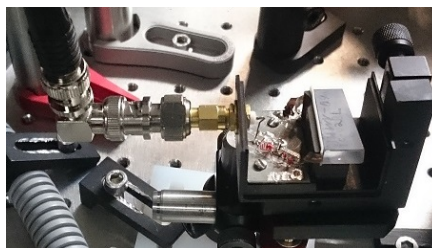

Fig. 3.6: One of the AOMs used at QuIC. The device receives a radio frequency signal from a driver via a BNC cable and the electronics convert it to a sound wave in the crystal, through which the light is propagating.

In order to switch between the different laser cooling phases and imaging, it is necessary to shift the laser frequency without messing up the alignment. This cannot be solved by any optical element, but by an electrical device employing a special locking technique. Here the reference laser comes into play: As outlined above, the frequency-stabilized output beam of the Pierluigi is mixed with the TA master, upon which the latter's frequency can be continuously shifted with respect to the reference.

Reference laser In accordance with fig. 2.7, the desired frequency range is given by the $5^2S_{1/2}, F = 2 \rightarrow 5^2P_{3/2}$ transitions including the cross-over peaks. The required spectroscopy signal is obtained by means of Doppler-free FM saturated absorption spectroscopy (cf. ch. 2.3). This technique was implemented using a double-pass setup with a rubidium vapor cell and two parallel beams. One of them enters a PD (**p**hoto**d**iode) for depiction on an oscilloscope, and the other one is directed into an APD (**a**valanche **p**hoto**d**iode) for further processing. An FM-lock card applying the frequency modulation to the laser generates an error signal proportional to the derivative of the spectroscopy signal. This error signal features zero crossings at the extrema and a sign depending on whether the frequency moves to the left or the right with respect to a resonance. It is fed into a PID (**p**roportional-**i**ntegral-**d**erivative) controller, which continuously tries to minimize the error, i.e., the deviation from the setpoint, once the laser is locked. In order to achieve this, the controller automatically adapts some control variable via an electronic feedback loop. In the case of the Pierluigi, this is the piezo voltage steering the grating. What the signals (including a trigger needed for locking) look like on an oscilloscope is shown in fig. 3.7.

Frequency offset lock The main laser is not locked directly to a rubidium spectroscopy. Utilizing the reference laser, the locking technique aims at attaining a frequency-
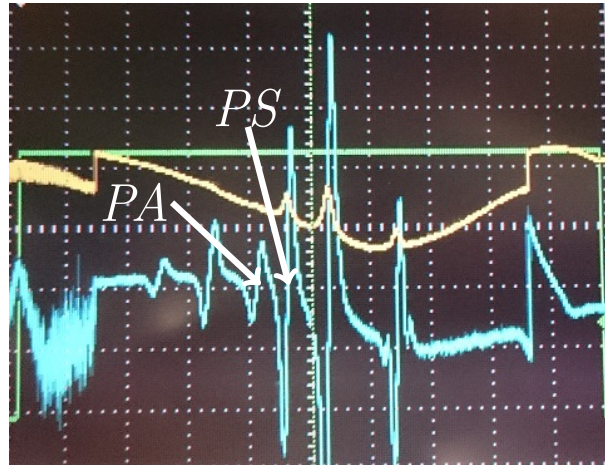

Fig. 3.7: Spectroscopy (yellow) and error (blue) signal of the Pierluigi. The laser can be locked to one of the error slopes, upon which the PID controller will try to compensate for any deviations from the selected zero crossing. Therefore, a higher slope implies a more stable lock. In the standard scheme, point *PS* is selected. How to lock the laser will be explained in ch. 4.1.1.

stabilized light source with a variable offset to the reference. A so-called FO (**f**requency **o**ffset) lock can provide the desired feature: In contrast to a conventional FM lock, here the error signal is generated from a beat note, arising from the overlay of two beams with slightly different frequencies. Although it is not used for frequency stabilization, a rubidium vapor cell is included in the TA master setup, so that the laser frequency can be shifted sufficiently close to the transition, to which the Pierluigi is locked. This condition is fulfilled, when the same section of the rubidium spectrum can be observed on an oscilloscope (fig. 3.8).

The mixed beams are directed onto an APD, from where the beat signal is transferred to an FO-lock card. Since the sum frequency is too high to be detected by the diode, the resulting voltage oscillates with the difference frequency $\Delta\nu = |\nu_1 - \nu_2|$. On the card, this signal is mixed with the output of a VCO (**v**oltage **c**ontrolled **o**scillator) with a frequency range of $\sim 126\,\mathrm{MHz}$. The oscillator currently in use can be tuned by applying a voltage between -10 and $+10\,\mathrm{V}$ and has a center frequency $\nu_{VCO}(0\,\mathrm{V}) \approx 120\,\mathrm{MHz}$. The mixture of beat and VCO signal is first low-pass filtered, in order to get rid of the sum frequency. Next, it is split into two equal parts and then recombined after adding a time delay τ to one of the paths. A phase detector can measure the resulting phase shift

$$\Delta\Phi = 2\pi\left(\Delta\nu - \nu_{VCO}\right)\tau = 2\pi\Delta\nu_{FO}\tau, \tag{3.1}$$

which depends on the new difference frequency $\Delta\nu_{FO}$ and the delay. The output of the detector varies as $\cos\left(\Delta\Phi\right)$ and, after being low-passed again, serves as an error signal for the main laser lock (fig. 3.8). The different peak heights stem from the limited bandwidth of the phase detector [60]. Feeding the error signal into a PID regulator allows for locking the TA master to one of the zero crossings (the feedback loop works just the same way as for the Pierluigi). As can be inferred from (3.1), each of these locking points corresponds to a certain frequency offset $\Delta\nu$. This offset can be measured by looking at the FFT (**f**ast **f**ourier **t**ransform) of the beating on an oscilloscope. In this manner, the beat note is on the one hand used to generate the error signal, and on the other its fourier transform indicates $\Delta\nu$, once the main laser has been frequency-stabilized.

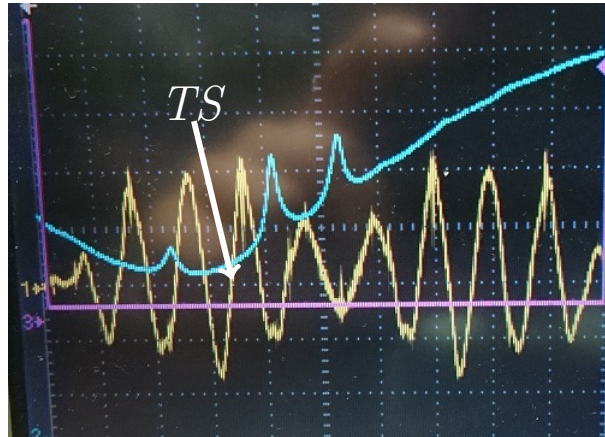During an experimental cycle, the laser must stay locked, while the frequency needs

Fig. 3.8: Spectroscopy (blue) and error (yellow) signal of the TA master. Each zero crossing corresponds to a certain offset to the reference laser. The standard lock point is labeled *TS*.

to be shiftable. This is where the VCO is employed: When ν_{VCO} is varied, the feedback loop tries to keep the error signal as close to zero as possible. As the regulator aims at keeping $\Delta\nu_{FO}$ constant, this results in a change of $\Delta\nu$. Since ADwin can provide an analog signal covering the input range of the oscillator (-10 to $+10$ V, cf. fig. 3.5), the program can this way be utilized to tune the locking point. A very important constraint of this technique is the limited timing latitude, which has to be considered in the voltage ramp speed. Since most changes happen in the regime of ms, the laser might simply fall out of lock at any point during an experimental cycle. As described in ch. 5.1, this is a typical reason for not observing atoms in the trap, so the ramps must be optimized in duration.

Locking scheme   The optimal locking scheme depends on the hyperfine rubidium transitions, the AOMs plus drivers at hand, the available FO locking points, and the VCO's tuning range. With the given preconditions, it seems most reasonable to lock the Pierluigi to the $F = 2 \rightarrow COF' = 1,3$ cross-over resonance (labeled *PS* in fig. 3.7), and the TA master to $\Delta\nu_0 = \Delta\nu(\nu_{VCO} = 120\,\mathrm{MHz}) = 139\,\mathrm{MHz}$ (labeled *TS* in fig. 3.8). As the cooling respectively optical pumping phases are separated in time, an AOM can be utilized for splitting the main beam into two parts. While the cooling beam experiences a $+62.5\,\mathrm{MHz}$ shift, for the pump beam the zeroth order is used. It is even shifted further down by $-2 \times 80\,\mathrm{MHz}$ due to another AOM in double-pass configuration. Optical power is not a problem, since the modulator is simply either on or off. The entire AOM setup will be shown in fig. 3.12.

During the course of the experiment, the locking scheme was temporarily modified. This seemed necessary due to some unexpected frequency shift, upon which the required pump detuning had obviously fallen below the lower limit of the accessible frequency range. In order to tune the latter, the Pierluigi was locked to the $F = 2 \rightarrow F' = 2$ transition. Combined with a slight variation of the locking setpoint, an overall laser frequency shift of $\sim -47\,\mathrm{MHz}$ could be implemented. A detailed discussion of this alternative locking scheme and its drawbacks concerning the lock stability is given in appx. C. Since it was possible to resolve the problems with the optical pumping (see ch. 5.3), the original locking scheme was finally restored.

Detuning calibration   Since ν_{VCO} and with it the offset frequency $\Delta\nu$ is controlled by ADwin, it is necessary to calibrate the analog output by converting frequency into voltage. If then a detuning δ is defined in the control program, the lock point is shifted by exactly the selected frequency. An accurate calibration curve was acquired by manually applying various voltages to the VCO. The corresponding oscillator and beat frequencies could be recorded by using the *Monitor* output of the FO-lock card. After fitting the obtained data (with a 12$^{\text{th}}$ order polynomial), the calibration was defined in the corresponding Matlab file. The latter is opened upon pressing the *calibrate* button on the respective channel in the user interface, as explained in appx. B.2.1. The created data table can be found in appx. D.

Repump laser   The remaining laser is the Rudi, used for rempumping. In order to stabilize it to the target frequency denoted in fig. 2.7, it is locked to the $F = 2 \rightarrow COF' = 1,2$ cross-over peak, which features the highest slope in the error signal (fig. 3.9).
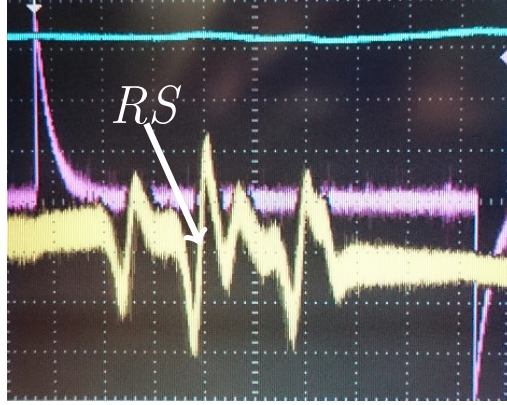
Fig. 3.9: Spectroscopy (blue) and error (yellow) signal of the Rudi. The slope it needs to be locked to is labeled RS.

An AOM then shifts the frequency upwards by $+78.5\,\mathrm{MHz}$, approaching the $F = 1 \rightarrow F' = 2$ transition. The spectroscopy setup and the locking technique are the same as for the reference laser, but the control variable being adjusted to minimize the error signal is as different one: As the Rudi is a DFB, there is no external grating and the PID controller employs the diode current. The resulting frequency budget covering the entire experimental cycle is shown in fig. 3.10.

Laserbox The three lasers are located inside a box, whose lid is only taken away for modifications of the setups. The box shields the latter from acoustic noise and improves the temperature stability. Each of the three lasers is equipped with a temperature control, which measures and regulates the temperature of the laser crystal via a Peltier element below the diode mounting. The resistance acquired by an NTC (**n**egative **t**emperature **c**oefficient) thermistor can be adjusted in order to shift the frequency. The effect is similar to changing the current, but the response time is longer [4]. While the AOMs are located in the "free" setup, which will be described in ch. 3.3.2, the whole spectroscopy part including the mixing of the Pierluigi and the TA master is protected from the outside. In this manner, all the signals depicted in figs. 3.7, 3.8 and 3.9 originate from the setups inside the box. Some feedthroughs for cables and optical fibers are necessary, and the main beam leaves the laserbox through a hole cut into the wall (fig. 3.11). The frequency-stabilized repump beam is directed to the optical setup through a fiber.

3.3.2 Optical setup

Besides the detuning δ, the ADwin program controls the AOMs (explained in ch. 3.3.1) and some optical shutters. The response time of the AOMs used is $\sim 100\,\mu\mathrm{s}$, which makes them well suited for switching between the different optical paths: All the beams entering the MOT or the science chamber originate from non-zero orders, so providing the related drivers with TTL (**t**ransistor-**t**ransistor **l**ogic) signals allows for effectively turning on and off the beams. The shutters have considerably longer response times ($\sim$ 1-5 ms), but prevent unwanted light from leaking into the chambers. An overview of the complete laser setup (outside the laserbox) is given in fig. 3.12.
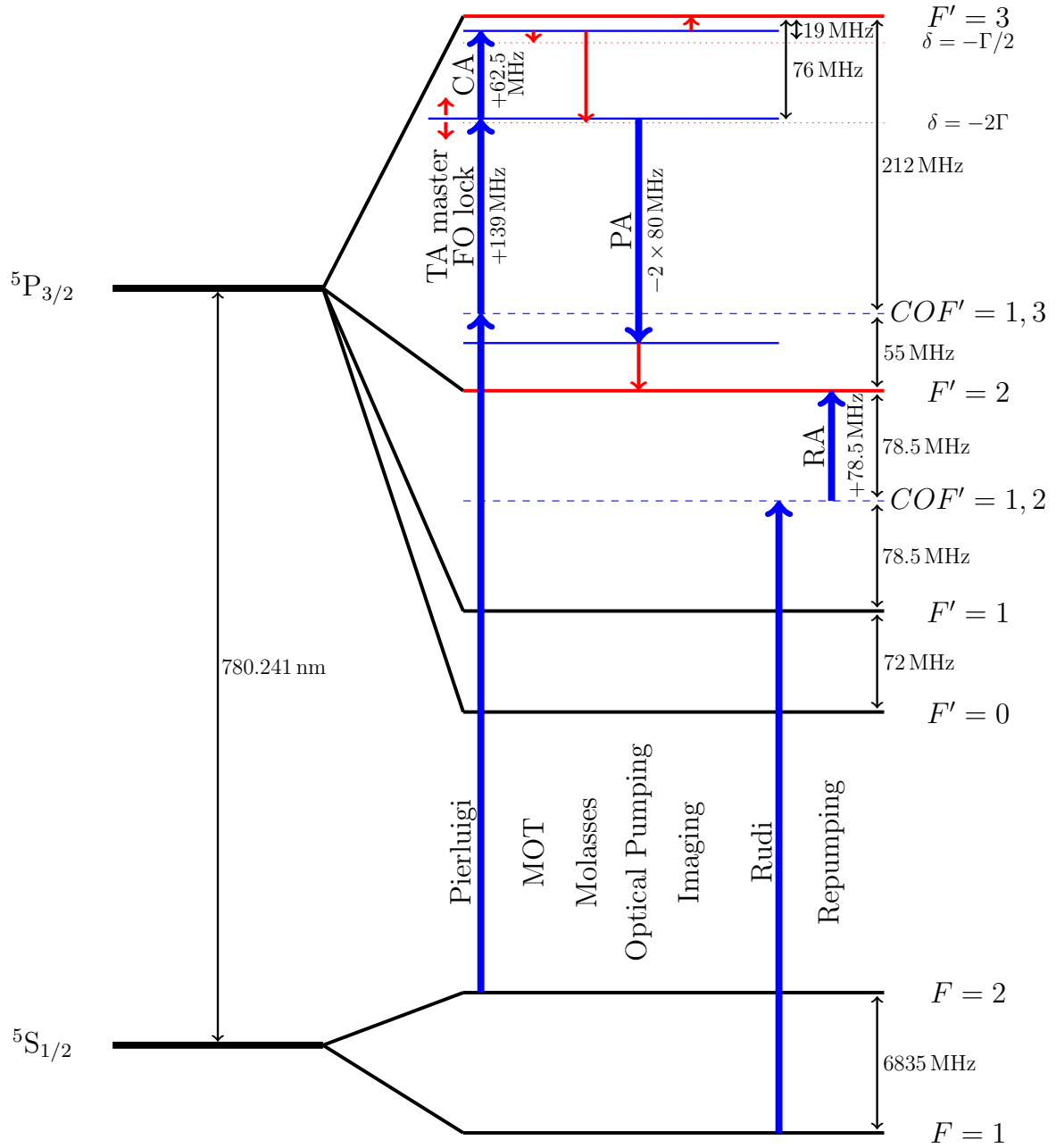
Fig. 3.10: The entire frequency budget of the laser setup. It features the standard locking scheme for the Pierluigi and the TA master. The red lines mark the frequencies needed in the different experimental phases (denoted below). The red arrows indicate a shift of the frequency offset ($\sim \pm 63\,\mathrm{MHz}$), which can be treated as a detuning from the $F' = 3$ level. For optical pumping the Pump AOM "PA" needs to be taken into account instead of the Cooler AOM "CA". The detunings must be optimized by monitoring the atom cloud properties, but are expected to be close to the values given here. Slight deviations will occur most of all due to the presence of magnetic fields. The repump beam is completely independent and employs the Repump AOM "RA".

34
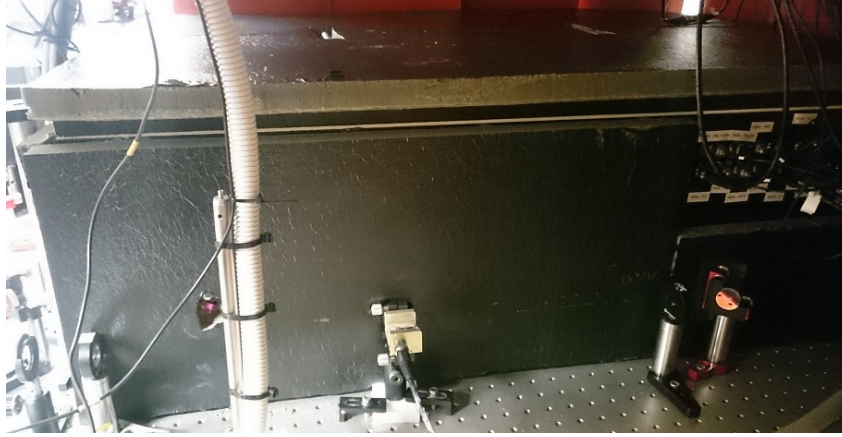
Fig. 3.11: Rear view of the laser box. The hole, through which the main beam leaves the box, is discernible on the left side.

Beam paths   The optical setup can be divided into different paths being "active" at different points in time during the experimental cycle. In the cooling phase, the light needs to take paths *1a* and *3* (in fig. 3.12) to the MOT chamber: The Cooler AOM is on, the Pump AOM off, shutter *A* is open, while shutters *B* and *C* are closed. Furthermore, the Repump AOM is on as well and shutter *D* open. Next up is the pump phase, where the light is has to take paths *2* and *3* (some repump light is added): The Cooler AOM is off, the Pump AOM on, shutter *A* is closed. The repump configuration stays the same. The imaging settings depend on where the atoms are intended to be observed, so either path *1b* or *1c* is used: For both cases, the Pump and the Repump AOMs are off, shutters *A* and *D* are closed. The Cooler AOM is employed as a light switch, which is needed for the imaging process. It is combined with either shutter *B* (for the MOT chamber) or *C* (for the science chamber).

MOT chamber light   The magneto-optical trap setup is straightforward (cf. ch. 2.2), but, due to certain constructional constraints, the implementation could be less complex. As already indicated in fig. 3.12, the expanded beam is split into six fractions by means of five half-wave plate plus PBS combinations (fig. 3.13). Although the quarter-wave plates cannot be placed right in front of the windows, attaining a sufficiently circular polarization on all axes is possible. The optical trap setup (alignment, power and polarization adjustment) is explained in ch. 5.2.

Fig. 3.12 also shows the beams used for optical pumping and for imaging, which enter the MOT chamber along the same axis. For attaining a picture of the atom cloud, standard absorption imaging is used. A variable TOF (**t**ime-**o**f-**f**light) in the range of ms determines the time interval between the moment the trap is turned off and the first picture. A high performance CCD camera placed on the opposite side is used for acquisition. This MOT camera has already been depicted in fig. 3.3. A more detailed explanation of the used absorption imaging technique is given in fig. F.1. Imaging the atoms in the science chamber follows the same principle, but features different configurations (see ch. 3.4.4).

Fig. 3.12: Complete optical setup outside the laserbox. In the bottom left corner, the first part of the MOT setup is depicted: A telescope expands the beam consisting of cooling and repumping light. This widened beam is then split into six ones and directed towards the MOT chamber. Right to it, the MOT imaging beam is shown, which enters the chamber through the same window as the optical pump beam. The latter is circularly polarized by means of a quarter-wave plate. The different beam paths, the AOMs and the shutters are labeled. Moreover, some of the irises will be referred to when explaining the alignment procedure.

Fig. 3.13: The MOT beam setup. By means of the five half-wave plates and the six cubes, the expanded beam approaching from the left is split into six equally strong and linearly polarized parts. Before entering the MOT chamber, each one is circularly polarized by a quarter-wave plate (four of them discernible in this picture). The half-wave plates are labeled because proper settings for each of them are denoted in appx. E.

3.4 Science chamber

As described in ch. 3.1, the atom cloud is transported into a cryogenic environment, that provides temperatures of $\sim$ 4-6 K (cf. ch. 2.5.1). The last part of the transport coil setup (V6 to V9) is superconducting, which is why it is integrated into the cooled science chamber. The heart of this upper chamber is the coil cage, where all superconducting coils and the atomchip are mounted. All these components need to be supplied from the outside, which is solved by separating the current lines into three parts each: Via special multipin feedthroughs, the currents are fed into the cryostat (fig. 3.14). Normal conducting copper wires are used for transferring them to commercial HTCs (**h**igh **t**emperature

Fig. 3.14: Current feedthrough into the cryostat by means of special multipin connectors.

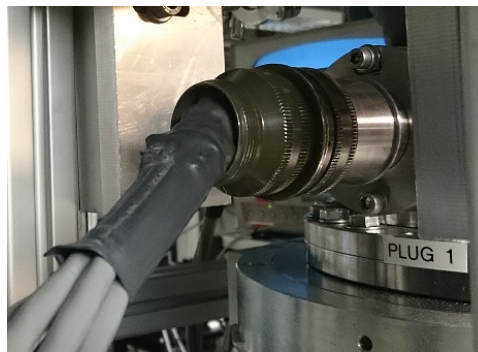superconductors), which promise high performance up to $77\,\text{K}$[25] and lead downwards to the cage baseplate. This plate marks the top of the coil cage and is connected to the coldfinger of the cryostat. It is therefore cooled down to $4\,\text{K}$, while everything above it has higher temperatures. The superconducting niobium wires (cf. ch. 2.5.4) of the coils respectively the chip are soldered to the ends of the HTCs. An overview of the current supply line inside the cryogenic environment is given in fig. 3.15a. As it is necessary to monitor the temperature inside the upper chamber, temperature sensors must be connected to the outside as well (fig. 3.15b).

The cryogenic environment is protected by different shields constituting different temperature stages (cf. fig. 3.4). The outermost cylinder (fig. 3.16) is at room temperature. The next stage is an aluminum shield, which provides good thermal conduction, but is not as prone to eddy currents as copper. It is covered with aluminized mylar for thermal radiation shielding (fig. 3.17a) and its temperature is $\sim 50\,\text{K}$. Right behind it, but additionally covered with insulating Kapton tape, mylar and Teflon tape, the lines shown in

(a)   (b)
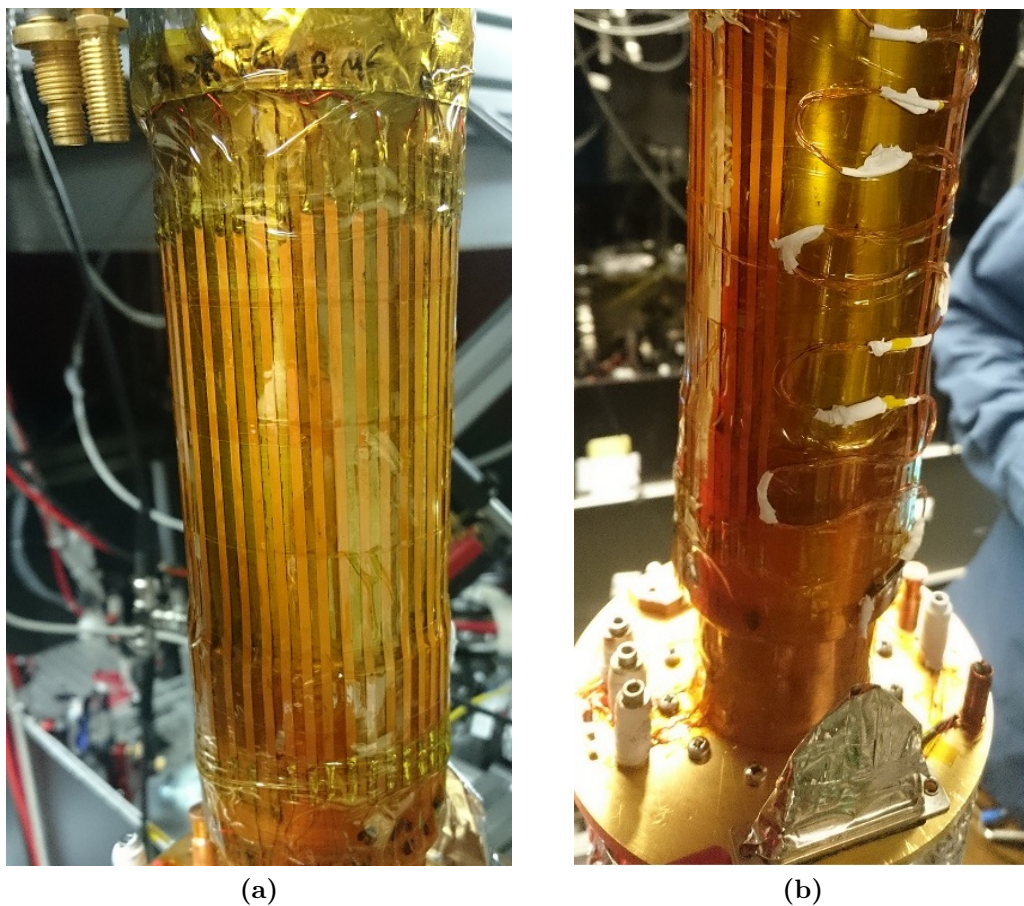
Fig. 3.15: Supply line towards the $4\,\text{K}$ regime. Normal conducting wires coming from the multipin connectors are soldered to flat HTCs, which run almost down to the baseplate. The superconducting niobium wires are soldered to the open ends **(a)** and supply the coils and the chip. For monitoring the temperature of the coil cage, the sensor signals merged on a Sub-D plug need to be guided to the outside **(b)**.

---

[25]SuperPower Inc. 2012 [2]
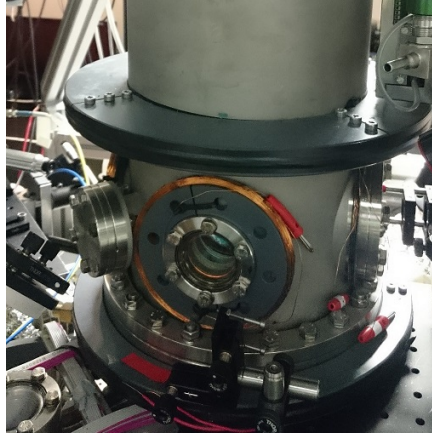
Fig. 3.16: Optical access to the outermost shield of the cryogenic environment.

fig. 3.15 are located. The outer Teflon layer is discernible in fig. 3.17b, where the coaxial wires supplying the rf coils (see ch. 3.4.2) and the 4 K shield (see ch. 3.4.1) are depicted as well.
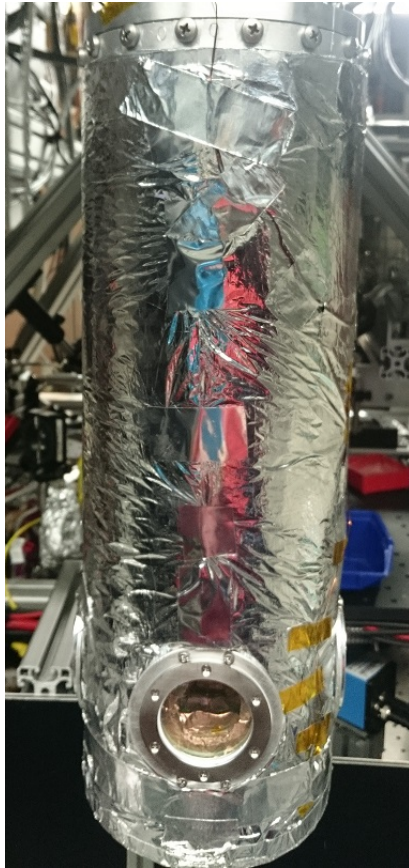
(a)   (b)

Fig. 3.17: The inner temperature stages. The 50 K shield is equipped with a separate temperature sensor, whose wire is discernible in **(a)**. Behind it, the feedthrough lines for the currents and the rf signals, and the 4 K shield are located **(b)**.

The science chamber is evacuated by means of a turbo pump. The setup was recently redesigned and is now permanently mounted to the corresponding chamber access. The strong vibrations created by the backing pump are sufficiently damped (fig. 3.18). The pressure in the chamber can be constantly monitored by a PC program (see ch. 4.1.3).

3.4.1 Coil cage

The 4 K shield covers everything below the cold baseplate and was redesigned, in order to improve the cooling performance. It was the first 3D printed part at QuiC. It is wrapped with two layers of mylar with some spacers in between and aluminum tape. The windows and a lens were mounted with superglue and aluminum tape (fig. 3.19). So far, the material has already survived several warm-up and cool-down cycles. Therefore, several

(a)   (b)
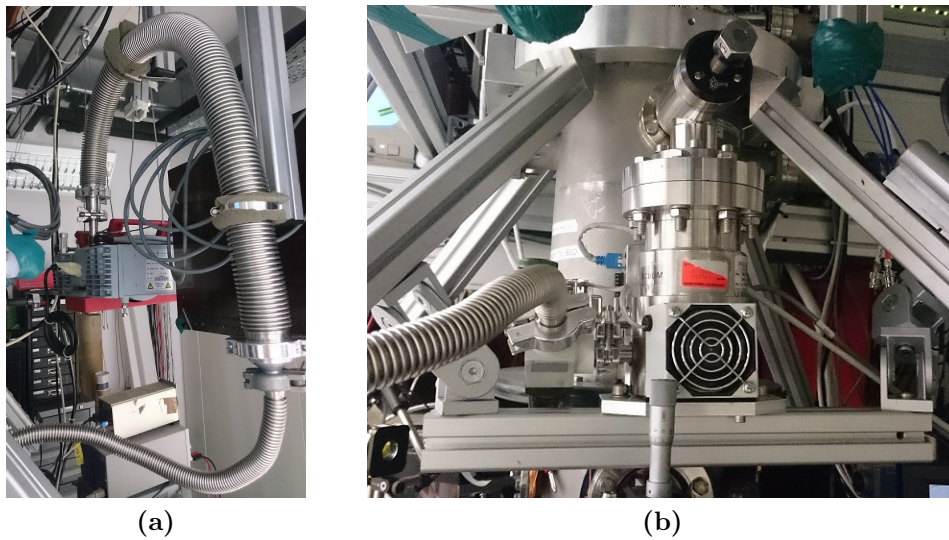
Fig. 3.18: Permanent installation of the vacuum pumps. The backing pump is hung from the ceiling and its vibration damped at two spots **(a)**. The turbo pump is mounted directly to the access valve, which is discernible at the top of **(b)**.
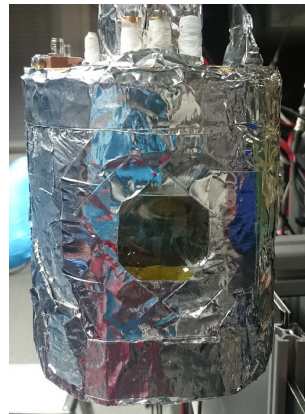
Fig. 3.19: The inner shield at 4 K. It is mounted to the baseplate by means of two screws. Three windows and one $f = 50$ mm lens provide optical access. Below the thermal insulation, a 3D printed part is hidden.

more 3D printed pieces are currently being planned. The new shield will be discussed in more detail in [46].

Without the shield, the coil cage is visible, which is covered with aluminum tape (fig. 3.20a). The Z-wire is visible from the bottom, as shown in fig. 3.20b. The wires run through the baseplate through drilled holes. Since everything not being in direct contact with the coldfinger is considerably warmer, they need to be properly anchored. Otherwise, the coils can possibly quench (cf. ch. 2.5.2), which, in the worst case, can lead to a cable fire. The wire arrangement was recently renewed and is shown in fig. 3.21. So far it seems to provide sufficient thermal conduction, while still electrically insulating the wires from the plate and from each other. The coil cage is equipped with three temperature sensors,

(a) (b)
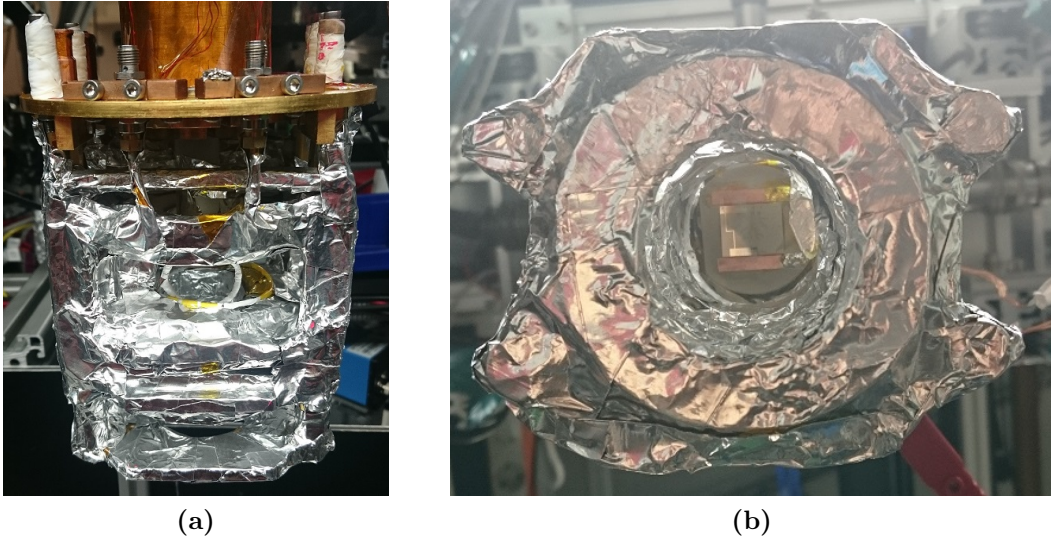
Fig. 3.20: The coil cage. Everything is covered with aluminum tape, so it is not possible to see the superconducting wires. The rf coils covered with Teflon tape are easily discernible **(a)**. From the bottom, it is even possible to view the chip with the Z-wire **(b)**.
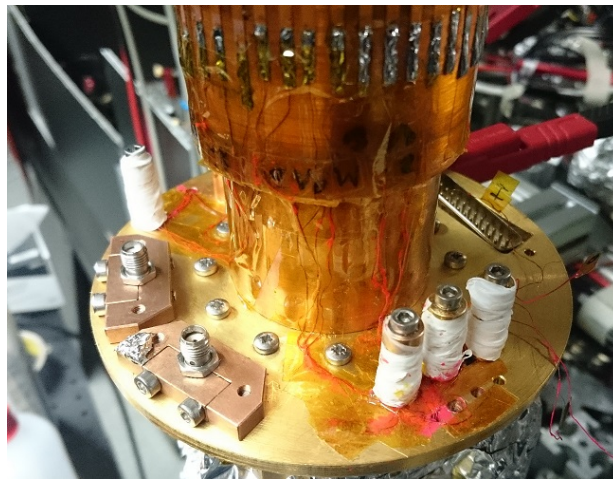
Fig. 3.21: Recently renewed thermal anchoring. Since $T_C(\text{Nb}) \approx 9.25\,\text{K}$, which is not so far above the cryostat operation temperature, all the wires need to be in good thermal contact with the baseplate. This picture was taken before finishing all connections.

surveilling the baseplate (sensor B), the coldfinger (A), and the lowermost coil (C on V6). Again, a PC program allows for real-time acquisition. This way, before running any currents through the superconducting coils, one can check, whether the temperature is well below the the critical point of niobium. When a certain threshold is exceeded, another program outputs an audible alarm (see ch. 4.1.3).

3.4.2 Transfer to the QUIC trap and rf cooling

Once the atoms reach the uppermost part of the coil cage, they need to be further cooled, in order to prepare them for loading onto the atomchip. The utilized setup, which has already been briefly described in ch. 3.1, is shown in fig. 3.22. The first phase after the end of the transport is a buffer trap using BV8 and BV9, while coils V8 and V9 are ramped down and connected in series (for details on the connections refer to [17]). The resulting QUIC series configuration is then ramped up again simultaneously with the Ioffe coil, where the ratio between the two supply currents is variable (see ch. 4.4.2). The symmetry axis of this third coil is perpendicular to the common axis of the other two. It produces an inhomogeneous field, which modifies the standard quadrupole field created by the anti-Helmholtz coils. While the minimum of a quadrupole trap is given by $|\vec{B}| = 0$, the altered trap configuration aims at creating a non-zero trap bottom. Loading into the chip trap demands a strongly compressed cloud, so the atoms necessarily come closer to the field minimum. In a very weak field, they can lose their quantization axis and switch to high-field-seeking states, eventually being lost from the trap (cf. ch. 2.1). In a QUIC trap generated by combining the three coils, the magnetic potential is deformed and can be transformed into a harmonic one with a trap bottom $|\vec{B}| > 0$ (fig. 3.23). Lifting the trap minimum can prevent the unwanted Majorana losses. The created potential features two different trapping frequencies and therefore results in an elongated atom cloud. The frequencies can be determined by slightly deflecting the atoms and measuring the oscillation frequency, which will be shown in ch. 4.4.3. The lifetime in the superconducting QUIC trap is rather long (in the order of 100 s), which is

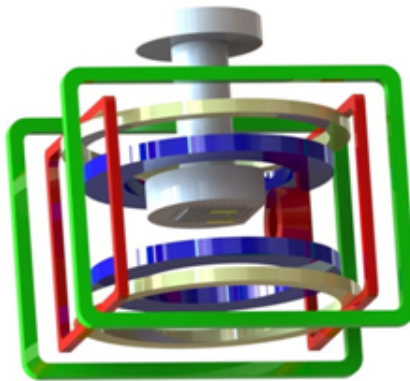**Fig. 3.22:** Coil setup inside the science chamber including the atomchip. The blue coils are V8 (bottom) and V9 (top), the last two transport coils. Together with the small Ioffe coil in red they form the QUIC trap. BV8 (bottom) and BV9 (top) in creme are used for the buffer trap. The other bias coil pairs are called HBIO (red) and HBIM (green). The chip mounting with a symbol chip on it is depicted in white.
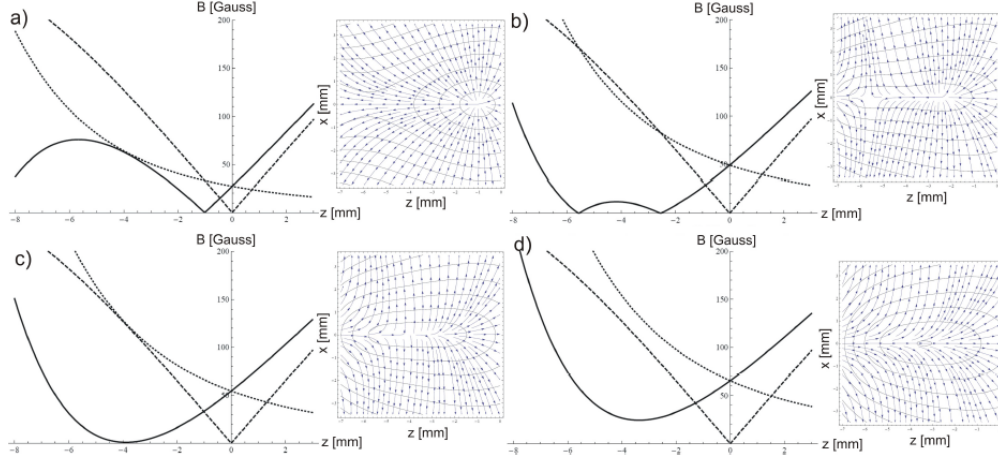
Fig. 3.23: Forming a QUIC trap[26]. The linear quadrupole trap with zero trap bottom is superimposed with an inhomogeneous field. For proper settings, an almost harmonic trap with a minimum greater zero can be formed, the bottom being shifted in space.

why this setup is perfectly suited for time-consuming cooling processes [20, 28, 52].

At this point, laser cooling is not sufficient any more, since cloud densities significantly higher than a MOT is typically capable of are required. A common solution is evaporative cooling, where the hottest atoms are driven from the trap. This results in an overall energy decrease if the cloud is given enough time to re-thermalize, which is possible due to the long lifetime. If a coil perpendicular to the Ioffe axis sends in a weak MHz field, atoms resonant with this field can be flipped to another spin state and leave the trap. Due to the shape of the magnetic potential, the Zeeman splitting (2.3) is position-dependent (like in a MOT). As atoms with higher energies reach areas further away from the field minimum than colder atoms, they experience a higher magnetic field and with it larger level spacing. If the frequency of the incident rf signal is higher than the Zeeman shift of the atoms close to the trap center, but already matches the energy difference of some of the hotter atoms, the latter are driven to non-trapped m_F states and fly away. In this manner, a certain part of the high-energy tail of the Maxwell-Boltzmann distribution can be cut off. Therefore, this kind of radiation is commonly referred to as an rf knife. Sweeping the frequency slowly down removes more and more atoms, until only the coldest ones remain in the trap. This means, that the atom number considerably decreases, but the residual cloud gets very, very dense [35]. Pictures proving this claim will be presented in ch. 4.4.3. The required signal is applied via the rf coils shown in fig. 3.20a.

3.4.3 Loading into the chip trap

The chip mounting is located above the QUIC trap position, with the trapping wire(s) offset from the cylinder axis by ~ 5.5 mm in the direction of the Ioffe coil. It is made of quartz to provide very good thermal, but bad electrical conduction. The atomchip is glued onto the surface and contacted via aluminum bonds through niobium pads. Over the past years, different kinds of chips were mounted inside the science chamber. A detailed description of various chip designs can be found in [17]. While some rather

---

[26]Rearranged version of Haslinger 2011 [28], ch. 5.4, fig. 5.6

complicated designs were already tested years ago, the upcoming measurements only require a simple Z-wire (cf. ch. 1.1). The currently used chip is shown in fig. 3.24. The niobium film, from which the wire was structured, was put on a sapphire substrate.

A very short overview of the chip loading sequence shall be given. The transverse magnetic field of the Z-wire trap is rotated by 45° with respect to the according QUIC trap field. Therefore, some "swing-by maneuver" is inevitable, which requires additional bias fields (cf. fig. 3.22). The current sequence is rather complicated and can be found in [47], where the chip loading observed along the Ioffe coil axis is depicted as well. As the cloud movement is most evident from this vantage point, it is advantageous to monitor the loading process on a second imaging axis (see ch. 3.4.4). A detailed insight into the chip trap will be given in the next theses featuring the QuIC experiment [46, 61, 68].

3.4.4 Imaging setup

A vital demand of the coil cage and shield design is optical access. The atom cloud is simultaneously imaged on two perpendicular axes, requiring two cameras illuminated by two imaging beams. The beams are directed to the entrance windows (one of them shown in fig. 3.16) through the respective optical fibers, whose input couplers are labeled in fig. 3.12. One of them enters the chamber through the Ioffe coil (axis x in fig. 3.4) and is mostly used for surveilling the chip loading sequence (cf. ch. 3.4.3). The other one defines the main imaging axis (y) and features two configurations: The light can either be sent directly through the atom cloud, or reflected by the chip, which is utilized for distance measurements in the chip trap. A detailed discussion of absorption imaging of atoms close to surfaces is given in [62]. While the MOT camera is equipped with a proper objective with fixed settings, the two cryostat imaging axes comprise several lenses. This allows for changing the magnification by removing or exchanging one of the lenses and moving the respective camera (fig. 3.25). A detailed description of the main imaging setup can be found in [17]. The Ioffe imaging setup has recently been modified, in order to improve the resolution, which included placing a lens inside the cryogenic environment (cf. fig. 3.19). The characterization and optimization of this new approach is under development and will be presented in [61]. In principle, it should be sufficient to be able to monitor the cloud during the chip loading, since everything else can be acquired with the main imaging system.
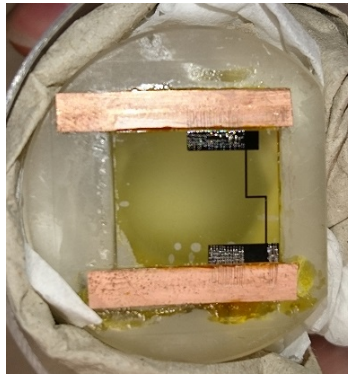

Fig. 3.24: The chip mounting with a Z-wire atomchip on top.
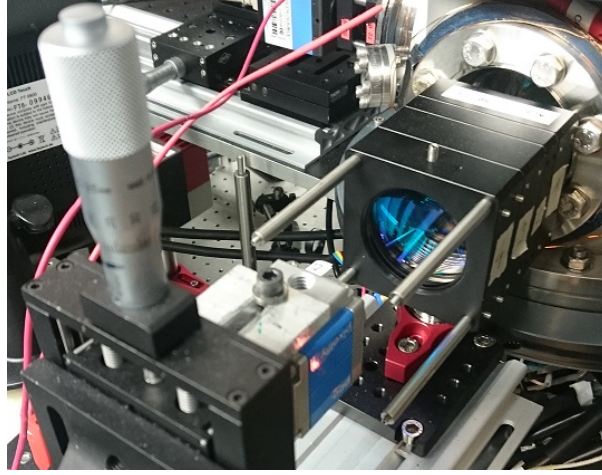
Fig. 3.25: Main imaging axis for the science chamber. The camera ("Pixel Fly") is mounted on translation stages. Switching from low to high magnification requires removing the last lens and shifting the camera backwards. On top of the picture, the Ioffe camera is discernible.

3.5 Quenching setup

The most substantial achievement of the recent past definitely was the implementation of a chip quenching setup. The intended analysis and subsequent utilization of the current and magnetic field hysteresis (cf. ch. 1.3) requires the possibility of resetting the superconducting atomchip to its virgin state. This means, that a technique for erasing the magnetization memory of the chip wire needed to be implemented (cf. ch. 2.5.3). In principle, warming up the entire chamber, until the transition temperature is exceeded, and then turning on the cryostat again would be a feasible method. However, this would lead to a pressure rise inside the science chamber with every turnoff. For this reason, a sudden phase transition rapidly spreading over the specimen constitutes a much better approach. This can be triggered in different ways, in any case at least one of the critical parameters T_C (temperature), H_{C2} (magnetic field) or J_C (current density) needs to be exceeded (cf. ch. 2.5.2). The second option comes with a side effect rendering it impractical, since the necessary magnetic field strengths would induce a remnant magnetization in the chip wire. Any subsequent current distribution would therefore depend on this quench field, i.e., instead of resetting the superconductor to its virgin state, a certain history would already be imprinted. A potential alternative is the combination of a strong laser and a weak chip current, which seemed very suitable for application at QuIC.

3.5.1 Quenching with a laser

The basic idea stems from another experiment investigating superconducting atomchips [48]. There, a blue laser (488 nm) was employed for opening the superconducting loop by locally heating the material. The optical laser powers used were in the range of $\sim$ 0.5-1.5 W. As reported in [64], shining a laser onto a superconducting thin film can furthermore lead to a sudden resistance jump on a distinctly shorter timescale than expected from ordinary heating. It is possible, that the energy deposited in the film is absorbed by the electrons. Thus, they could be excited across the energy gap Δ, implying the breakdown of the superconducting phase.

45

An easy way of monitoring the wire resistance is supplying a current and continuously measuring the voltage. Moreover, in case the laser is only heating the superconductor, a weak chip current can be sufficient to rapidly quench the wire: As the size of the energy gap diminishes with increasing temperature, the critical current density j_C, being proportional to Δ, is reduced by heating (cf. ch. 2.5.2). This approach has more advantages: For one thing, the required chip current is very likely to be well below the minimum transport current applied in any measurements. The hysteresis behavior is determined by only maximum values. For this reason, the quenching process, in particular the current flow right after reverting to the superconducting state, does not effect the experimental cycle. For another thing, the combination with the current can trigger an avalanche effect [9]. This allows for resetting the wire over the entire length of interest. It could be proven, that this method of quenching the chip really works, as will be discussed in ch. 3.5.3.

The laser chosen for the quenching setup is a Mephisto laser[27] and can provide an output of up to $\sim 1\,\mathrm{W}$ in the infrared region with $\lambda = 1064\,\mathrm{nm}$ [13]. This wavelength corresponds to an energy greater than the superconducting energy gap of niobium (cf. ch. 2.5.4). Consequently, enough energy for breaking Cooper pairs might already be deposited by the laser, which happens on a much shorter timescale than heating. A calibration graph acquired by means of a power meter placed almost right after the beam output is given in fig. 3.26. An important feature regarding the integration into the experimental cycle is the possibility to remotely control the injection current. This way, the output power can easily be varied, as the frequency does not matter at all for the designated application. By feeding an analog signal into the *Current Laser Diode* modulation input, the current can be tuned ($0.1\,\mathrm{A/V}$ [13]). This has been tested with a signal generator and a PD connected to an oscilloscope, and revealed a response time of $\sim 180\,\mu\mathrm{s}$. The latter needs to be taken into account for programming the corresponding ADwin channel (cf. ch. 4.5.1). An analog channel can be used for usually keeping the injection current below the lasing threshold (where lasing activity starts) and ramping it up to a sufficiently high value only for quenching.
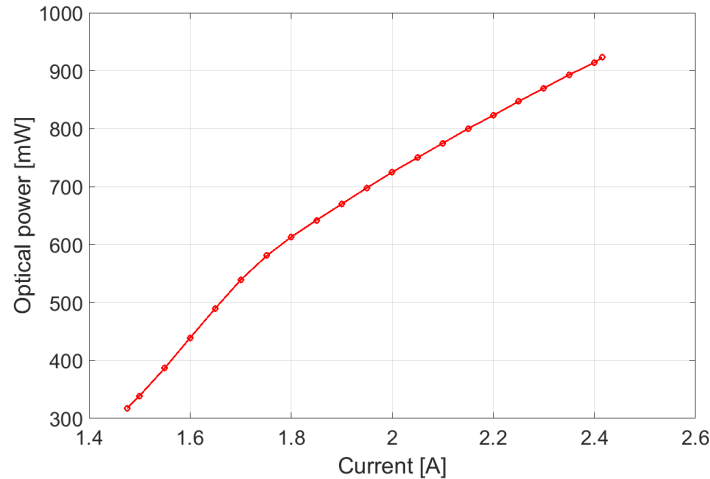

Fig. 3.26: Mephisto output power for different injection currents. This curve was ultimately used for calibrating the analog channel, that controls the laser power.

---

[27]Coherent Inc.

3.5.2 Focusing onto the wire

The atoms approach the science chamber from below, i.e., they are transported vertically along the z axis drawn in fig. 3.4. For this reason, the different shields (cf. ch. 3.4) all have holes along this axis, so that the cloud can pass through. Furthermore, the atomchip wire is visible from below (cf. fig. 3.20b), which is why directing the beam into the cryogenic environment through the bottom window shown in fig. 3.4 is the most convenient solution. This optical access is located below the end of the horizontal transport and was originally installed for potentially providing an additional cloud imaging axis. Aligning the laser beam onto the chip requires an imaging setup. The first version of this setup was planned and built up in the course of a short-term project [29]. The necessary simulations were performed with Zemax[28]. The combination of some mirrors and two lenses allows for attaining a sharp image of the Z-wire on a live camera. The imaging light is shined in through the window opposite to the Ioffe coil, for which a flashlight can be utilized. Meanwhile, the setup has already been modified a few times. Above all, the camera had to be replaced by a worse one, but the result is still sufficient.

Due to the constructional constraints, a single mirror below the entrance window is used for imaging and shining in the laser both. This could be implemented by using a polarizing beam splitter for defining the two different light paths: The laser beam is split into a transmitted part entering the cryogenic environment, and a reflected one hitting a beam dump. The reflected part of the imaging light, that leaves the chamber at the bottom, is directed to the opposite side, where the lenses and the camera are located. The polarization of the laser beam causes the major fraction of the optical power to be reflected into the dump. As a half-wave plate suited for this specific wavelength was not available, the cube was therefore attached to a flip mirror mounting (fig. 3.27). Thus, it is still possible to use the PBS for aligning the laser, where only very low power is required. For quenching, the cube is then simply flipped away, since the beam is only negligibly displaced on the transmission axis. An overview of the entire quenching setup is depicted in fig. 3.28.
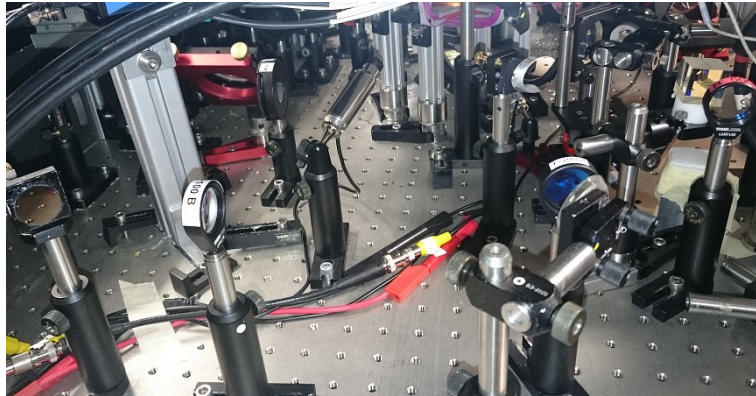
Fig. 3.27: A part of the quenching setup. The laser beam passes trough the lens on the very right and then through the PBS. The imaging light approaches the cube from the opposite side and is reflected to the left. Once the alignment is sufficient, the beam splitter can simply be flipped away.

---

[28]http://www.zemax.com/
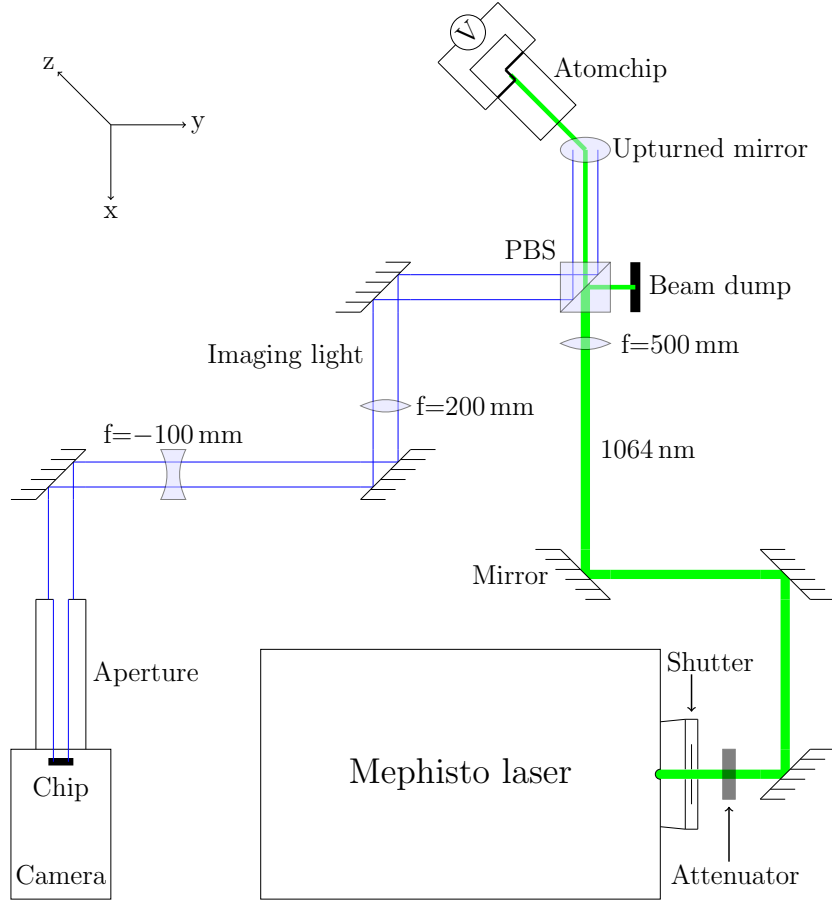
Fig. 3.28: A sketch of the quenching setup in bird's-eye view. The upturned mirror reflects the laser beam into the chamber, where the atomchip is mounted. In this illustration, the beam is aligned to the center of the Z-wire. Monitoring the chip voltage allows for identifying a quench. The attenuator after the shutter is only used for alignment. The axes drawn here are the same as in fig. 3.4.

Aligning the laser beam to the chip wire is not straightforward, since the spatial leeway is rather limited. As a first step, the beam was directed more or less centrally through the chamber, while the cryostat was open: A paper circle matching the diameter of the outer cylinder was placed on top. Then, the beam was centered on the bottom window by moving one of the mirrors far away. After that, the upturned mirror just below the access window was adjusted, such that the laser spot hit the center of the paper circle. This procedure was repeated several times, until the beam seemed to enter and leave the chamber as centrally as possible. This at least guaranteed, that the light would reach the atomchip mounting at all. However, as the chip wire is offset to the geometrical center of the cryostat (cf. ch. 3.4.3), this was only the initial preparation for the alignment.

Steering the beam towards the superconducting wire requires imaging the atomchip on a live camera. In order to achieve this, the chip needs to be illuminated (from opposite to the Ioffe coil) and the imaging light spot on the bottom window must be found. If the aperture mounted on the camera (fig. 3.29) is replaced by a proper objective, the optical elements are discernible as a whole. When the setup was modified for the first time, the mirrors and lenses were already more or less oriented along the imaging beam
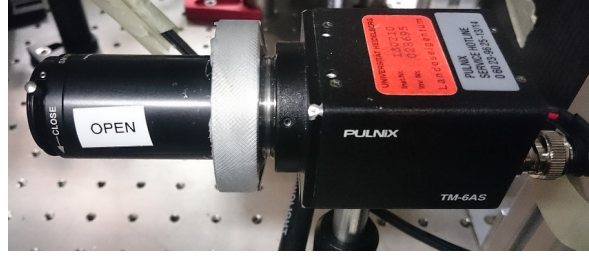
Fig. 3.29: The camera used for imaging the Z-wire. If necessary for alignment, the aperture can be removed and replaced by an objective.

path. For this reason, moving around the camera allowed for receiving a bright light spot on the closest mirror rather quickly. If the correct position seems to be lost, referring to [29] might help. Once the light definitely reaches the camera chip, the objective can be swapped for the aperture again. Moving the mirrors, the Z-shaped wire should then be locatable (fig. 3.30a). The glue traces looking like conifer branches, which are located below the wire, might serve for orientation. Another prominent features are the contact pads on both sides of the Z (cf. fig. 3.24). Note that the upturned mirror should not be used for adjusting the picture, since it is located after the PBS and changes the laser beam direction as well.

The biggest challenge is steering the Mephisto beam towards the wire. Many obstacles impede the alignment and suppose a lot of patience. In fact, it is very likely that a lot of optical power is lost along the path. As the atomchip surface exhibits a high reflectivity, for alignment the injection current is set to only slightly above the threshold. Additionally, an attenuator, more precisely a neutral density filter reducing the power by a factor $\sim 10^{2.5}$, is inserted after the beam outlet. The resulting laser spot can be slowly moved towards the wire by walking the beam[29]. In case it is too far off, it might be necessary to adjust the upturned mirror below the window as well. This can only be done in small steps, since the imaging axis always needs to be adapted to the changes. Following this procedure, it was possible to center the Mephisto beam on the Z-wire (fig. 3.30b).

(a)   (b)
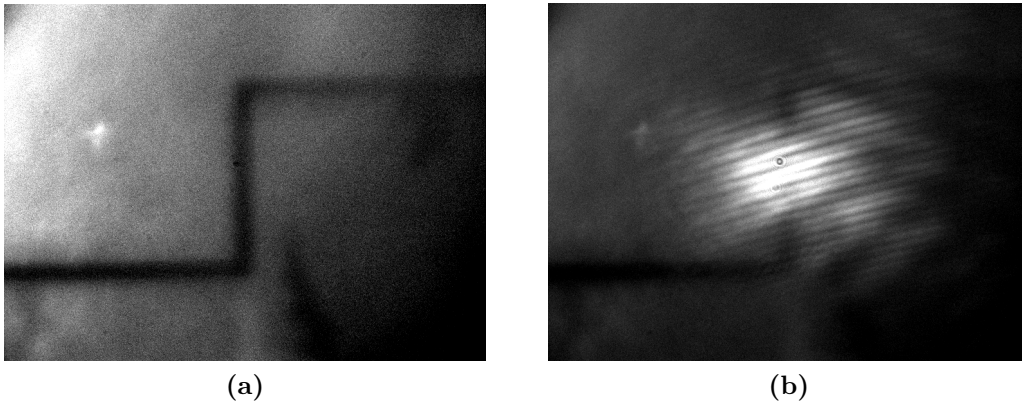
Fig. 3.30: Live image of the Z-wire without **(a)** and with the laser beam **(b)**.

---

[29]see for example `http://virtualetters.blogspot.co.at/2012/07/walking-beam.html`

It is worth considering to move the spot somewhere else. This premises an avalanche effect, which would spread the normal conducting phase over the entire wire. It would allow for quenching the atomchip in the presence of a cold atom cloud, without potentially hitting the atoms (see ch. 4.5.2). A convenient alternative to the Z-wire center are the contact pads. Tests on this approach are currently already performed and have been proven successful so far.

3.5.3 Observing a quench

If the laser hits the superconductor and the chamber is cooled down to $\sim$ 4-6 K, the quenching performance can easily be tested at any time. The shutter in front of the beam outlet must be closed, the attenuator removed, and the PBS flipped away. Then, the injection current is manually ramped up to a reasonable value (for the calibration see fig. 3.26). The second prerequisite is a chip current, which can be applied by means of an external current source. In view of the history measurements, it makes sense to keep this current low (cf. ch. 3.5.1), so that the parameters can be adopted to the experimental cycle. Conveniently, the current feedthrough shown in fig. 3.14 can be directly connected to a board with inputs for all the coils and the chip, which is shown in fig. F.2.

For simple tests, its connectors P and Q can be used for supplying the Z-wire. The voltage can be acquired by connecting an oscilloscope in parallel. When the shutter is opened briefly and the atomchip wire quenches, the voltage features a sudden rise, caused by the jump in resistance (according to Ohm's law). The sync signal of the shutter can serve as an external trigger. Utilizing such a setup, the first successful quenches were observed and characterized. The shutter was manually opened and closed again, once the voltage rise was discernible on the oscilloscope. The slope was fitted with a high-order polynomial, and the point in time, where the voltage had reached its high level (considering some confidence interval), was determined (fig. 3.31). The time difference between this point and the trigger defines a quench delay. With a constant quench current $I_q \approx 100\,\mathrm{mA}$, voltage curves for different laser powers were recorded. The delay's dependence on laser power is plotted in fig. 3.32.
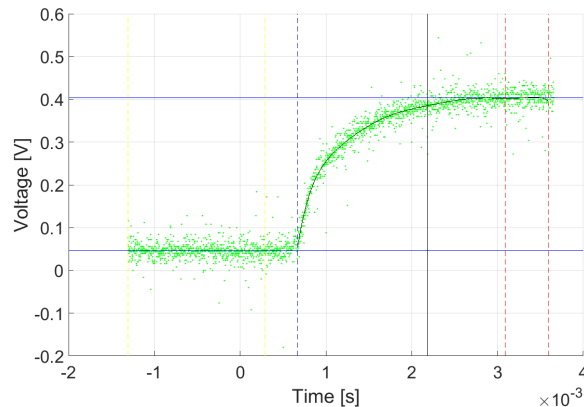
Fig. 3.31: A quench acquired by an oscilloscope. $t = 0$ marks the shutter opening, less than a ms later the resistance starts to increase. The laser power in this example was $\sim 870\,\mathrm{mW}$, $I_q \approx 100\,\mathrm{mA}$. By means of a data fit, a quench delay was determined, marked by the vertical solid line. There, the fit reaches 95% of the upper voltage level.

50
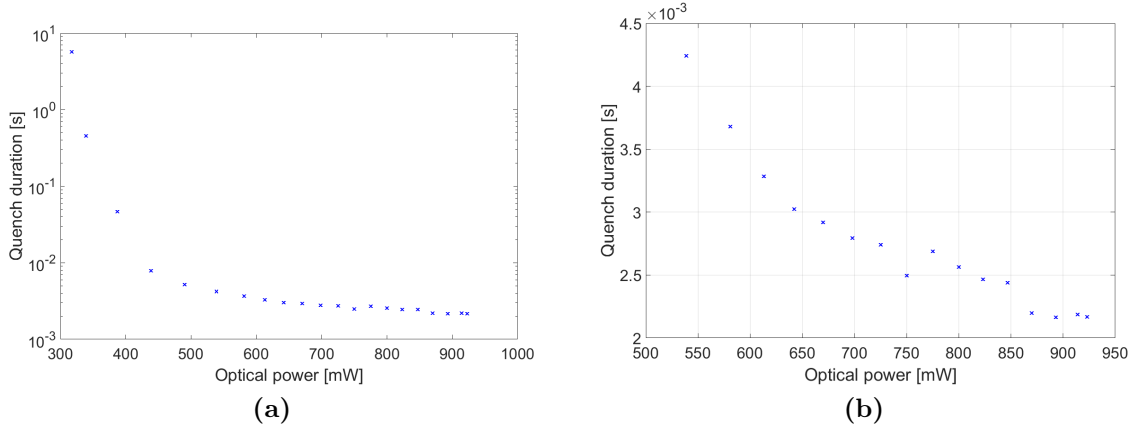
Fig. 3.32: Quench delay for different laser powers and $I_q \approx 100\,\mathrm{mA}$. These curves were produced from fits like in fig. 3.31. **(b)** is just a section of **(a)**.

Incorporating the quenching into the experimental cycle requires applying the chip current via the corresponding analog channel and monitoring the quench in one of the PC programs. In order to test this, an external power supply was used for simulating an ADwin channel, i.e., the current was really run through all components between the ADwin box (cf. fig. 3.5) and the atomchip. The chip was furthermore connected to the DAQ (**d**ata **acq**usition) card, that is used for monitoring the superconducting coils. A separate window for the chip voltage and the shutter was added to the related program (cf. ch. 4.1.3).

After having to realign the quenching laser, the subsequent tests showed a considerably better performance than observed before. Already a quench current $I_q \approx 5\,\mathrm{mA}$ forced a fast transition to the normal conducting state with laser powers $P_q < 400\,\mathrm{mW}$. This current strength is definitely much weaker than any transport current I_t intended to be applied during measurements in the chip trap. For this reason, it was decided to stick with this value and search for a proper combination of laser power and quench delay. It was figured out, that already a few milliseconds of exposure at optical power below $500\,\mathrm{mW}$ initiated a quench. An example quench acquired with the DAQ card is shown in fig. 3.33 (however using $P_q > 500\,\mathrm{mW}$). While the voltage resolution is much better than in an oscilloscope, the time resolution is not really good, and it was not possible to properly fit the slope. Therefore, trying to create a neat plot of quench delay over laser power was not successful.

The only vital condition for the current and magnetic field history measurements is the possibility of resetting the atomchip to its virgin state. This is sufficiently fulfilled by the new quenching setup.
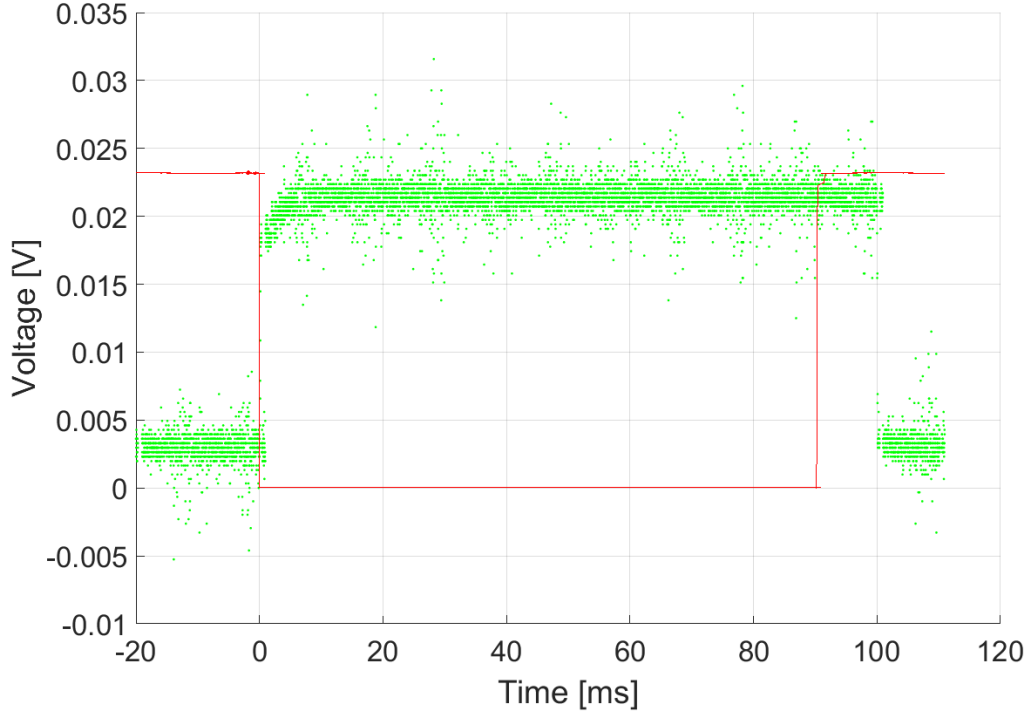
Fig. 3.33: A quench acquired by measuring the chip voltage via a DAQ card. The red graph is the shutter sync signal, the green one the chip voltage. After a few ms, the voltage suddenly increases, indicating the breakdown of the superconducting phase. An interesting feature is the fact, that the voltage stays at the same level, while the shutter is open. Furthermore, it drops soon after closing. This might imply, that just enough energy for breaking the Cooper pairs is supplied, but no further heating occurs. This graph was acquired with $I_q \approx 5\,\mathrm{mA}$ and $P_q \approx 870\,\mathrm{mW}$. Supplying the same current, it is actually possible to quench the wire with $P_q < 400\,\mathrm{mW}$, depending on the alignment accuracy.

4 Operation and performance

This chapter is intended to serve as an introduction to the different experimental cycles. It provides a guideline for characterizing the atom cloud properties and features the necessary devices and programs. Furthermore, the recent standard performance of the experiment is presented. This might help to perceive and pin down potential errors. How to confront different kind of issues is elaborated in ch. 5 and appx. A. Beginning with August 2016, benchmark measurements were performed at regular intervals and noted down to the lab book.

4.1 Basic start-up

The daily start-up procedure needed for any measurements on the atom cloud shall be explained briefly. In order to obtain a Rb vapor background in the MOT chamber, the dispensers must be switched on (cf. ch. 3.1). This constitutes the start of a standard workday, since some waiting time is required, before recording any data makes sense. The two associated current sources are depicted in fig. 4.1. After turning those on, the LabView[30] VI (**v**irtual **i**nstrument) *Agilent 6623A Power Supply.VI* is started and the third output set to 6.1 V (fig. 4.2). The optimal value might gradually change and depends on the amount of Rb left in the dispensers. As suggested before, achieving a reasonable MOT cloud requires some waiting time after the dispenser start-up. Depending on how long the experiment was in operation beforehand, it can take $\sim$ 2-6 hours. For this

Fig. 4.1: The two current sources controlling the dispensers. Device **(a)** controls the output voltage of **(b)** via a Sub-D connector. The dispensers are finally supplied via two banana cables, discernible at the very right.
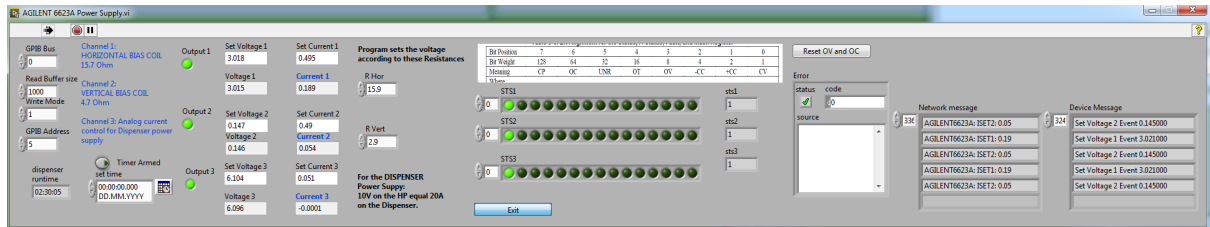
Fig. 4.2: Front panel of the Agilent VI, where the dispenser control voltage is set (*Output 3*). Boolean indicators show, whether the outputs are on or off. The first two outputs supply two of the three MOT chamber bias coils and are controlled via ADwin.

---

[30]http://www.ni.com/labview/

reason, a timer has been added to the program, automatically switching the output on at a selectable time.

4.1.1 Lab devices

Nearly everything inside the cryogenic part is supplied by car batteries (fig. 4.3). These are usually charged over the weekend. The normal conducting part is supplied by the Deltas (cf. ch. 3.1), one of them being shown in fig. 4.4. For safety reasons, they are always turned off before leaving. To prevent accidental water leaks in the water cooling, the same holds for the corresponding valve (fig. 4.5). Opening it before running any measurements is even more vital. Otherwise, the coils heat up rather quickly. That they burn is unlikely, since all normal conducting coils are equipped with bimetal temperature sensors. Via a relay box (fig. 4.6), these immediately disconnect the heavy current supply,
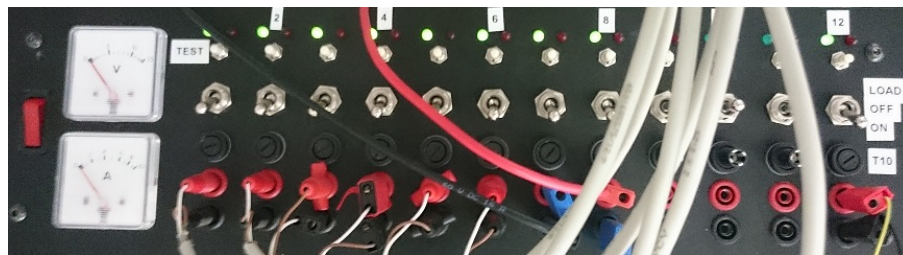
(a)

(b)

Fig. 4.3: The car battery current sources. All connected outputs should be activated when running the experiment. The switch position assignment of **(b)** is exactly opposite to the labeled one of **(a)**.
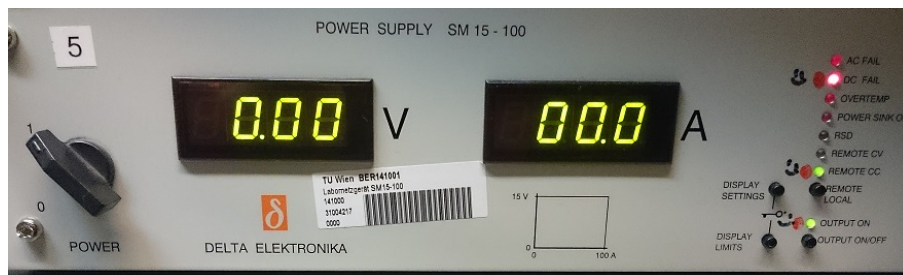
Fig. 4.4: One of the Delta current sources. After turning on the power switch, the bottom right button (*Output on/off*) must be pressed. Upon this, three LEDs should go on, as shown in this picture. This indicates, that the Delta is ready for operation. Starting the other four Deltas only requires using the power switch.

Fig. 4.5: The water cooling valve. This picture is actually flipped by 90°, the valve is located on the left side right after the lab door. It can be distinguished from the other valves by the flow indicator below it. The latter is discernible on the right and should show $\sim$ 8.5-9.5 l. In order to prevent leaks due to too strong water flow, the valve should be first opened very carefully and then slowly adjusted to the desired value.
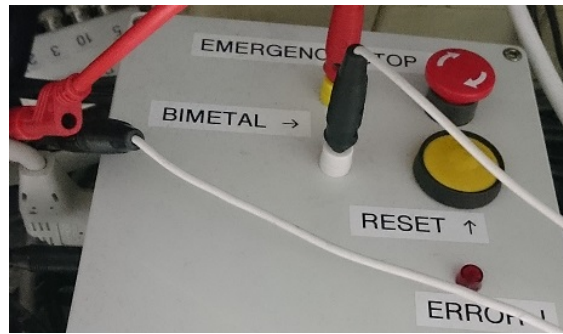
Fig. 4.6: The safety box for the deltas. In case one of the coils heats up above $\sim 80°$C, a relay cuts the connection of the Deltas to the heavy current line. The *emergency stop* button can be used to manually disconnect them. Upon pressing *reset*, the connection is re-established.

when the temperature of a coil exceeds 80°C. The connection can also be cut by means of a manual switch in the control room.

An extensive description of the transition selection and the laser stabilization techniques has already been given in ch. 3.3.1. The chosen slopes can be inferred from figs. 3.7, 3.8 and 3.9. In all three figures, the trigger signal is centered on the oscilloscope screen. This implies, that shifting one of the lasers to a certain frequency is equivalent to moving the desired locking point to the middle of the screen. In scan mode, either the piezo voltage or the injection current is continuously varied within a defined range. Adjusting this range therefore allows for zooming in and out on the spectroscopy and simultaneously the error signal. Additionally, the signals can be shifted by means of a current offset knob. Once the correct slope is centered and zoomed in to as close as possible, the scan mode is deactivated and integration mode turned on. Upon this, the laser is locked to the chosen transition and the PID controller tries to compensate for any deviations. To prevent damage on the laser diodes, unlocking the lasers before leaving is advisable.

If the cryostat is at operation temperature and the pressure is below $\sim 2 \times 10^{-9}$ mbar, the transport valve can be opened (cf. fig. 3.3). This allows for performing measurements on the magnetic transport performance and in the science chamber. The function generators providing the rf signals for cooling in the QUIC trap (cf. ch. 3.4.2) are called "SRS" (**S**tanford **R**esearch **S**ystems) and "Agilent RF 2".

4.1.2 Experiment control

The heart of the experimental control is the user interface accessing ADwin. The different GUIs available (cf. ch. 3.2) demand for different boolean settings. These are needed for switching between the different sections of the Matlab code, that are executed during the cycle. The corresponding values will be denoted in the subsequent interface descriptions. Since different cameras are used for imaging in the MOT respectively the science chamber (cf. chs. 3.3.2 resp. 3.4.4), the camera control program(s) must be selected depending on the chosen GUI. The image processing program, however, is always the same, and the correct camera can be selected in the *Acquisition* window. The acquired pictures and the calculated cloud image are displayed in this window. It is possible to select an ROI (**r**egion **o**f **i**nterest) and an RBC (**r**egion of **ba**ckground). The selected section is shown in the *RealTimeProcessing* window, some characteristic properties are calculated and denoted in the *Data Window*. The trend of one of these attributes can be monitored in the *Online Plot*. How to start the program and to load and run the interfaces is explained in detail in appx. B.1.

4.1.3 Monitoring programs

The pressure in the science chamber is recorded by *Varian Pressure new.VI*, the temperature by *Lakeshore 336 new.VI*. The acquired data is automatically saved to log files. The alarm program mentioned in ch. 3.4.1 is called *Temperature Alert.VI* and outputs an alert, whenever the temperature or the pressure exceeds the defined limits. In addition, any issues in the communication between ADwin and one of the camera control programs are reported too. The currents running through the normal conducting part are traced in *Delta DAQ Complete.VI*, the superconducting one in *Cryo DAQ Complete.VI*. The latter furthermore contains a separate field comprising the chip voltage and the shutter for the quenching laser (cf. ch. 3.5.3). The MOT live cam (shown in fig. 3.2) is accessed by *wxPropView*. Since the MOT constitutes the very first part of every experimental cycle, it indicates if enough atoms are acquired from the rubidium background. An example screenshot of a reasonably big MOT cloud in the chamber is given in fig. 4.7.
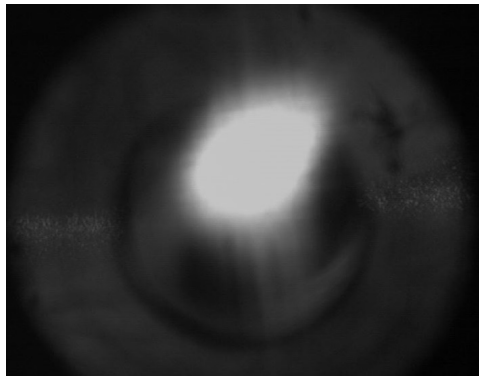
Fig. 4.7: The MOT cloud in live mode. Ideally, the observed cloud is rather big and more or less symmetric. In case the beam alignment (or maybe only the bias field settings) is not sufficient, it seems like the atoms are leaking out to one side of the trap.

4.1.4 Data evaluation

A data evaluation program named *NEW_analyze_Vxx.m* (where *xx* stands for the sometimes changing version number) allows for analyzing any variable scan by entering date and scan number. Most of the parameters there are self-explanatory. Specific graphs like lifetime or cloud temperature fits are automatically provided, when the associated variable was scanned.

4.2 Magnetic trap: M-GUI

This user interface was designed for characterizing and optimizing the laser cooling and the subsequent magnetic trapping. The atom cloud can be imaged right after the molasses, or after a variable holding time in the magnetic trap. In the latter, the atoms are simply confined by means of the MOT coils, without laser light being present.

4.2.1 Specific programs and settings

The camera control program for the MOT camera is written in Visual Basic. In *Example1.vb* (*Microsoft Visual Studio*), the file path somewhere in the upper part of the document is adapted to the current date. After running the program, the device is chosen and its properties are checked: Any auto settings are deactivated, the gain is set to minimum level and the exposure time to 1/2000 s. Gamma should be around 100 and the trigger needs to be enabled. The button next to the input field is used for establishing the connection to the device. Then, the image processing program can be started (see appx. B.1). In the *Acquistion* tab, the *Firefly* camera is selected. The only boolean that matters is **adwin.magnetic_data.magnetic_transport = 0** found in *start.m*.

4.2.2 Vital parameters

How to initialize the ADwin interface and run the experimental cycle is described in appx. B.1. How to perform measurements on the parameters determining the cloud properties is explained in appx. B.2.1. The highest impact on these properties is definitely given by the detuning settings. This is easily discernible, since the observed atom number distinctly changes with the detunings. A certain range, in which reasonable values are expected to be found, is already given by fig. 3.10. However, besides the influence of magnetic fields, possibly unknown and even changing distortion factors can considerably shift the required frequencies. For this reason, it is advisable to perform detuning scans from time to time. As long as the introduced benchmarks are really reproducible, this is probably not necessary. But if the atom number or the cloud shape changes, such a scan might already give a better insight into the problem. The most recent surprise was a shift of the optimal MOT detuning (**MOT_det**) from -20 to **-29** MHz. This happened for no obvious reason at all, so it was decided to stick to the new value. Before that, the pump detuning (**Pump_det**) had changed by tens of MHz (cf. ch. 3.3.1). This problem could be solved in the end, as elaborated in ch. 5.3. The molasses detuning (**Mol_det**) mostly influences the cloud temperature, but within quite a large range around the expected value, the difference does not seem that big.

All the bias field settings contain **comp** in their names. They are also very important for the atom lifetime and temperature, but usually stay the same, unless the beam alignment changes. The best possible values depend on the alignment and the position of the MOT coils. How to properly adjust them will be described in ch. 5.2. Only **B_comp_quant** does not depend on all of this. It is utilized for generating a short pulse before the magnetic trap, in order to define a quantization axis for optical pumping (cf. ch. 2.1).

The parameters frequently scanned are used for characterizing the atom cloud and therefore the performance of the experiment. The **average atom number** in the **magnetic trap** is by default determined for a holding time **t_after_magnetic** of **1370** ms and a **TOF** (cf. ch. 3.3.2) of **10** ms. The dummy variable **Scan** is scanned, which means repeating the exact same measurement multiple times. Upon scanning the holding time **t_after_magnetic**, the **lifetime** in the trap is measured. The evaluation program automatically applies an exponential fit to the atom number decrease depending on the duration of the trapping phase (cf. ch. 4.1.4). Varying the **TOF** provides an estimation for the expansion speed of the atoms after being released from the trap. This allows for calculating the cloud **temperature**, which is done by the evaluation program too. Basically the same measurements can be performed in the **molasses** phase. This requires setting the MOT currents **I_MOT_trap1** and **I_MOT_trap2** to **0**. Furthermore, **IMAGE_TOF_notrans** is changed to **0** and **IMAGE_mol_notrans** to **1**. Note that in this case the pump detuning and any magnetic trap settings do not influence the results.

4.2.3 Expected performance

The recently achieved cloud properties in the magnetic trap exhibit the highest atom numbers in the QuIC lab. The main reason for this success probably is the engagement in the MOT alignment, which can be followed in ch. 5.2. As mentioned in ch. 4.1, the actual performance depends on the dispenser run time. After some days of operation in a row and a couple of hours waiting time before performing measurements, a certain plateau seems to be reached. A few example benchmark results are put together in tab. 4.1. What a typical molasses respectively magnetic trap cloud looks like, is depicted in fig. 4.8.

4.3 Transport with return: R-GUI

In case the magnetic trap provides a reasonably big and cold atom cloud, the transport can be optimized. This is done by means of the return GUI. Using this interface, the

Date	2016/12/14	2017/01/10	2017/01/17	2017/01/19
Atom number $[\times 10^9]$	0.9	0.7	1.1	3.4
Lifetime [s]	3.87	3.18	3.16	2.55
T transversal [μK]	553	542	566	590
T longitudinal [μK]	503	488	514	519

Tab. 4.1: Typical properties in the magnetic trap. The standard settings (if the respective variable is not the one being scanned) are t_after_magnetic = 1370 and TOF = 10.

psd	0.07		
temp_trans	22089.05		
temp_long	569.44		
rms_long	3151.62		
rms_trans	1963.25		
best100_pixels	458.14	total_long_pos	320.07
atomnumber	8.42e+008	total_trans_pos	254.81
tof	5.00	thermal_peak_densit	1.31

(a)

psd	0.03		
temp_trans	68356.16		
temp_long	929.82		
rms_long	4027.24		
rms_trans	3453.62		
best100_pixels	388.12	total_long_pos	301.42
atomnumber	1.43e+009	total_trans_pos	279.46
tof	10.00	thermal_peak_densit	0.72

(b)

Fig. 4.8: Typical M-GUI clouds. In this interface, the imaging takes places either after the molasses phase **(a)**, or after the magnetic trapping **(b)**.

atoms are transferred to a certain position within the transport line, held there for a short time interval, and then brought back into the MOT chamber. The first few centimeters of the transport work with the transport valve closed too, but for the rest it needs to be opened before. For this reason, the cryogenic environment must be properly evacuated before and cooled down to the cryostat's operation temperature (cf. ch. 4.1.1). The cloud can be transported all the way up into the science chamber and back. The maximum distances are 210.4 mm along the horizontal and, subsequently, 215 mm along the vertical direction. The coil setup needs to be supplied with the correct current sequence, which can be checked in the two DAQ card VIs (cf. ch. 4.1.3). What the curves should look like and how to handle potential deviations will be explained briefly in appx. A.1.

4.3.1   Specific programs and settings

Since the atoms are always transported back into the MOT chamber, the image is taken there as well. This means, that the same camera as for the M-GUI is used, so for start-up refer to ch. 4.2.1. The boolean variables need to be adapted to tab. 4.2.

4.3.2   Vital parameters

In case any characteristic M-GUI parameters had to be adjusted for improving the cooling and trapping, those now need to be transferred to the R-GUI. The position mostly

Boolean variable	Value
adwin.magnetic_data.oneway	**0**
adwin.magnetic_data.calculate_always	**1**
adwin.magnetic_data.vertical_transport	**0**
adwin.magnetic_data.magnetic_transport	**1**

Tab. 4.2: Boolean settings for the return GUI. The last one is found in *start.m*, the others are located in *magnetic_transport_parameters.m*.

used for any optimization scans is the **corner**, i.e., the end of the horizontal transport. Consequently, the horizontal coordinate **xfinal_gui** is set to **210.4** mm. The boolean switching between exclusive horizontal and additional vertical transport, **vert_on_gui**, must be **0**. The default holding time at the selected destination, **t_hold_hor_gui**, equals **20** ms, the standard **TOF** is **5** ms. This change compared to the M-GUI (cf. ch. 4.2.2) stems from timing issues adding an offset of 6.5 ms. The latter can be taken into account in the evaluation program. Actually, there are parameters already present in the M-GUI, whose impact can only be realized by optimizing the corner cloud. Minor differences in certain attributes of the magnetic trap cloud can have a significant influence on the transport performance. The best example is the Repump AOM level during the pumping phase, **R_level_pump**. It defines the amplitude of the voltage signal, which supplies the corresponding AOM transducer (cf. ch. 3.3.1). While varying this level makes hardly any difference for the magnetic trap, it significantly changes the atom number in the corner.

The transport interface is separated into variables for the horizontal part of the transport and such for the vertical one. As long as **vert_on_gui** equals **0**, only the horizontal coordinate and the corresponding holding time are considered. Scanning **xfinal_gui** serves as an estimation for the **horizontal transport** quality. The dependence of the atom number on the holding position indicates, where most atoms are lost. The benchmark measurements in the **corner** record the **lifetime** by scanning **t_hold_hor_gui**, and **temperature** by varying the **TOF**. When **vert_on_gui** is set to **1**, the **vertical transport** performance can be acquired by scanning **zfinal_gui**. For this measurement, the horizontal settings are kept at their default values and **t_hold_vert_gui** is set to **20** ms too.

If the magnetic trap yields the expected results (cf. ch. 4.2.3), but the atoms seem to get lost on their way to the corner, the angle of the coil rail might be misaligned. Three translation stages with long posts are supposed to more or less fix the horizontal transport coils in place, but the latter are still rather easily movable. Therefore, it might be necessary to play around with the position, until a sufficiently big atom cloud in the corner is achieved. The post on the side of the laser setup can be used as a reference for optimizing the angle.

4.3.3 Expected performance

The horizontal transport scan exhibits a very typical shape, which is not so clear for the vertical one (fig. 4.9). A benchmark compilation is given in tab. 4.3, a reasonably big corner cloud is depicted in fig. 4.10.
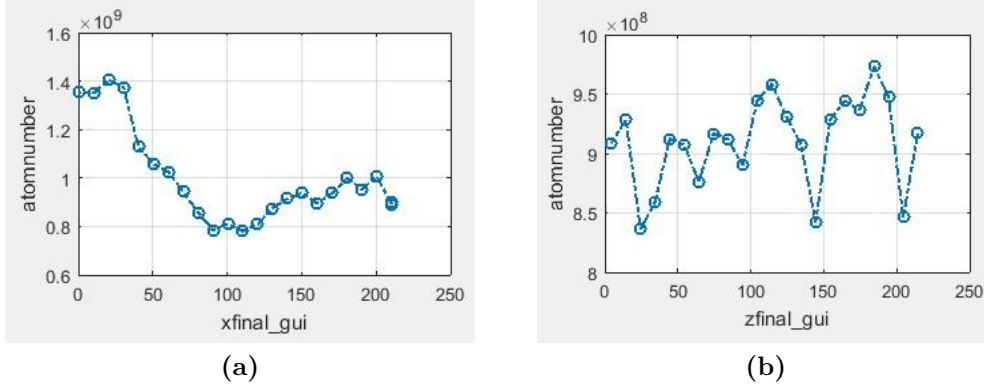
Fig. 4.9: Transport performance. The curves show the atom loss along the horizontal **(a)** respectively the vertical **(b)** axis. If the observed performance is similar to these figures, the coil rail angle is probably more or less fine. The horizontal transport performance is much more reproducible than the vertical one.

Date	2016/12/14	2017/01/10	2017/01/17	2017/01/19
Atom number $[\times 10^8]$	7.1	4.7	8.4	9.1
Lifetime [s]	4.12	2.47	5.46	5.63
T transversal $[\mu K]$	293	575	696	631
T longitudinal $[\mu K]$	1067	1772	2334	1527

Tab. 4.3: Typical properties of the corner cloud. The standard settings are t_hold_hor_gui = 20 and TOF = 5, the appropriate position variable is xfinal_gui = 210.4, while vert_on_gui = 0.
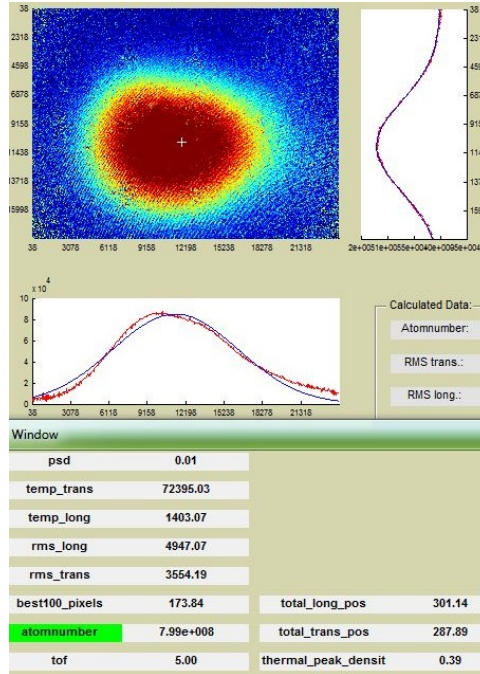
Fig. 4.10: Typical R-GUI corner cloud. The image is taken after transferring the atoms into the corner, briefly holding them there, and bringing them back into the MOT chamber.

4.4 Inside the cryogenic environment: C-GUI

This interface is used for optimizing the QUIC trap and the rf cooling. Furthermore, measurements in the chip trap can be performed, which is not featured in this thesis. The latest extension of the experimental setup, the possibility of quenching the chip wire (cf. ch. 3.5), is not considered in this section either. The chosen approach to incorporate it into the C-GUI will be discussed in ch. 4.5. Here, the focus is on optimizing the parameters required to obtain a sufficiently dense atom cloud, which is ready for loading onto the atomchip.

4.4.1 Specific programs and settings

For measurements in the science chamber, two cameras are available. They require separate control and image processing programs. For the main imaging, a Matlab program (called *start.m* and containing "Pixelfly" in its comment section) is used. This imaging axis features two different options, high or low magnification, determined by the established imaging setup (cf. ch. 3.4.4). Therefore, the camera selection menu in the *Acquisition* window (cf. ch. 4.1.2) contains *Pixel Fly* with the adjunct *1 HIGH async mode* or *2 LOW async mode*. Controlling the Ioffe camera works with *IC VB Dialog Application1* (*Microsoft Visual Studio*). The program is very similar to the MOT camera control, which is why the further course of action can be inferred from ch. 4.2.1. The camera to be selected in the image processing program is named *FireFly 3 Cryo*.

Rf cooling utilizes *SRS DS345.VI* and *Agilent RF 2.VI*, which control the function generators. Since the communication with ADwin is not really fast, changing variable values sometimes suppresses the signal output for one or two cycles. Boolean indicators on the front panels (*SWEEP busy* respectively *Modulation Enable*) indicate, whether the rf signal is supplied or not. The necessary boolean settings for the C-GUI are given in tab. 4.4.

4.4.2 Vital parameters

Any variable changes in the other GUIs have to be adopted to the C-GUI. In contrast to the other interfaces, in this one the type of cloud being pictured is entirely determined by the TOF setting. This implies, that it is not possible to run only a part of the cycle. The whole sequence is always executed, and only the moment the first picture is taken can be changed. For a single phase within the cycle, time-of-flight measurements can be performed, which is the chip trap: TOF = 0 marks the turnoff of this trap, so a scan of TOF > 0 shows no influence of magnetic fields any more. For any other kind of trap active after the end of transport, this does not work.

Boolean variable	Value
adwin.magnetic_data.oneway	**1**
adwin.magnetic_data.calculate_always	**0**
adwin.magnetic_data.vertical_transport	**1**
adwin.magnetic_data.magnetic_transport	**1**

Tab. 4.4: Boolean settings for the C-GUI.

For the subsequently explained measurements, it is advisable to choose low magnification on the main imaging axis, as the non-cooled cloud is usually too big for the high one. The first phase after the transport is the **buffer trap**, usually optimized by already looking at the **QUIC trap**. This corresponds to a **TOF** of **-1430** ms and marks the moment before the chip loading process begins. The associated variable is **I_Buffer** and changing it will have a noticeable impact on the QUIC. For this optimization, rf cooling should still be deactivated, in order to clearly observe any difference. This is guaranteed by setting **SRS_rf_amp** to **0** and **Agilent_rf_output** to **0**. The crucial parameters of the QUIC trap are **I_Series** and **ioffe_ratio**. The latter defines the ratio between the QUIC series and the Ioffe coil current (cf. ch. 3.4.2). When an atomchip is mounted in the science chamber, the bias field **BVHH_away** is expected to make a difference as well. It shifts the cloud closer to or further away from the chip surface. An **average atom number** in the **QUIC trap** can be estimated by scanning the **scan** variable. Furthermore, the **lifetime** can be determined by varying **t_after_rf**.

The QUIC phase has recently been split up into four different parts. It begins with a holding time **SRS_rf_Ctime**, where a constant rf signal provided by the SRS device is supplied. The next step is an rf ramp, where the SRS output is ramped down from **SRS_rf_start** (in MHz) to **SRS_rf_end** within a time interval given by **SRS_rf_Rtime**. Subsequently, a second signal ramp can be added, that is supplied by the Agilent device and analogously determined by the variables **Agilent_rf_start**, **Agilent_rf_end** and **Agilent_rf_time**. Finally, the atoms are kept in the trap without any rf signal being present, the holding time being defined by **t_after_rf**. The two signals are fed into the cryogenic environment via the same cable. A digitally triggered switch connects or disconnects the respective device. The amplitudes are set via **SRS_rf_amplitude** and **Agilent_rf_amplitude**; the Agilent signal generator additionally requires a separate output boolean, **Agilent_rf_output**. In this manner, a two-stage cooling setup was implemented. This allows for splitting the originally used single rf ramp into two ramps with different speeds. This method is believed to improve the cooling efficiency and might pave the way towards a BEC, as outlined in [57]. The cited paper is also intended to serve as a guideline for improving the rf cooling. Optimizing the cooling phase is done by maximizing the peak density instead of the atom number. Once the obtained values look promising, it is necessary to switch to high magnification, where the atom cloud density can be more accurately determined.

On 2016/06/12, a modified C-GUI version was saved. It was designed for measuring the **trapping frequencies** of the QUIC trap, requiring some new variables. These can still be found in *calculate_variables.m* (appx. B.2.2), but are commented out by default, since not being present in any other C-GUI version. The additional feature is the possibility of applying a short **spike** to either the **Ioffe coil current** or the **BVHH_away** field. Upon this, the atom cloud is briefly deflected from its position and therefore starts to oscillate. Scanning the holding time after the spike and plotting the cloud center position over it provides an estimation for the associated frequency. A spike on the Ioffe coil causes a horizontal oscillation, while a bias field spike results in a vertical one.

The **atomchip phase** is covered by **-1430 < TOF < 0** and composed of a sequence of different subphases as well. An instruction for measurements in the chip trap is not presented here, but will be part of the theses to follow [61, 68].

4.4.3 Expected performance

The rf cooling has not been optimized during the course of this thesis. For this reason, it is not possible to show the best cloud to be expected in the QUIC trap at this point. In particular, the two-stage cooling still has to be tested. However, it could be proven, that an rf signal can be utilized for evaporatively cooling the atom cloud in the science chamber. Comparing a cloud exposed to only a short sweep not going too far down to one having experienced a long ramp close to the trap bottom reveals a major difference (fig. 4.11). The expected **lifetime** in the QUIC trap is in the range of **100 - 200 s**. The longest observed lifetimes were even around 500 s (around 2014). It seems like the lifetime might be reduced by the presence of an atomchip, which is why increasing **BVHH_away** can improve the performance.

Finding reasonable starting values for optimizing the cooling phase requires analyzing the trap shape. A so-called trap bottom spectroscopy can be performed by supplying a constant rf knife for a few seconds (e.g. SRS_rf_Ctime = 5000 ms). If SRS_rf_start is changed after each cycle, the number of atoms being addressed by a certain frequency is obtained. The resulting plot can be used as a reference for choosing the ramp interval (fig. 4.12).

By means of a specific C-GUI (cf. ch. 4.4.2), horizontal and vertical oscillations of the atom cloud in the QUIC trap were recorded (fig. 4.13). The obtained variation in position was fitted with a damped oscillation. The resulting frequencies were calculated to $\sim$ **16.66 MHz** along the **horizontal** (longitudinal) and $\sim$ **166.66 MHz** along the **vertical** (transversal) axis. The trapping frequencies and the atom cloud widths along these axes can be used for estimating the cloud temperature. The dense cloud resulting from an optimized single rf ramp is shown in fig. 4.14a. Its width is obtained by a Gaussian fit and provided by the evaluation program. Scanning the holding time after the sweep (t_after_rf) yields the heating rate in the QUIC trap (fig. 4.14b).

(a) (b)
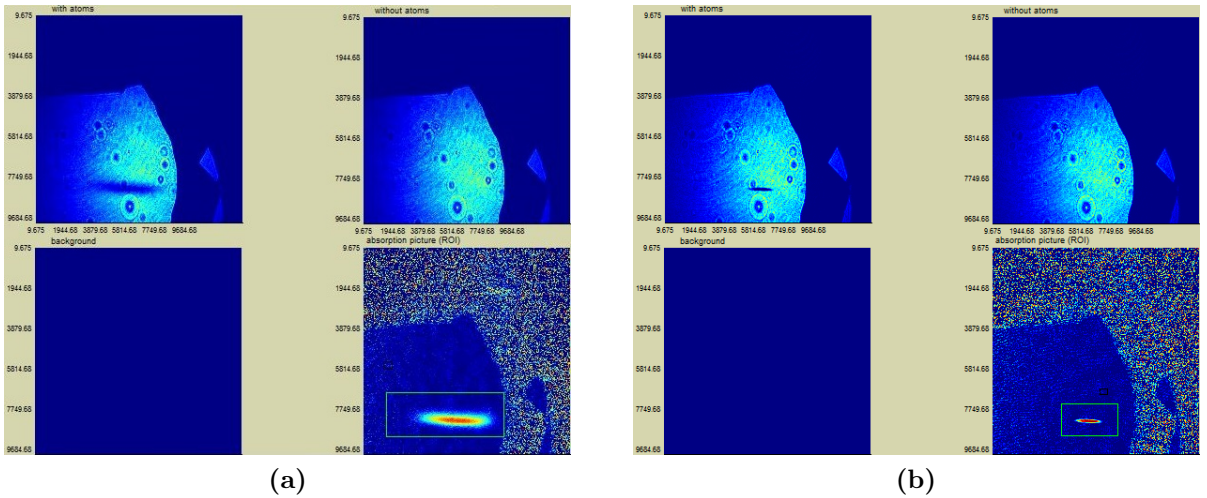
Fig. 4.11: C-GUI clouds for different rf signal ramps. In order to perceive the vast effect, all the absorption imaging pictures displayed in the *Acquistion* tab are shown.
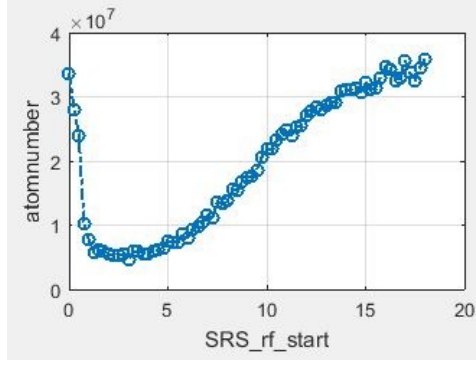
Fig. 4.12: Trap bottom spectroscopy. The atom number depends on the frequency of a constant rf knife. Such a measurement can be used to estimate the frequency range needed for evaporative cooling. This is for example utilized in [57].

(a)	(b)
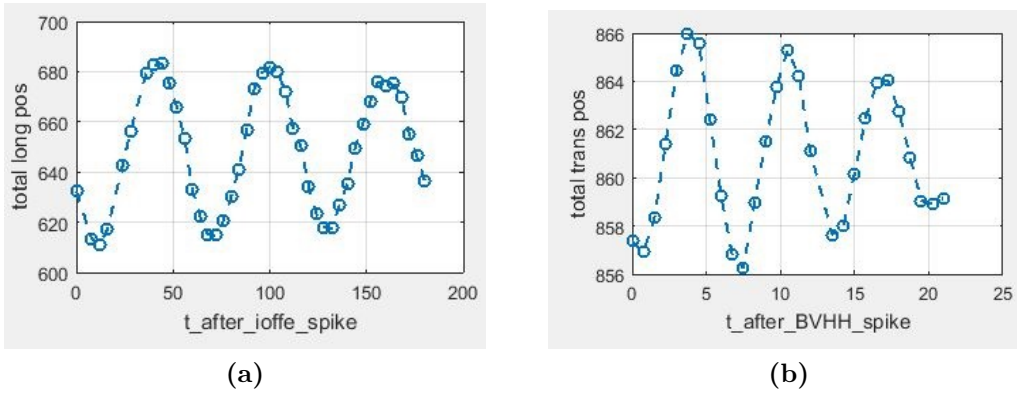
Fig. 4.13: Oscillations of the cloud position induced by a short spike on the Ioffe current **(a)** respectively the BVHH_away field **(b)**. As can be inferred from the time axes (both ms), the trapping frequencies considerably differ, being ten times higher in vertical direction. This stems from the asymmetric potential formed by adding the Ioffe coil.

4.5 Chip quench implementation: Q-GUI

The quench interface is nothing but a C-GUI augmented with some new channels and parameters required for quenching. Recently, the quench cycle has already been employed for first measurements on the evidence of a remnant magnetization in the chip wire. This section focuses on the implementation of quenching the superconductor at different points in time. A first hint on the history dependence of the current distribution inside the chip wire is given in ch. 6.

4.5.1 GUI expansion

The quench setup requires two signals to be added to the cycle: An analog channel is used for controlling the Mephisto injection current. In particular, it only ramps the current up above the lasing threshold for quenching, and keeps it below over the remaining cycle duration. The supplied voltage level determines the laser output power, for which the channel was calibrated according to fig. 3.26. A digital channel controls the shutter in front of the beam outlet. The shutter is opened respectively closed, when the injection
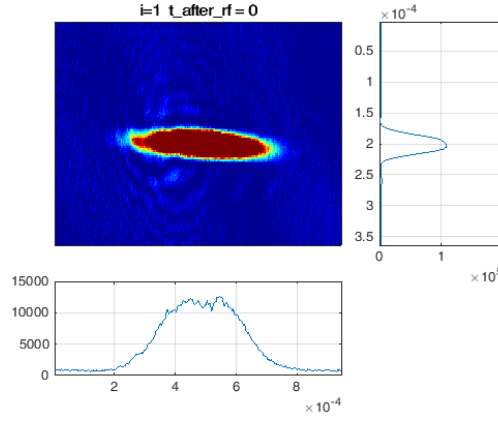
(a)
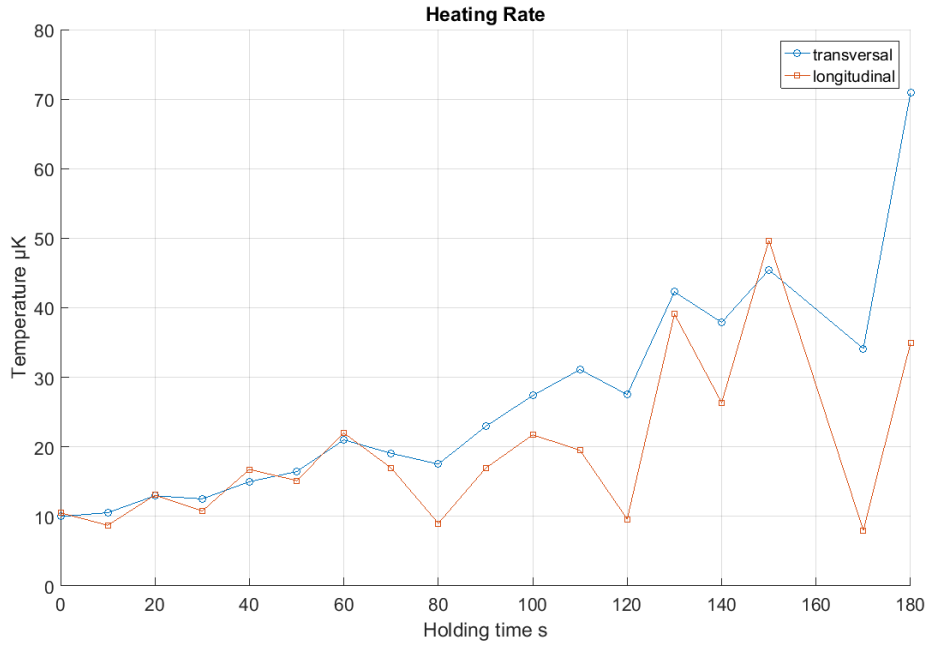
(b)

Fig. 4.14: (a) shows an evaporatively cooled cloud of $\sim 2.5 \times 10^6$ atoms. It was exposed to a 70 s rf ramp from 30 to 1.5 MHz. The image was acquired in low magnification configuration on the main imaging axis. The diffraction features suggest, that the resolution was not high enough for calculating the actual properties. The heating rate of this cold cloud in the QUIC trap along the two perpendicular axes is depicted in **(b)**.

current has already reached the desired level. For this, the associated delay must be taken into account, so that a constant optical power over the entire exposure time is guaranteed. Simultaneously, the chip current channel supplies the Z-wire with a quench current I_q. This implies modifying another digital channel, that serves as a switch for connecting the atomchip to its source. The simplest way of quenching the wire is waiting for the end of the standard C-GUI cycle. Then, a sequence containing all the required signals can be supplied (fig. 4.15). However, this approach is expected not to be sufficient for performing an accurate analysis of the hysteresis behavior.
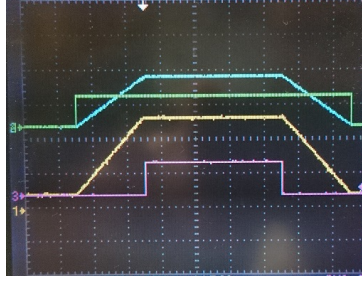
Fig. 4.15: The signals necessary for a quench. The upper two are for the chip current, first establishing the connection to the source and then ramping up I_q. At the same time, the laser injection current is increased. Finally, the shutter is opened briefly by the digital signal at the screen bottom.

4.5.2 Quench timing

There are different points in time within the experimental cycle, at which it makes sense to erase the magnetization memory. During the initial realization of the Q-GUI, quenching the wire before the start of the next cycle was made possible. But as outlined in ch. 2.5.3, the virgin state of the superconductor can be destroyed by external magnetic fields anytime. Between the last part of the magnetic transport and the chip trap, plenty of magnetic fields are present in the chip's vicinity. This is therefore expected to induce a remnant magnetization in the wire, which can only be reviewed by quenching the latter during the different trapping phases.

When the quenching sequence is executed can be chosen by adjusting the variable **quench_delay**. Initializing a quench during any of the trapping phases implies, that the atoms are already up in the science chamber and possibly hit by the laser beam. This might demand aligning the quenching laser to another spot than the center of the Z-wire. Although the wavelength is significantly off resonance, shining so much power through the cloud could have a noticeable impact on the atoms. As mentioned in ch. 3.5.2, a potential alternative is given by the contact pads. This has recently been tested and clearly led to a voltage rise as well. The question for the optimal time for a quench will be subject to near-future measurements.

Another idea features quenching the wire during the chip trap phase. If a persistent supercurrent is induced, forming a chip trap without a transport current should be possible [48]. Such a trap could be immediately turned off by means of a quench, erasing the magnetization. This would constitute a method for time-of-flight measurements in a zero-current trap. Furthermore, quenching at the end of a standard chip trap might influence the expansion of the atom cloud as well.

5 Experimental challenges

The complexity of the QuIC experiment (cf. ch. 3) can make diagnosing occurring problems difficult. This chapter aims at serving as a guideline for identifying issues with the optics. It furthermore comprises the major challenges faced during the course of the experiment. Typical malfunctions, also including the electronics, device communication and software issues, are discussed in appx. A.

5.1 Laser setup analysis

There are some common reasons preventing the experiment from working. If the lasers are involved, the problem is very likely to be evident in the MOT or the magnetic trap. If the MOT does not work, the vital components to be checked are the AOMs and the shutters. The three drivers for Cooler, Repump and Pump AOM must be off and the first two set to external, the third one to internal level. The correct shutter control switch positions are *N.O.* (**n**ormally **o**pen) for the Cooler shutter and *TTL* for everything else. It is worth checking the locking points too, which are obtained from figs. 3.7, 3.8 and 3.9. In case a laser keeps falling out of lock, the PID gain or the detuning ramps might have to be adjusted, which is explained in detail in appx. A.2.1.

The basic alignment of the setup can be very quickly reviewed. Checking the different optical paths requires turning on the associated AOMs (best being set to internal level) and opening the shutters. The necessary settings can be inferred from ch. 3.3.2. If the cooling beam has been misaligned and does not properly enter the beam expander (cf. fig. 3.12) any more, no atom cloud can be observed. A rather asymmetric cloud usually stems from inaccurate MOT alignment or improper bias fields. If the cloud exhibits a very strange shape despite proper alignment, the reason might be a severely non-uniform cooling beam. Ch. 5.2 basically provides an introduction to setting up the MOT, but also mentions the last observation. The emergence of a MOT cloud moreover depends on the presence of the repump beam. The latter must co-propagate with the cooling beam, so they need to overlap right after mixing them as well as before entering the telescope.

However, a reasonably big amount of atoms collected in the MOT does not necessarily guarantee a satisfactory cloud in the molasses or the magnetic trap. The most common source for a such a discrepancy is troubles with the laser locking, which are confronted in appx. A.2.1. During the course of the experiment, the cloud in the magnetic trap furthermore temporarily shrank to less than half its size because the optical pumping did not work. This problem is discussed and resolved in ch. 5.3. The pump beam increases the number of trapped atoms by a factor ~ 2.5. The alignment of the pump beam and the three imaging axes can be checked by measuring the optical power leaving the respective fibers.

5.2 MOT setup procedure

One of the major challenges encountered was finding a reproducible way of setting up the magneto-optical trap. This involves not only the beam alignment, but power distribution, beam polarization and bias field settings have to be considered as well. The

approach implemented in this thesis and explained briefly in this section led to the best magnetic trap results in the experiment ever. It is featured here, since many iterations were required, before a reproducible procedure could be found. A step-by-step instruction is given in appx. E.

Beam alignment   The expanded beam entering the MOT setup (cf. fig. 3.13) must exhibit a very uniform shape, especially in the center. This requires cutting off some perturbing fractions from the yet unwidened beam. Otherwise, the MOT cloud is considerably distorted by the spatial modes. For forming an intersection region in the center of the chamber, alignment t-shirts (fig. 5.1) inserted into the telescope are utilized, which yield a very small beam diameter representing the center of the widened beam. The light spots can be centered on the MOT chamber windows by means of specially tinkered alignment caps (fig. 5.2). A polarization filter is used for reducing the optical power and with it the reflections on the cap surface. On each of the three perpendicular axes, one of the two beams is first aligned to both window centers, which makes it pass through the center of the MOT chamber. The two reference points for the second beam are the PBS, where it is overlapped with its counterpart, and the window further away from the beam splitter.

Power distribution and polarization   The power of the six beams is equalized right in front of the windows. The last iris before the MOT setup is used for reducing the beam diameter. The half-wave plates are adjusted for varying the power distribution. Some unexpected troubles with degrading beam splitter cubes, that were discovered during this process, are treated in appx. A.2.2. The polarization is measured either right before the

Fig. 5.1: One of the alignment t-shirts. Placed at both ends of the beam expander, those allow for making the beam enter it parallel to the tabletop plane.

| (a) | (b) |
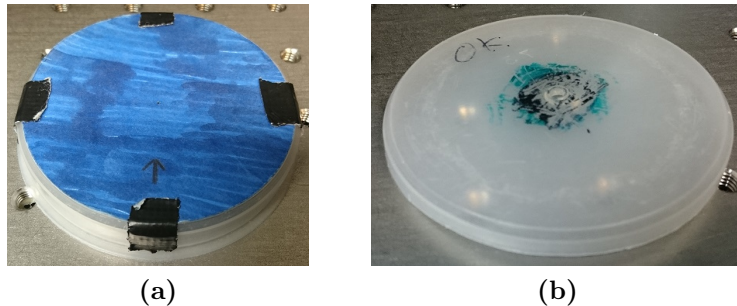
Fig. 5.2: The two different alignment caps. For five of the six axes, a recently designed one producing only few reflections is used **(a)**. For $-X$, an old one with a cut rim **(b)** must be used.

beam is entering or right after it is leaving the chamber. An overview of the necessary polarizations is given in appx. E.2.

Bias field adjustment   The bias fields are adjusted by varying the corresponding variables in the M-GUI (cf. ch. 4.2.2). The current running through the MOT coils is increased and the TOF decreased, which yields the approximate position of the magnetic trap minimum. After resetting the coil current, the centers of the MOT and the molasses cloud are simultaneously matched with this minimum by adjusting the bias fields. The highest atom numbers observed were achieved by following this procedure. A possible explanation is the fact, that the atoms have to travel the shortest possible way between the molasses phase, where the magnetic field is turned off, and the MOT respectively the magnetic trap phases, where the cloud is pulled towards the minimum of the MOT coil field. The most symmetric atom cloud ever recorded is shown in fig. 5.3.

5.3   Frequency shift of the optical pump beam

In case optical pumping is not working, the atom count in the magnetic trap is significantly reduced. If the pump beam has no observable effect, a few simple things can be checked: With the Cooler AOM off and the Pump AOM on, the optical power leaving the associated fiber must be high enough. Usually $\sim 8\,\mathrm{mW}$ are sufficient. The beam leaving the fiber outcoupler must not be cut anywhere and should pass the MOT chamber centrally. It is advantageous to simply make it co-propagating with the imaging beam. Furthermore, circular polarization is required (cf. ch. 2.1), in the current setup CR light. It is possible, that the calibration of the bias coils utilized for defining the quantization axis somehow changes. However, a vast alteration of the magnetic fields generated by this coils would immediately be discernible in the shape of the MOT cloud. The same holds for an overall shift of the cooling laser frequency.

All the potential error sources mentioned so far could be ruled out, when the optical pumping had gone missing at some point (cf. ch. 3.3.1). Scanning the pump detuning revealed, that the atom number slowly increased again for more negative values of δ. This suggested a considerable shift of only the frequency of the pump beam. Ideally, the origin for this behavior was not found in the laser. The initial shift made the optimal frequency leave the accessible detuning range, but was still sufficiently small. Thus, it

(a)   (b)
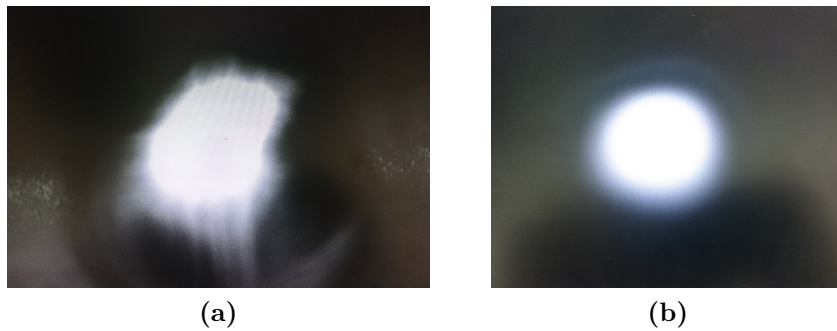
Fig. 5.3: Rather symmetric MOT in live mode on both cameras, the MOT live cam **(a)** and the MOT camera **(b)**.

could be compensated for by modifying the AOM double-pass setup. The frequency of the signal provided by the AOM driver can be varied within a certain range. Changing it only requires moving the iris blocking the zero order and the retro-reflecting mirror (cf. fig. 3.12). But once the shift became larger, the limits of the tunability were reached soon. Consequently, the effort on resolving the problem had to be increased.

The main suspect was the modulator itself. In order to review its performance, a setup for beating the zeroth and the first order beam was established (fig. 5.4). By means of a flip mirror, it is possible to direct the two beams into this setup instead of to the fiber. They are mixed in a PBS and aligned to a fast PD, which provides high frequency resolution when adding a $50\,\Omega$ resistor. Employing this setup, the AOM was ruled out as an error source either: With the driver on, the PD provided a voltage signal oscillating with the driver frequency, after turn-off the oscillation vanished.

The problem was therefore temporarily circumvented by changing the entire locking scheme. The course of action is extensively described in appx. C. The combination of an AOM driver frequency of $100\,\mathrm{MHz}$ and a pump detuning of $-100\,\mathrm{MHz}$ allowed for attaining a reasonable atom count again. Compared to the original settings, this meant a shift of $\sim 100\,\mathrm{MHz}$, which illustrates the magnitude of the deviation. It was possible to revert to the standard scheme, when the error source was finally located: The frequency shift was caused by the SM (**s**ingle **m**ode) fiber leading the beam to the MOT chamber. Replacing the fiber shifted the optimal detuning back to approximately the original level. As discussed with colleagues, this observation contradicts to all knowledge on how a fiber can manipulate a laser beam. The best guess so far was some optical feedback, although chances for this are not too high: The beam takes a very long path from the fiber input coupler back to the laser. For this reason, this case somehow remains a mystery.
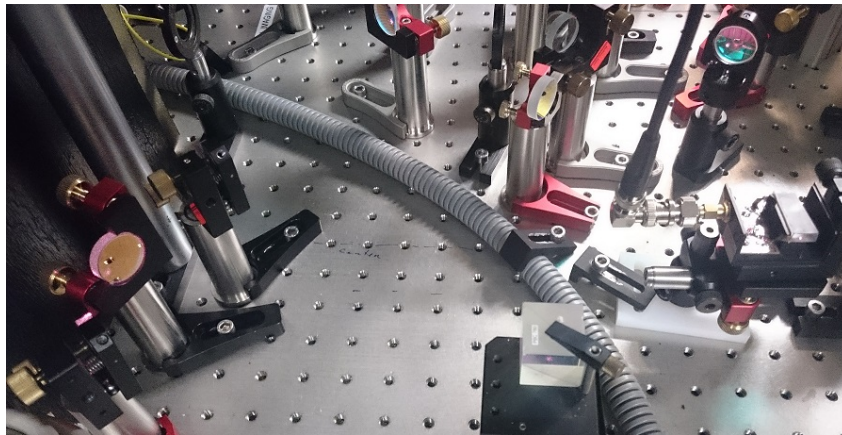
Fig. 5.4: The setup for beating the two Pump AOM orders with each other. The flip mirror in the top right corner reflects the two resulting beams onto different mirrors. Eventually, they are mixed in the PBS at the bottom and directed into a fast PD.

6 Results and prospects

The goal of hybrid quantum systems has already been discussed in ch. 1.1. However, there are other prospects that are also interesting. The recent progress first of all comprises the implementation of a quenching setup. This allows for resetting the superconducting atomchip to its virgin state within milliseconds. Furthermore, the optical setup has been significantly improved. This provides atom numbers never achieved before. Consequently, attaining a big, but still extremely dense cloud confined to a Z-wire trap is within reach. Very recent measurements on cooling in the chip trap suggest, that this claim will be proven true anytime soon.

The imminent application of these achievements is the detailed characterization of the magnetization memory of the niobium wire. Using the ultracold atoms as a magnetic field sensor, the quenching setup can be utilized for analyzing the response of the superconductor to magnetic field and current sequences. First tests on this revealed, that the distance of the cloud to the atomchip depends indeed on the current history. Fig. 6.1 shows such distance measurements for different maximum currents. These preliminary results already constitute evidence for the hysteresis behavior. They furthermore emphasize the successful incorporation of the quenching in the experimental cycle. It was possible to reset the superconductor in the presence of the atom cloud by aligning the quenching laser to the contact pads of the chip.
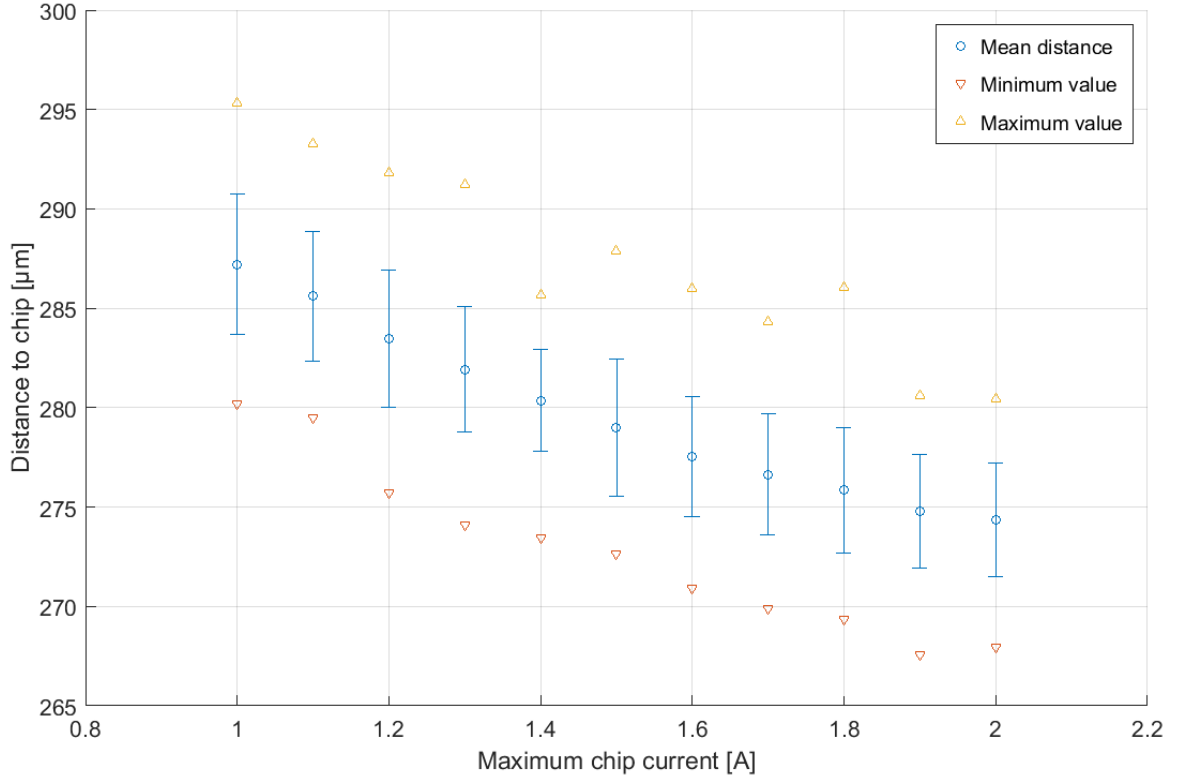
Fig. 6.1: Distance between the atom cloud and the chip surface for varying maximum current. It was measured at a transport current of 1 A and a bias field of 8 G, but for various previously reached current maxima. During each cycle, the niobium wire was quenched right before loading the atoms from the QUIC trap.

73

In conclusion, it could be shown, that the current flow along the niobium wire massively depends on the current history. This suggests, that earlier data with older chip iterations were influenced by a remnant magnetization formed by the transport current. This was the main conclusion of [17], as the data fits could be very well adapted to the associated models. The quenching setup now allows for full control of the transport current distribution on a superconducting atomchip. For this reason, it will be easily possible to tailor various current distributions, as their shape strongly depends on the history (fig. 6.2). This will constitute a novel atomchip technology for ultracold atoms, as programming superconductors in this way would allow for designing custom trapping potentials. Combined with geometrical structures on an atomchip, arbitrarily shaped trapping structures could be created, implying plenty of new applications for chip design. An interesting perspective is the generation of ultracold atom arrays, which would allow for simulating different physical systems.

Some further ideas cover the emergence of superconducting vortices in type-II superconductors. If the flux quanta can be sensed and studied by means of cold atoms, they might be utilized for forming magnetic traps as well. Consequently, small-spaced lattice traps could be created, that would allow for performing condensed matter simulations on scales never reached before. A more detailed insight in these visions is given in [17].

A currently ongoing process is the renewal of the experimental control [38]. In particular, this aims at facilitating the modification of the transport current sequences. The long lifetime in the science chamber exceeds the duration of a MOT loading cycle many times over. Therefore, it might be possible to gradually increase the atom count. A current sequence for merging two clouds has already been designed. This would provide atom numbers not achievable in standard setups with normal conductors. Further progress on the many perspectives will be reported in [46], [68] and [61].
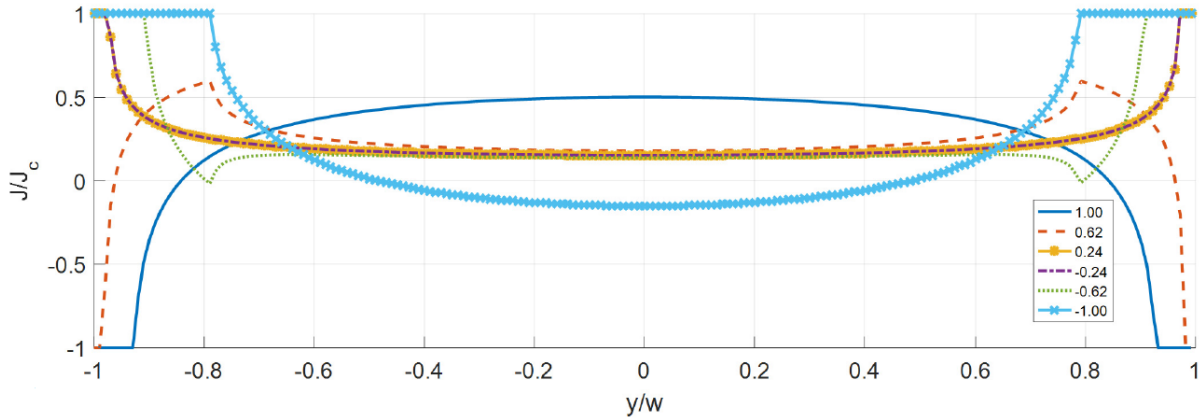
Fig. 6.2: Simulation of the current distribution in a wire for various histories[31]. The graphs shown here assume the exact same transport current $I_t = 0.24 I_C$, but different previously reached maximum currents.

---

[31]Diorico 2016 [17], ch. 7.3, fig. 7.14a

Acknowledgments

References

[1] *Properties of superconductors*, in CRC Handbook of Chemistry and Physics, Internet Version 2005, D. Lide, ed., CRC Press, 2005.

[2] *SuperPower 2G HTS wire specifications.* Available online at `http://www.superpower-inc.com/system/files/SP_2G+Wire+Spec+Sheet_for+web_2012FEC_v2_1.pdf`, 2012.

[3] C. S. Adams and E. Riis, *Laser cooling and trapping of neutral atoms*, Progress in Quantum Electronics, 21 (1997), pp. 1–79.

[4] R. Amsüss, *Development of a source of ultracold atoms for cryogenic environments*, Diploma thesis, Vienna University of Technology, 2008.

[5] J. Bardeen, L. N. Cooper, and J. R. Schrieffer, *Microscopic theory of superconductivity*, Physical Review, 106 (1957), pp. 162–164.

[6] M. Bartenstein, D. Cassettari, T. Calarco, A. Chenet, R. Folman, K. Brugger, A. Haase, E. Hartungen, B. Hessmo, A. Kasper, P. Krüger, T. Maier, F. Payr, S. Schneider, and J. Schmiedmayer, *Atoms and wires: Toward atom chips*, IEEE Journal of Quantum Electronics, 36 (2000), pp. 1364–1377.

[7] C. P. Bean, *Magnetization of hard superconductors*, Physical Review Letters, 8 (1962), pp. 250–253.

[8] ——, *Magnetization of high-field superconductors*, Reviews of Modern Physics, 36 (1964), pp. 31–39.

[9] A. V. Bobyl, D. V. Shantsev, T. H. Johansen, W. N. Kang, H. J. Kim, E. M. Choi, and S. I. Lee, *Current-induced dendritic magnetic instability in superconducting MgB_2 films*, Applied Physics Letters, 80 (2002), pp. 4588–4590.

[10] E. H. Brandt and M. Indenbom, *Type-II-superconductor strip with current in a perpendicular magnetic field*, Physical Review B, 48 (1993), pp. 12893–12906.

[11] S. Bühler-Paschen and P. Mohn, *Festkörperphysik II.* Lecture notes, Vienna University of Technology, 2013.

[12] J. Carlstrom, J. Garaud, and E. Babaev, *Semi-meissner state and non-pairwise intervortex interactions in type-1.5 superconductors*, Physical Review B, 84 (2011), p. 134515.

[13] Coherent Inc., *Mephisto laser operator's manual*, 2013. Part No. 1265350 Rev. AA.

[14] J. Dalibard and C. Cohen-Tannoudji, *Laser cooling below the Doppler limit by polarization gradients: simple theoretical models*, Journal of the Optical Society of America B, 6 (1989), pp. 2023–2045.

77

[15] J. Denschlag, D. Cassettari, and J. Schmiedmayer, *Guiding neutral atoms with a wire*, Physical Review Letters, 82 (1999), pp. 2014–2017.

[16] D. Dew-Hughes, *The critical current of superconductors: an historical review*, Low Temperature Physics, 27 (2001), pp. 713–722.

[17] F. R. Diorico, *Novel atomchip technologies with superconductors*, PhD thesis, Vienna University of Technology, 2016.

[18] E. A. Donley, T. P. Heavner, F. Levi, M. O. Tataw, and S. R. Jefferts, *Double-pass acousto-optic modulator system*, Review of Scientific Instruments, 76 (2005), p. 063112.

[19] R. C. Dougherty and J. D. Kimel, *Temperature dependence of the superconductor energy gap*, arXiv preprint arXiv:1212.0423, (2012).

[20] T. Esslinger, I. Bloch, and T. W. Hänsch, *Bose-Einstein condensation in a quadrupole-ioffe-configuration trap*, Physical Review A, 58 (1998), pp. 2664–2667.

[21] R. Fermani, T. Müller, B. Zhang, M. J. Lim, and R. Dumke, *Heating rate and spin flip lifetime due to near field noise in layered superconducting atom chips*, arXiv preprint arXiv:0912.2183, (2009).

[22] D. K. Finnemore, T. F. Stromberg, and C. A. Swenson, *Superconducting properties of high-purity niobium*, Physical Review, 149 (1966), pp. 231–243.

[23] R. Folman, P. Krüger, D. Cassettari, B. Hessmo, T. Maier, and J. Schmiedmayer, *Controlling cold atoms using nanofabricated surfaces: Atom chips*, Physical Review Letters, 84 (2000), pp. 4749–4752.

[24] Georgia Institute of Technology, *Measuring the hyperfine levels of rubidium using saturated absorption spectroscopy*, 2009. Lab manual, available online at `http://advancedlab.physics.gatech.edu/labs/SaturationSpectroscopy/SatSpecManual.pdf`.

[25] B. Gerstenecker and L. Schmid, *Laser frequency stabilization with TOPTICA DLC pro*, Project thesis, Vienna University of Technology, 2015.

[26] S. Gov, S. Shtrikman, and H. Thomas, *Magnetic trapping of neutral particles: Classical and quantum-mechanical study of a Ioffe–Pritchard type trap*, Journal of Applied Physics, 87 (2000), pp. 3989–3998.

[27] K. C. Harvey and C. J. Myatt, *External-cavity diode laser using a grazing-incidence diffraction grating*, Optics Letters, 16 (1991), pp. 910–912.

[28] S. Haslinger, *Cold atoms in a cryogenic environment*, PhD thesis, Vienna University of Technology, 2011.

[29] C. Heistracher, *TBA*, Project thesis, Vienna University of Technology, 2017.

[30] ——, *TBA*, Project thesis, Vienna University of Technology, 2017.

[31] R. Huebener, R. T. Kampwirth, R. L. Martini, T. W. J. Barbee, and Z. R. B., *Critical current density in superconducting niobium films*, IEEE Transactions on Magnetics, 11 (1975), pp. 344–346.

[32] C. Hufnagel, *Superconducting microtraps for ultracold atoms*, PhD thesis, Vienna University of Technology, 2011.

[33] P. Kauranen, *Frequency modulation (FM) spectroscopy*, Diploma paper, Lund Institute of Technology, 1989.

[34] M. Keil, O. Amit, S. Zhou, D. Groswasser, Y. Japha, and R. Folman, *Fifteen years of cold matter on the atom chip: promise, realizations, and prospects*, Journal of Modern Optics, 63 (2016), pp. 1840–1885.

[35] W. Ketterle and N. J. van Druten, *Evaporative cooling of trapped atoms*, Advances in Atomic, Molecular, and Optical Physics, 37 (1996), pp. 181–236.

[36] C. Kittel, *Introduction to solid state physics*, John Wiley & Sons, Inc, 8th ed., 2005, ch. 10.

[37] C. Koller, *Towards the experimental realization of hybrid quantum systems*, PhD thesis, Vienna University of Technology, 2012.

[38] J. Kurz, *Migration of the QuIC experiment from MATLAB to QiController*, Bachelor's thesis, Vienna University of Technology, 2017.

[39] I. Ladany, J. T. Andrews, and G. A. Evans, *Distributed feedback lasers*, Contractor Report 4154, NASA, 1988.

[40] M. Lara, B. L. Lev, and J. L. Bohn, *Loss of molecules in magneto-electrostatic traps due to nonadiabatic transitions*, Physical Review A, 78 (2008), p. 033433.

[41] R. Liang, P. Dosanjh, D. A. Bonn, W. N. Hardy, and A. J. Berlinsky, *Lower critical fields in an ellipsoid-shaped $YBa_2Cu_3O_{6.95}$ single crystal*, Physical Review B, 50 (1994), p. 260407.

[42] N. Lippok, *A magnetic transport for ultracold atoms*, Diploma thesis, Vienna University of Technology, 2008.

[43] F. London, *On the problem of the molecular theory of superconductivity*, Physical Review, 74 (1948), pp. 562–573.

[44] H. J. Metcalf and P. van der Straten, *Laser cooling and trapping of atoms*, Journal of the Optical Society of America B, 20 (2003), pp. 887–908.

[45] ——, *Laser cooling and trapping of atoms*. Available online at `http://info.phys.unm.edu/~ideutsch/Classes/Phys500S09/Downloads/handpubl.pdf`, 2006. Review of the work of Metcalf and van der Straten on this topic, mainly comprising [44]; found on the course webpage of Prof. Deutsch, University of New Mexico.

[46] S. Minniberger, *TBA*, PhD thesis, Vienna University of Technology, 2017.

[47] S. Minniberger, F. Diorico, S. Haslinger, C. Hufnagel, C. Novotny, N. Lippok, J. Majer, C. Koller, S. Schneider, and J. Schmiedmayer, *Magnetic conveyor belt transport of ultracold atoms to a superconducting atomchip*, Applied Physics B, 116 (2014), pp. 1017–1021.

[48] T. Mukai, C. Hufnagel, A. Kasper, T. Meno, A. Tsukada, K. Semba, and F. Shimizu, *Persistent supercurrent atom chip*, Physical Review Letters, 98 (2007), p. 260407.

[49] T. Müller, X. Wu, A. Mohan, A. Eyvazov, Y. Wu, and R. Dumke, *Towards a guided atom interferometer based on a superconducting atom chip*, New Journal of Physics, 10 (2008), p. 073006.

[50] T. Müller, B. Zhang, R. Fermani, K. S. Chan, M. J. Lim, and R. Dumke, *Programmable trap geometries with superconducting atom chips*, Physical Review A, 81 (2010), p. 053624.

[51] S. Nakanishi, H. Ariki, H. Itoh, and K. Kondo, *Frequency-modulation spectroscopy of rubidium atoms with an AlGaAs diode laser*, Optics Letters, 12 (1987), pp. 864–866.

[52] C. Novotny, *Transport of ultracold atoms into a superconducting QuIC-trap*, Diploma thesis, Vienna University of Technology, 2011.

[53] R. C. Pooser, A. M. Marino, V. Boyer, K. M. Jones, and P. D. Lett, *Quantum correlated light beams from non-degenerate four-wave mixing in an atomic vapor: the D1 and D2 lines of ^{85}Rb and ^{87}Rb*, Optics Express, 17 (2009), pp. 16722–16730.

[54] D. W. Preston, *Doppler-free saturated absorption: Laser spectroscopy*, American Journal of Physics, 64 (1996), pp. 1432–1436.

[55] D. E. Pritchard, *Cooling neutral atoms in a magnetic trap for precision spectroscopy*, Physical Review Letters, 51 (1983), pp. 1336–1339.

[56] O. Romero-Isart, C. Navau, A. Sanchez, P. Zoller, and J. I. Cirac, *Superconducting vortex lattices for ultracold atoms*, Physical Review Letters, 111 (2013), p. 145304.

[57] C. Roux, A. Emmert, A. Lupascu, T. Nirrengarten, G. Nogues, M. Brune, J.-M. Raimond, and S. Haroche, *Bose-Einstein condensation on a superconducting atom chip*, Europhysics Letters, 81 (2008), p. 56004.

[58] J. Schmiedmayer, R. Folman, and T. Calarco, *Quantum information processing with neutral atoms on an atom chip*, Journal of Modern Optics, 49 (2002), pp. 1375–1388.

[59] T. Schumm, S. Hofferberth, L. M. Andersson, S. Wildermuth, S. Groth, I. Bar-Joseph, J. Schmiedmayer, and P. Krüger, *Matter-wave interferometry in a double well on an atom chip*, Nature Physics, 1 (2005), pp. 57–62.

[60] U. Schünemann, H. Engler, R. Grimm, M. Weidemüller, and M. Zielonkowski, *Simple scheme for tunable frequency offset locking of two lasers*, Review of Scientific Instruments, 70 (1999), p. 242f.

[61] N. Shokrani, *TBA*, Master's thesis, Vienna University of Technology, 2017.

[62] D. A. Smith, S. Aigner, S. Hofferberth, M. Gring, M. Andersson, S. Wildermuth, P. Krüger, S. Schneider, T. Schumm, and J. Schmied-mayer, *Absorption imaging of ultracold atoms on atom chips*, Optics Express, 19 (2011), pp. 8471–8485.

[63] D. A. Steck, *Rubidium 87 D Line Data*. Available online at `http://steck.us/alkalidata`, 2015. Revision 2.1.5.

[64] L. R. Testardi, *Destruction of superconductivity by laser light*, Physical Review B, 4 (1971), pp. 2189–2196.

[65] M. Thirumaleshwar and S. V. Subramanyam, *Gifford-McMahon cycle – a theoretical analysis*, Cryogenics, 26 (1986), pp. 177–188.

[66] P. Treutlein, P. Hommelhoff, T. Steinmetz, T. Hänsch, and J. Reichel, *Coherence in microchip traps*, Physical Review Letters, 92 (2004), p. 203005.

[67] J. Verdú, H. Zoubi, C. Koller, J. Majer, H. Ritsch, and J. Schmied-mayer, *Strong magnetic coupling of an ultracold gas to a superconducting waveguide cavity*, Physical Review Letters, 103 (2009), p. 043603.

[68] T. Weigner, *TBA*, Master's thesis, Vienna University of Technology, 2017.

[69] P. Weiss, M. Knufinke, S. Bernon, D. Bothner, L. Sárkány, C. Zimmer-mann, R. Kleiner, D. Koelle, J. Forthág, and H. Hattermann, *Sensitivity of ultracold atoms to quantized flux in a superconducting ring*, Physical Review Letters, 114 (2015), p. 113003.

[70] M. Zehetner, *Theorie der Supraleitung*. Lecture notes, Vienna University of Technology, 2013.

[71] E. Zeldov, J. R. Clem, M. McElfresh, and M. Darwin, *Magnetization and transport currents in thin superconducting films*, Physical Review B, 49 (1993), pp. 9802–9822.

[72] B. Zhang, R. Fermani, T. Müller, M. J. Lim, and R. Dumke, *Design of magnetic traps for neutral atoms with vortices in type-II superconducting microstructures*, Physical Review A, 81 (2010), p. 063408.

Appendices

A Troubleshooting

This chapter provides an overview of common issues with the electronics, optics and the software. In many cases, one of the devices will simply be off or one of the switches (especially for AOMs and shutters) in the wrong position. In addition, PC programs might be stuck or have lost connection to the associated devices. In order to narrow the scope within the experimental cycle, where an error occurs, the different GUIs can be tested one after the other, following the chronological order in ch. 4. Upon this, it might already be evident, which part of the setup is afflicted.

A.1 Electronics

The most frequent error concerning the electronics is related to the transport currents. Sometimes, single coils are not supplied with the correct sequence or any current at all. This can be figured out by comparing the curves displayed in *Delta DAQ Complete.VI* and *Cryo DAQ Complete.VI* (cf. ch. 4.1.3) to fig. A.1. It is usually a malfunction of one of the switchboxes (for the deltas) or the switchboard (for the superconducting part). The

(a)

(b)
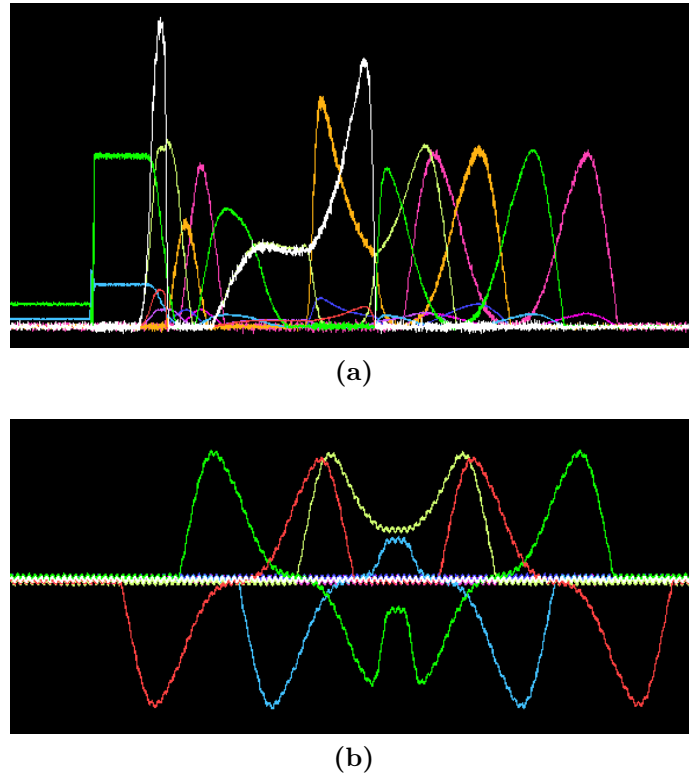
Fig. A.1: Transport current sequence. This example shows a transfer up into the science chamber and back into the MOT chamber. For the normal conducting part, only one direction is depicted **(a)**. For the superconducting one, the whole – and therefore symmetric – sequence is shown **(b)**.

boxes are equipped with LEDs, which should all be green. Otherwise, the reset button must be pressed. If the vertical transport does not work, simply shaking the switchboard a bit is worth a try. Usually, this already solves the problem. In case the currents of the normal conducting part are entirely missing, the safety relay might have disconnected the deltas from the heavy current line (cf. ch. 4.1.1). For the superconducting one, the connector feeding the current into the cryostat from the outside (cf. ch. 3.4) might be not plugged in.

The only other substantial issue associated with the electronics were superconducting coils quenching. This is possibly caused by an interplay of different factors like damaged HTCs, not good enough thermal anchoring, and incomplete radiation shielding (cf. ch. 3.4.1). Due to the rather recent renewal of these parts, these problems should be minimized in the future.

A.2 Optics

A brief guideline for diagnosing various problems with the optics is given in ch. 5.1. By far the most were encountered with the laser locking. Another observation is featured here as well, as degrading polarizing beam splitters do not seem to be a common issue.

A.2.1 Lock instabilities

A few times, frequency stability problems encountered could finally be solved by realigning the spectroscopy setups respectively the beating of reference and main laser. How the according beams had gradually misaligned, although being protected inside the laserbox, remained unclear. Besides potential vibrations, the BNC cables connected to the PD outputs might cause some traction and very slowly change the angle. The beams have to be made counter-propagating through the vapor cells, as a double-pass configuration is employed (cf. ch. 3.3.1). Then, the spectroscopy and the error signal can be maximized by adjusting the mirrors in front of the PDs. The higher the slopes of the error signal get, the more stable the locking points are. The same procedure can be applied to mixing the Pierluigi and the TA master. By optimizing the beam overlap, the error signal signal can be significantly improved.

The lock stability always depends on the selected PID gain, that can be too low or too high both. Lately, a default procedure of adjusting the different gains has been chosen: First, the reference laser is locked and the gain increased, until the error signal starts to oscillate. Then, it is decreased to the level, where it gets flat again, and the laser is unlocked and immediately locked again. The exact same procedure can be applied to the repump laser. Next, the main laser is locked too and the PID gain adjusted basically the same way. However, it needs to be reduced to slightly further below the oscillation limit. Finally, the TA master and the Pierluigi are both unlocked and locked one last time (in the reverse order). The magnetic trap cycle is started and the TA master's error signal attentively watched. In case slight oscillations occur at any point during the cycle, the gain has to be further decreased, until they vanish. Otherwise, chances for obtaining a reasonable cloud in the magnetic trap are very low, and the laser is very likely to fall out of lock. The fact that the MOT cloud often looks very good anyway can be misleading.

If the laser keeps leaving the lock for no obvious reason, varying the detuning ramp

times is worth a try. Since the FO lock only allows for a certain maximum ramp speed (cf. ch. 3.3.1), it is not able to deal with arbitrarily fast frequency changes. Especially the frequency jump between the MOT and the molasses detuning is very large. The same applies to the difference between molasses and image detuning. Thus, slightly increasing the associated ramp durations defined in the interface can possibly solve the problem. A typical indicator for a too fast ramp is the laser falling out of lock right after the MOT phase. This can be observed in the FFT of the beat signal. Moreover, the frequency is then completely off in the subsequent phases, and no atoms are imaged after the molasses or the magnetic trap.

On rare occasions, the lasers might stay locked over plenty of cycles, but already the MOT cloud looks rather small and seems to flicker. Furthermore, the atom count in the magnetic trap is distinctly reduced. This usually occurs, when of the two ECDLs is too close to a mode hop. It can be solved by changing the injection current, where for the TA master the seed laser current is used. Another rarely observed issue is caused by some special behavior of the main laser: Depending on the offset current, sometimes "bad" modes of the error signal arise. Locking the laser to such a mode, the atom cloud becomes considerably smaller too. The "bad" modes can be distinguished from the "good" ones by closely looking at the shape: In contrast to fig. 3.8, the former feature approximately equally high peaks. Adjusting the offset current and finding another mode does the trick.

A.2.2   Degrading beam splitters

Malfunctioning beam splitter cubes do not seem to be a very common issue. For this reason, it is worth mentioning, that they constitute a potential error source. This was figured out, when trying to optimize the power distribution of the MOT beams: Although in the first place the power distribution of the Z beam pair had been equalized by means of wave plate *Z2*, turning *Z1* completely destroyed the balance between $+Z$ and $-Z$. Instead of a tiny deviation, one beam suddenly was around four times stronger than the other. Measuring the power right after the PBS revealed, that the reason was to be found in the small part of the setup only consisting of half-wave plates and cubes.

In theory, a half-wave plate rotates an incoming linear polarization and a PBS splits up any beam into a vertically and a horizontally polarized part. Employing a polarization analyzer, the performance of the optical elements was reviewed. The wave plates seemed to work, but most of the beam splitters behaved nothing like ideally. Some exhibited slightly tilted axes with respect to the vertical or horizontal plane or small deviations from linear shape. Such distortions are not expected to have any considerable impact on the experiment. However, the polarization axis of the beam reflected by one of the cubes could be arbitrarily rotated by turning any of the wave plates in front. This suggests a dependence of the angle on input power. Another cube even assigned a circular polarization to the reflected light, again depending on the wave plate settings. It was not possible to find any references covering this strange behavior.

Ultimately, two of the five beam splitters were replaced by brand-new ones. They are used for splitting $+Z$ /$-Z$ and $+Y$/$-Y$. Several cubes were tested and the two most ideal ones chosen. It seems like even new cubes might already exhibit some serious performance constraints. Replacing the old ones was not too difficult: Trying to overlap the beams

at some reference points (e.g. a mirror and a quarter-wave plate) by moving around the PBS allows for placing it rather close to the original position. As the severe distortions occurred only on the reflecting axis, the broken cubes can probably still be used as beam cleaners. This means, that only the transmitted light is used, while the reflected one is hitting a beam dump. It is utilized for guaranteeing a merely linear polarization. An example for this can be found in the optical setup at QuIC (cf. fig. 3.12).

A.3   Software

Software issues are a very common problem, but can usually be solved quickly. If one of the VIs loses connection to the associated lab device, unplugging the USB (or GPIB) connector briefly probably helps. Mere software problems can sometimes only be solved by several PC restarts.

Device communication   On a regular basis, the two DAQ VIs (cf. ch. 4.1.3) are unable to connect to the DAQ cards. Pressing the *Clear Chart* button before starting increases the chances, that they work right away. Otherwise, the respective VI needs to be closed, then the USB connection to the DAQ card (inside the lab) is removed for around ten seconds and plugged back in. Next, *NI MAX* is opened on the PC. Under *Geräte und Schnittstellen*, the device is selected and reset. *Dev1* is the DAQ card for the superconducting part and *Dev2* for the normal conducting one. Now the program can be run again and – after pressing *Clear Chart* – it is started and should display the signals.

Serious problems can occur with the camera control programs. The one used for the main imaging in the science chamber (cf. ch. 4.4.1) regularly shows timing issues. Sometimes every third picture must be discarded because the calculated image is entirely red. The program controlling the MOT camera (cf. ch. 4.2.1) might suddenly stop working at all. In case the latter happens, stopping and closing the acquisition program, doing the same for the control program, and then restarting both usually does the trick. Thus, the troubles with the science chamber imaging are more severe, since so far there is not really a solution. A complete redesign is intended to be performed soon. Progress on this task will be reported in [30].

Software issues   The image acquisition can sometimes be buggy too. Typically, the *Acquisition* window either entirely stops reacting to pictures being taken by the control program, or a very long delay in between suddenly arises. Pressing *Stop Data Acquisition* and starting again sometimes helps, sometimes Matlab needs to be completely closed and the program restarted. Some weird error in the ADwin interface was encountered when programming the channels needed for the chip quenching: In any C-GUI, it is not possible to right-click fields not located in either the first or the last two rows or columns of the *Analog1* window. For editing those locked fields, the GUI must be loaded with wrong boolean settings. In particular, **adwin.magnetic_data.magnetic_transport** must be changed to **0** (instead of 1, cf. tab. 4.4). Upon this, the program does not manage to finish the loading process, since a lot of variables framed by other if-conditions cannot be found. Anyway, for some reason this makes the desired fields accessible. When finished with modifying the channels, the GUI can be saved as explained in appx. B.2.1 and reloaded with the correct settings.

B Computer control

B.1 Start-up

While the camera control programs need to be selected with respect to the chosen GUI, the image processing program is the same for all of them. The associated Matlab file is named *start.m* and contains the line "DataAcquistion" in the code. It is best started, when the respective camera control program is already running. This seems to facilitate a functioning communication between the two. Upon running it, multiple windows open up. The file path in the *Acquisition* window must be checked and possibly adapted to the current date. A section of this window is shown in figs. 4.11 and F.1. Moreover, the correct camera needs to be selected, as denoted in the corresponding section in ch. 4. Finally, the *Start Data Analysis* button can be pressed.

Although different types of GUIs exist, loading the interfaces follows the same procedure. There are a few vital parameters, which need to be adjusted to the type of measurements intended to be performed. The Matlab file *start.m* (this time on the AD-win PC) contains the boolean **adwin.magnetic_data.magnetic_transport**. The latter switches the transport current sequences on or off. **adwin.magnetic_data.oneway** and **adwin.magnetic_data.calculate_always** stand for single respectively repeated current calculation (for transport scans). **adwin.magnetic_data.vertical_transport** is used to switch between transport back to the MOT chamber and mere transfer into the science chamber. Note that it is set to zero, even if the cloud is transported vertically using the R-GUI (cf. ch. 4.3). These three booleans can be found in *magnetic_transport_parameters.m*.

Upon running the file *start.m*, the available interfaces can be found in the folder *magnetic_transport*. It makes sense to select the *Details* view and sort the files by date. Usually, the latest version of a GUI works right away. Older ones might still contain variables not existing in the code any more. In most cases, the missing parts have been deleted from or commented out in *calculate_variables.m*. For further explanation refer to appx. B.2.2). If no problems occur, the interface is loaded and plenty of windows pop up. These are described in great detail in appx. B.2.1. The initialization is finished, once the *Analog1* window shifts itself in front of the others.

When all lab devices and programs are ready for operation, a cycle can be started by hitting the huge *Start* button in the *BEC 2.2* window. Recently, a new issue has been encountered, which keeps occurring after each restart of Matlab: Upon starting the experiment for the first time, nothing happens. Only after entering the command **open set_progressbar.m** and then pressing *Stop* and *Start* again, the cycle is executed. Once the first picture has been sent to the *Acquisition* window, the regions of interest and of background can be selected. This is done by clicking the corresponding buttons and framing the desired areas. The top left *Start* button in *BEC 2.2* is used for scanning one or more variables. A detailed instruction on this is provided in appx. B.2.1.

B.2 ADwin user interface

B.2.1 Control windows

Since it is the easiest and therefore the neatest interface, the experimental control is explained in detail on the example of the M-GUI, where "M" stands for **m**agnetic trap.

It covers everything happening inside the MOT chamber. Once the interface is loaded, several windows pop up: Two for the analog channels, two for the digital channels, one containing variables, one with calculated variables, a delay overview, and the main control. A network tab exists too, but so far communication problems have never been indicated there.

Analog window(s) The analog windows contain an array with channel name and number on the left and a sequence of fields with three entries each (fig. B.1). The numbers refer to the assignment in fig. 3.5. The top left number defines the voltage, the letter next to it the type: **C** for constant or **R** for ramp. The bottom number sets the duration. The voltage calibration needs to be adjusted by pressing the *calibrate* button on the respective channel. Upon this, the associated Matlab file opens, where the calibration is defined. ADwin can output signals between **-10** and **+10 V**, so these boundaries have to be considered when setting the voltage levels. If the type letter of a field is changed to **R**, ADwin will perform a linear ramp. The latter starts from the value belonging to this field and ends at the value entered into the next field. All the time intervals are given in ms. If the mouse is placed on one of the type letters, the displayed number shows the overall time from the beginning of the cycle to the end of the selected field in the respective channel. The values can be modified by manually typing numbers in or by right-clicking the entry. Upon this, a list of all available variables is shown for selection.

Additionally, the *Analog1* window is the only one that is equipped with an options bar. The latter is used for saving the active GUI (File ▷ Save) and for setting channel limits (Files & Limits ▷ Limits). In the associated Matlab file, limits for all analog channels can be defined. Note that besides a warning showing up, any variable out of bounds is automatically deleted from the channel.

Fig. B.1: One of the analog channel windows. Here, a level and a duration for voltage signal output via the associated channel can be defined. This can be done either manually or by selecting one of the available variables.

Digital window(s) The digital channels provide the experiment with TTL signals. This means, that the level is either high (**H**, $\sim 5\,\text{V}$) or low (**L**, $\sim 0\,\text{V}$). Therefore, only time intervals (again in ms) need to be defined (fig. B.2). Again, channel name and number are denoted on the left. Furthermore, the initial level is set there, which will be active over the first time entry of the respective channel. For the second interval, ADwin will then supply the opposite voltage level. Over the third one, the original level is established again, and so forth. If a channel needs to be kept on the same level over a series of time constants or variables, zeros can be placed in between. As they then constitute the output time of the opposite voltage level, the latter does not change at all. If a channel is intended to be turned off for the rest of the cycle, the easiest solution is putting a **1** onto a "low" position and filling all the remaining fields with zeros.

Variable window The most important window for daily operation contains the variables (fig. B.3). The latter can be scanned, in order to either optimize their values or characterize the atom cloud. Setting a tick left to the name activates the field, which allows for renaming the variable. Spaces should be avoided, as the program cannot properly handle them. The first number after the name is the standard value. It is used as starting point for a potential scan as well. Scan mode is activated by ticking the box right to it. The second value stands for the ending point of a scan and the third one for the increment (positive or negative). Once a new variable has been added, it can immediately be inserted to one of the channels. When doing this, remember the set channel limits, which might cause the immediate removal of a variable off limits from the channel again.

#	Name	Lvl																
0	Cool AOM	H	10008.51	1431	L_expos_ON1	210.7	L_expos_ON2	250	0	0	0	0	0	0	0	0	0
1	Rep AOM	H	10009.51	INFINITY	0	0	0	0	0	0	0	0	0	0	0	0	0
2	Pump AOM	L	10008.51	T_pum_hold	1	0	0	0	0	0	0	0	0	0	0	0	0
3	Cooler Shut	L	10006.41	INFINITY	0	0	0	0	0	0	0	0	0	0	0	0	0
4	Pump Shutter	L	10001.51	6	1	0	0	0	0	0	0	0	0	0	0	0	0
5	vwar IMG shutter	L	11433.11	L_Sh_open1	205.5	L_Sh_open2	250	0	0	0	0	0	0	0	0	0	0
6	FireWire Trig	L	11438.11	1.21	209.48	1.21	200.68	1.21	100	0	0	0	0	0	0	0	0
7	O Image Shut	L	1	0	0	0	0	0	0	0	0	0	0	0	0	0	0
8	PixelFly Trig	L	1	0	0	0	0	0	0	0	0	0	0	0	0	0	0
9	MOT coil swit	L	10000	9.53	1419.98	466.58	0	0	0	0	0	0	0	0	0	0	0
10	Transport	L	0	0	0	0	0	0	0	0	0	0	0	0	0	0	0
11	Transport	L	0	0	0	0	0	0	0	0	0	0	0	0	0	0	0
12	MOT switch	H	1	0	0	0	0	0	0	0	0	0	0	0	0	0	0
13	Transport	L	0	0	0	0	0	0	0	0	0	0	0	0	0	0	0
14	Transport	L	0	0	0	0	0	0	0	0	0	0	0	0	0	0	0
15	Transport	L	0	0	0	0	0	0	0	0	0	0	0	0	0	0	0
16	Transport	L	0	0	0	0	0	0	0	0	0	0	0	0	0	0	0
17	Transport	L	0	0	0	0	0	0	0	0	0	0	0	0	0	0	0
18	Transport	L	0	0	0	0	0	0	0	0	0	0	0	0	0	0	0
19	Transport	L	0	0	0	0	0	0	0	0	0	0	0	0	0	0	0
20	Transport	L	0	0	0	0	0	0	0	0	0	0	0	0	0	0	0
21	Transport	L	0	0	0	0	0	0	0	0	0	0	0	0	0	0	0
22	Transport	L	0	0	0	0	0	0	0	0	0	0	0	0	0	0	0
23	Transport	L	0	0	0	0	0	0	0	0	0	0	0	0	0	0	0
24	Transport	L	0	0	0	0	0	0	0	0	0	0	0	0	0	0	0
25	Transport	L	0	0	0	0	0	0	0	0	0	0	0	0	0	0	0
26	V8	L	0	0	0	0	0	0	0	0	0	0	0	0	0	0	0
27	V9	L	0	0	0	0	0	0	0	0	0	0	0	0	0	0	0
28	Transport	L	0	0	0	0	0	0	0	0	0	0	0	0	0	0	0
29	unused	L	1	0	0	0	0	0	0	0	0	0	0	0	0	0	0
30	unused	L	1	0	0	0	0	0	0	0	0	0	0	0	0	0	0
31	Rep Sh	H	10007.61	INFINITY	0	0	0	0	0	0	0	0	0	0	0	0	0

Fig. B.2: One of the digital channel windows. Since there are only two possible settings, only the initial level and the timing must be defined. The fields alternately represent high or low level.

Use	Names	Values	Prim	Stop	Step	Value
☑	MOT_det	-29.5	☐	-35	-2.5	NaN
☑	Mol_det	-74	☐	-44	10	NaN
☑	Pump_det	-73.5	☐	-47	5	NaN
☑	B_comp_zero	5	☐	90	10	NaN
☑	B_comp_quant	450	☐	450	25	NaN
☑	INFINITY	1000	☐	0	0	NaN
☑	t_after_magnetic	1370	☐	8005	500	NaN
☑	Ladezeit	10000	☐	20000	1000	NaN
☑	t_magnetic	50	☐	2100	100	NaN
☑	TOF	10	☐	24	1	NaN
☑	C_lev_med	0.7	☐	0.7	0.02	NaN
☑	C_lev_mol	0.7	☐	0.5	0.01	NaN
☑	R_lev_med	0.8	☐	0.4	-0.02	NaN
☑	R_lev_mol	0	☐	0.1	-0.05	NaN
☑	IMAGE_TOF_notrans	1	☐	0	0	NaN
☑	IMAGE_mol_notrans	0	☐	0	0	NaN
☑	t_magnetic_con	0.8	☐	0	0	NaN
☑	T_pum_ram_6	0.01	☐	0	0	NaN
☑	T_level_ramp	1.1	☐	0	0	NaN
☑	Tmedium_hold	0	☐	0	0	NaN
☑	Tmedium	50	☐	15	1	NaN
☑	Tmedium_ram	2.02	☐	0	0	NaN
☑	T_pum_ram_3	0.22	☐	0	0	NaN
☑	T_det_reset	2.01	☐	0	0	NaN
☑	T_pum_hold	1	☐	0	0	NaN

Use	Names	Values	Prim	Stop	Step	Value
☑	T_pum_ram_1	0.9	☐	0	0	NaN
☑	T_mol_hold	5	☐	5	-1	NaN
☑	T_mol_ramp	2.5	☐	0	0	NaN
☑	T_startramp	5	☐	0	0	NaN
☑	T_wait	5	☐	0	0	NaN
☑	L_expos_OFF	50	☐	0	0	NaN
☑	L_expos_ON1	0.09	☐	0	0	NaN
☑	L_betw_pics	210	☐	0	0	NaN
☑	L_befo_bkg	200	☐	0	0	NaN
☑	L_expos_ON2	0.09	☐	0	0	NaN
☑	L_Sh_open1	5	☐	0	0	NaN
☑	L_Sh_bet_pics	201.5	☐	0	0	NaN
☑	L_Sh_open2	5	☐	0	0	NaN
☑	Acc_pump_Sh	5	☐	0	0	NaN
☑	Image_Detuning	-4.5	☐	-9	-0.5	NaN
☑	I_MOT_trap1	30	☐	10	-2	NaN
☑	I_MOT_trap2	68	☐	0	0	NaN
☑	Scan	1	☐	10	1	NaN
☑	R_lev_pump	1.2	☐	1.5	0.25	NaN
☑	B_comp_mol	5	☐	35	5	NaN
☑	B_comp_vert	50	☐	35	5	NaN
☑	B_comp_hor	190	☐	105	5	NaN
☐	unused	0	☐	0	0	NaN
☐	unused	0	☐	0	0	NaN
☐	unused	0	☐	0	0	NaN

(Right panel: all fields "unused", 0, 0, 0, NaN)

Fig. B.3: The *Variables & Movie* window. Here the variables are defined and scan parameters selected.

Calculated variables window   This window gives an overview of the variables calculated within the Matlab code. How to define them is explained in appx. B.2.2. Just like in the variable window, ticking the box activates the respective field. The only thing that can be changed is the name, since the value is always automatically determined during the experimental cycle. Any calculated variable intended to be inserted into a channel has to be included here.

Delay window   The delay overview contains and defines the time constants that need to be considered for triggering devices like optical shutters or cameras. These feature certain internal delays, i.e., after receiving the trigger signal, it takes (typically) a few ms, until the requested action is performed.

Main control   The main control window, actually called *BEC 2.2*, is used for starting and stopping the experimental cycle and, within this scope, scans too. The big bottom left button is the main start/stop-control, the top left one starts and stops a scan. Scanning one or more variables is only possible, when the cycle is already running and at least one scan box in the variable window is ticked and contains reasonable values. This includes the increment(s), as the sign is important here. On rare occasions, the software cannot deal with two-dimensional scans. Mostly communication problems with the camera control occur. The number of repeats on each scan point can be set too, moreover a progress bar and the cycle duration are displayed. Unfortunately, the estimated overall scan time is completely dispensable because always entirely wrong.

B.2.2   Code modifications

The only thing frequently changed in the Matlab code is the boolean variables depending on the type of GUI to be used (cf. ch. 4). Anyway, during the past year a lot of

modifications in *calculate_variables.m* were performed. Every calculated variable added to the respective window (appx. B.2.1) must be defined in this file. For this, one can use numerical constants as well as delays or variables existent in the associated windows, and other calculated variables too. At the beginning of each cycle, the program searches for the appropriate values and determines the solution. It is important to place each definition in the correct section within the file, which is separated into the different cases of the boolean variables. Otherwise, ADwin is not able to find the names the respective interface is trying to access. Since different versions of the same type of GUI may differ in the present variables as well, it might be necessary to comment certain lines in the Matlab code out from time to time. Besides that, some messages ADwin sends via the network and that depend on settings in the GUI are generated in this file. A recently modified example are the network messages sent to the rf signal generators. Since they contain values set in the variable window, they are concatenated in the Matlab code and then transferred to the associated LabView VIs (cf. ch. 4.1.1).

C   Alternative locking scheme

As discussed in chs. 3.3.1 and 5.3, the experiment was temporarily operated using another laser locking scheme. Besides the shift of the optical pump frequency, the atom cloud in the molasses respectively the magnetic trap had definitely been too small over several weeks, even considering that pumping was not working at that time. Therefore, an overall laser frequency shift was suspected and the possibility of modifying the locking scheme of the reference and the main laser was analyzed. This required determining the actual frequency differences between the locking points in both error signals.

The easiest way of checking the frequency ranges of different configurations for suitability is manually supplying the MOT coils (with $\sim 9\,\mathrm{V}$) and shifting the VCO frequency by means of an external power supply. Using the MOT live cam (cf. ch. 4.1.3) it is then possible to find out, whether an atom cloud can be trapped in the chamber within the desired fraction of the VCO range. This tests revealed, that upon selecting one of the slopes in the right half of fig. 3.8, looking somewhat like a mirror image of the left one, the beat frequency seems to have the same value as for its counterpart. However, the value obtained from the FFT is completely misleading, since it was not possible to establish a proper MOT for any of those slopes. In consequence, the right part of the error signal cannot be utilized for locking at all.

Apparently only one potential setup exists, which more or less meets the requirements regarding the frequency range. It uses the same offset $\Delta\nu$, but a different zero crossing of the reference error signal, which is labeled PA in fig. 3.7. The resulting shift seems to agree with a switch to the $F = 2 \rightarrow F' = 2$ transition, upon which the frequency is assumed to change by $\sim -55.05\,\mathrm{MHz}$. However, in this configuration the expected MOT and image detunings are already at the very edge of the oscillator range. The lock stability there is worse than in the central region. Hence, the laser tends to fall out of lock, when during a fast ramp the marginal area of the range is reached. Prolonging the ramp durations can solve this problem, but it is definitely not possible to image the cloud right after the molasses (due to the very fast ramp necessary for this measurement).

Imaging the atoms in the science chamber actually requires $\delta > 0$. The atoms are probably level-shifted by magnetic fields, since the low-field-seeking $m_F = 2$ state is prone to such influences (cf. ch. 2.1). This demands an additional setpoint shift on the PID controller of the TA master. It implies moving the position on the slope of the error-signal towards one of the extrema, which weakens the stability even more. The maximum possible correction seems to be $\sim +8\,\mathrm{MHz}$ and is restricted by the slope height. Although the resulting alternative locking scheme (fig. C.1) works at least for attaining a reasonable atom cloud in the MOT chamber, it is therefore not a good solution for moving the accessible range towards lower frequencies. As the problems could finally be fixed, the search for a proper alternative was stopped. It would have been possible to further modify the scheme by implementing more radical changes in the setup, e.g. by changing the Cooler AOM frequency, but therefore ruining the alignment.

Running the experiment with the alternative locking scheme for a little while allowed for examining the hypothesis, that a more negative molasses detuning results in a distinctly lower atom cloud temperature (cf. ch. 2.2.3). This was suggested by measurements some years ago, but the difference turned out to be negligible and not worth considering any configuration changes. It was actually figured out, that for quite some time the mo-

Fig. C.1: The alternative locking scheme for the Pierluigi and the TA master. In this configuration, considerably lower frequencies can be reached. In return, the $F' = 3$ level is already close to the upper limit of the frequency range, which considerably weakens the lock stability. The optical pumping is not shown here, since its weird behavior was the reason for the scheme change, but is supposed to work analog to fig. 3.10.

lasses detuning had been below the lower boundary defined by the calibration. Upon this, ADwin had supplied the FO-lock card with partly completely wrong and insanely fast ramps. Hence it is even surprising, that the atom cloud properties were this satisfying, since the actual frequencies must have been messed up. A clear distortion could only be observed in the shape of the molasses, which becomes very bulky and a lot bigger than for proper settings.

D FO calibration

Supply voltage [mV]	VCO [MHz]	APD [MHz]	Offset [MHz]	Supply voltage [mV]	VCO [MHz]	APD [MHz]	Offset [MHz]
-10000	188.5	204.0	15.5	200	118.7	135.0	16.3
-9802	187.0	202.4	15.4	401	117.5	133.8	16.3
-9599	185.4	200.6	15.2	599	116.3	133.0	16.7
-9399	183.8	199.0	15.2	800	115.2	131.8	16.6
-9201	182.2	197.6	15.4	1001	114.0	130.8	16.8
-9001	180.6	195.6	15.0	1201	112.8	129.4	16.6
-8801	179.0	194.2	15.2	1400	111.8	128.4	16.6
-8602	177.4	192.8	15.4	1601	110.6	127.0	16.4
-8400	175.9	191.0	15.1	1800	109.4	126.2	16.8
-8199	174.4	189.6	15.2	2000	108.2	124.8	16.6
-8002	172.9	188.4	15.5	2200	107.0	123.8	16.8
-7800	171.4	187.2	15.8	2399	105.8	122.6	16.8
-7600	170.0	186.0	16.0	2600	104.4	121.0	16.6
-7400	168.6	184.6	16.0	2799	103.2	120.2	17.0
-7201	167.1	183.4	16.3	3000	101.8	118.6	16.8
-7000	165.7	181.8	16.1	3200	100.5	117.6	17.1
-6799	164.2	180.4	16.2	3401	99.2	116.4	17.2
-6600	162.8	179.2	16.4	3599	97.6	115.4	17.8
-6400	161.3	178.0	16.7	3800	96.2	114.6	18.4
-6200	159.8	176.4	16.6	3900	95.4	114.0	18.6
-6001	158.4	175.2	16.8	4000	94.7	113.4	18.7
-5800	157.0	173.8	16.8	4200	93.3	112.0	18.7
-5601	155.6	172.6	17.0	4400	92.1	110.0	17.9
-5400	154.3	171.4	17.1	4601	90.8	107.6	16.8
-5200	153.0	170.0	17.0	4801	89.5	106.2	16.7
-4999	151.6	168.6	17.0	4999	88.4	104.4	16.0
-4801	150.3	167.4	17.1	5200	87.1	102.2	15.1
-4599	148.8	166.0	17.2	5400	85.8	99.8	14.0
-4400	147.6	164.6	17.0	5600	84.4	98.6	14.2
-4199	146.2	163.0	16.8	5799	83.0	98.0	15.0
-4000	144.8	161.8	17.0	5999	81.6	97.0	15.4
-3801	143.4	160.6	17.2	6199	80.1	95.6	15.5
-3600	142.1	159.2	17.1	6399	78.1	94.4	16.3
-3400	140.8	157.8	17.0	6600	77.1	93.2	16.1
-3198	139.5	156.4	16.9	6801	75.4	92.0	16.6
-2999	138.2	155.0	16.8	6999	73.9	90.8	16.9
-2800	137.0	153.6	16.6	7201	72.3	89.4	17.1
-2600	135.7	152.2	16.5	7399	70.8	88.2	17.4
-2399	134.4	150.8	16.4	7600	69.3	86.8	17.5
-2200	133.1	149.6	16.5	7799	67.9	85.6	17.7
-2001	131.9	148.4	16.5	8000	66.6	84.8	18.2
-1779	130.6	147.2	16.6	8201	65.5	84.0	18.5
-1600	129.4	145.8	16.4	8399	64.5	83.0	18.5
-1401	128.2	144.4	16.2	8599	63.5	82.0	18.5
-1201	127.0	143.2	16.2	8800	62.6	80.8	18.2
-999	125.8	142.0	16.2	9002	61.9	80.0	18.1
-800	124.6	140.6	16.0	9199	61.2	79.0	17.8
-601	123.4	139.6	16.2	9400	60.6	78.4	17.8
-400	122.1	138.2	16.1	9600	60.1	77.8	17.7
-201	121.0	137.2	16.2	9800	59.6	77.4	17.8
0	119.8	136.0	16.2	10000	59.2	77.0	17.8

Tab. D.1: Calibration of the frequency offset lock. The VCO was controlled with an external power supply. The TA master was locked to the slope labeled TS in fig. 3.8. The frequencies were measured with an oscilloscope connected to the *Monitor* output of the FO-lock card.

E   MOT instruction

This chapter provides a step-by-step instruction for setting up the magneto-optical trap. It is a much more detailed version of ch. 5.2 and comprises the exact alignment procedure.

Beam preparation   In order to check the alignment of the cooling beam to the telescope, the t-shirts (one has been shown in fig. 5.1) are inserted at the two ends. Before being widened, the beam usually exhibits a power of $\sim 230\,\mathrm{mW}$. Facing the t-shirts from the front side, i.e., looking into the propagation direction, the spot must be centered on both of them. This is done by adjusting the two closest mirrors. The latter should, however, only be touched, in case the MOT alignment is messed up anyway. Due to the long path, that the light still has to take before reaching the chamber, any slight changes have a rather huge impact.

For now, the t-shirts are removed again and the shape of the expanded beam is examined by means of an IR card. At least the center of the beam should be very uniform. This provides maximum overlap in the MOT chamber and prevents light vacancies somewhere right in the middle of the optical trap. If the beam is directed into the telescope having the same shape it shows when leaving the laserbox, spatial modes significantly distort its appearance. Therefore, two irises are used to cut off the perturbing fractions. They are labeled *IB1* and *IB2* in fig. 3.12. This costs some optical power, but allows for getting rid of most inhomogeneous features within the beam. As long as such are only located at the very edge, their influence on the MOT performance is negligible.

Reaching the MOT setup, the beam must centrally pass the half-wave plates and the beam splitters (cf. fig. 3.13). The alignment to the cubes can be checked with an IR card, for the wave plates an IR viewer (fig. E.1) can help. In both cases, the entire beam cross-section should enter each optical element. As the mirrors after the telescope only allow for changing the alignment of all six resulting beam axes simultaneously, it is advisable to rather move the optical components, if necessary. On three of the six axes, the quarter-wave plate can already be centered within the beam path as well, as no mirrors possibly being adjusted are located in between.

Alignment   The alignment procedure is basically the same for all three pairs of counter-propagating beams. Therefore, a generalized instruction shall be given here, using the following definitions: Each beam pair constitutes two opposed axes, which are called $A1$ and $A2$. The light propagating along $A1$ enters the MOT chamber through window $W1$
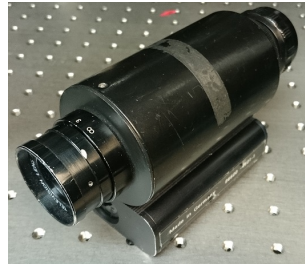

Fig. E.1: An IR viewer. Utilizing the reflections on the inner rim of the wave plates, one can make sure the beam is centrally passing through.

and leaves it through $W2$. The situation is reversed for the $A2$ beam. The mirror closest to the entrance window of $A1$ is called $M1.2$. Any other mirror further away (but still on the same side of the beam path with respect to the chamber) can be employed as $M1.1$. If somehow accessible, it makes sense to choose the very first mirror after the PBS here. In the same way, mirrors $M2.1$ and $M2.2$ are defined. Note that on $-Y$ only one mirror is located between the PBS and the entrance window. Consequently, the beam splitter itself must be employed as $M1.1$ or $M2.1$.

The t-shirts are placed in the telescope and the iris just before the MOT setup is almost entirely closed. It is labeled IM in fig. 3.12 and needed for cutting off some unwanted reflection. In case the alignment to the t-shirts is sufficiently accurate, the resulting tiny light spots represent the center of the widened beam. For discerning the window centers, an alignment plastic cap matching the window flanges was tinkered (shown before in fig. 5.2a). Due to the limited access there, on $-X$ another cap is required (fig. 5.2b). If one of the IR cams (fig. E.2) is pointed at the mounted cap, it is possible to observe the infrared beam on a screen. On some axes, these cameras are already permanently installed. As the light spot usually is too bright due to reflections, a polarization filter is inserted after the IM iris. Turning its wheel allows for adjusting the power and with it the size of the spot.

First, the beam propagating along $A1$ is centered on both chamber windows. Thus, $A2$ is blocked by placing some obstacle, e.g. a black piece of cardboard, right after the PBS. The axes usually utilized as $A1$ are $+X, -Z$ and $-Y$. The plastic cap is attached to $W1$ and $M1.1$ is adjusted, until the beam enters the window as centrally as possible. Then, the cap is removed and mounted on $W2$, where the spot is centered by means of $M1.2$. In principle, producing a second alignment cap and keeping both windows covered would be possible. However, two caps will never be exactly the same. Moreover, the light can be slightly diffracted, when entering the chamber through a hole in the plastic cap. Now switching back to $W1$ again, this procedure is repeated several times, until the spot matches the cap center on both windows simultaneously. How long this takes depends on the initial situation.

Aligning $A2$ is rather similar, but the reference points are not the same. However, it still starts with blocking $A1$ and centering the $A2$ laser spot on $W2$. The apparent center position can possibly differ depending on the direction, from which the beam is approaching the cap. Therefore, $A1$ is briefly unblocked in each iteration, so that
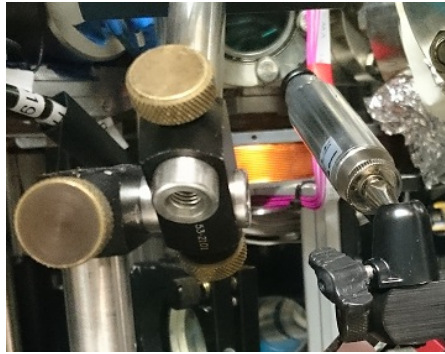

Fig. E.2: One of the alignment cameras. Upon connection to a screen, they allow for monitoring the position of the infrared laser spot.

the overlap can be checked. The second reference point of $A2$ is the PBS: The longer the distance, across which the counter-propagating beams overlap, the more precise the alignment. Upon removal of the polarization filter, the beam block and the cap, the two spots can be observed on an IR card placed right after the PBS. Their positions are matched by adjusting $M2.2$, for which a second person is very helpful.

Once the alignment looks promising, the t-shirts are removed and the iris is fully opened. The overlap of the expanded beams is reviewed on each window and after the PBS. Most times, repeating the procedure for $A2$ is necessary, but at some point it does not get better any more, as there is no perfect alignment. Finally, the remaining quarter-wave plates must be centrally placed within the beam path. An alternative to partly blocking one of the beams for checking the overlap is "switching" between the two axes by turning the associated half-wave plate. This should only be done if the optical power is not equally distributed to the axes anyway.

Power distribution   Ideally, the light entering the chamber should exhibit an equalized power distribution. By means of the *IM* iris, the beam diameter can be reduced to the size of a power meter head. The optical power can be measured right on front of the window on each axis. The easiest way of achieving the desired distribution is first equalizing the power within each pair of axes by turning the half-wave plates named *X2*, *Z2* and *Y1* in fig. 3.13. The overall power is then divided by six and the correct fractions are distributed to the three pairs by turning *X1* and *Z1* (in this order). Since the reflectivities respectively transmissivities of the optical elements slightly differ, this procedure has to be repeated a few times, always calculating a new power sum. It gets a lot harder, when the optics start degrading, as exemplified in appx. A.2.2. An overview of approximate wave-plate settings is given in tab. E.1. Note that the power distribution is very sensitive to even slightest changes in the angle of the wave plates. Touching the latter should therefore be avoided.

Polarization   Only major modifications of the beam alignment can lead to the necessity of adjusting the quarter-wave plates. In accordance with ch. 2.2, all beams must be circularly polarized. The orientation can be left (CL) or right (CR), but there is only one correct configuration for a 3D MOT. The polarization can be measured by means of a polarization analyzer. As the windows have no considerable influence, on each axis one polarization is acquired before the beam is entering, and the other after it is leaving the chamber. The other windows are not accessible due to the constructional constraints. Two counter-propagating beams must have the same circular polarization, since they approach the atoms from different directions. Consequently, eight potential settings are possible, of which only one results in a MOT cloud. An overview of the latest quarter-wave plate settings is given in tab. E.2.

Plate label	$X1$	$Z1$	Y	$X2$	$Z2$
Wheel position	103	112	246.5	253	210.5

Tab. E.1: Last settings of the half-wave plates. The assignment can be inferred from fig. 3.13. The values denoted here can only serve for orientation.

Axis	$+X$	$-X$	$+Z$	$-Z$	$+Y$	$-Y$
Polarization	CR	CR	CL	CL	CR	CR
Wheel position	205	28	139	5	23.5	40

Tab. E.2: Last settings of the quarter-wave plates. For a σ_+-σ_- configuration (cf. ch. 2.2), counter-propagating beams must have the same polarization due to the opposed directions, from which they approach the atoms.

Bias fields   After each modification of the alignment, the **bias fields B_comp_hor**, **B_comp_vert** and **B_comp_zero=B_comp_mol** need to be adjusted. The first two are controlled by *Agilent 6623A Power Supply.VI* (cf. fig. 4.2), the last two have always been set to the same value lately. Different optimization approaches have been tested, the most successful one is featured here. The basic idea is simply matching the position of the atom cloud with the minimum of the MOT coil field. At first, the **MOT coil current** is increased from **9** to **18** A in the corresponding analog channel. Upon this, the cloud on the live monitor becomes significantly smaller, the atoms being pulled into the middle of the magnetic trap. This central position is marked on screen. Then, the **TOF** is reduced to a point, where the cloud just starts expanding. The center of the absorption image, which represents the axis perpendicular to the MOT live cam, is marked as well. Now the current is changed back to **9** A and the GUI parameters are switched to imaging after the **molasses** (cf. ch. 4.2.2). Again, a rather small **TOF** is selected, but the expansion must be clearly discernible. Playing around with the **bias fields**, the MOT and the molasses cloud are simultaneously matched with the mark positions.

The actual shape of the MOT cloud slightly changes over time. The current supply calibrations might drift or optical elements might move just a little bit. As long as the benchmarks are satisfying (cf. ch. 4.2.3), there is no need for any optimization anyway.
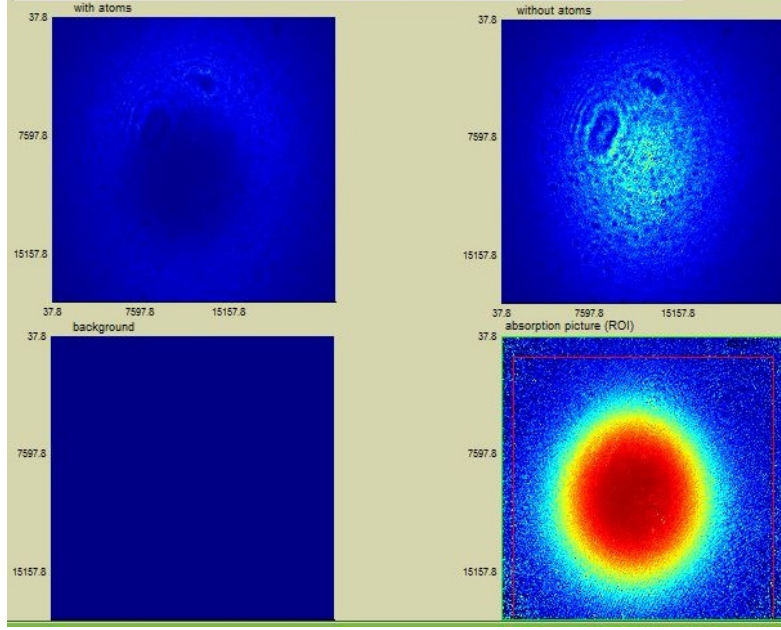
F   Miscellaneous

Fig. F.1: Principle of absorption imaging. For the first picture, imaging light is shined into the chamber after a variable TOF. Some of the light is absorbed by the atom cloud, the remaining fraction reaches the camera. A second picture is taken after the atoms have entirely vanished. Again, light is shined onto the camera, which this time acquires a full image of the beam. A third one is taken without any light, i.e., the background resulting from other sources is recorded. Pictures one and two are divided by the background. By then subtracting the picture without atoms from the one taken with atoms in the chamber, an image of the atom cloud can be generated.

Fig. F.2: Connection board for the superconducting part. By connecting the plug on top to the correct feedthrough, the chip wire and the coils can be manually supplied by an external current source. Primarily, the board is used for monitoring the coil resistances during maintenance work.